NASA Contractor Report 181939

COMPUTATIONAL DESIGN OF LOW ASPECT RATIO WING-WINGLET CONFIGURATIONS FOR TRANSONIC WIND-TUNNEL TESTS

John M. Kuhlman and Christopher K. Brown

WEST VIRGINIA UNIVERSITY
Morgantown, West Virginia

Grant NAG1-625
October 1989

National Aeronautics and
Space Administration

Langley Research Center
Hampton, Virginia 23665-5225

COMPUTATIONAL DESIGN OF LOW ASPECT RATIO WING-WINGLET CONFIGURATIONS FOR TRANSONIC WIND-TUNNEL TESTS

by

John M. Kuhlman and Christopher K. Brown

SUMMARY

Computational designs have been performed for three different low aspect ratio wing planforms fitted with nonplanar winglets; one of the three configurations has been selected to be constructed as a wind tunnel model for testing in the NASA LaRC 8-foot transonic pressure tunnel. A design point of $M = 0.8$, $C_L \cong 0.3$ was selected, for wings of aspect ratio equal to 2.2, and leading edge sweep angles of 45° and 50°. Winglet length is 15% of the wing semispan, with a cant angle of 15°, and a leading edge sweep of 50°. Winglet total area equals 2.25% of the wing reference area. This report summarizes the design process and the predicted transonic performance for each configuration.

In addition, a companion low-speed design study has been conducted, using one of the transonic design wing-winglet planforms but with different camber and thickness distributions. A low-speed wind tunnel model was constructed to approximately match this low-speed design geometry, and force coefficient data have been obtained for the model at speeds of 100-150 ft/sec. Measured drag coefficient reductions were of the same order of magnitude as those predicted by numerical subsonic performance predictions.

INTRODUCTION

Winglets have proven to be effective nonplanar drag reduction devices in several applications to high aspect ratio wing planforms typical of transport or business jet aircraft. However, recent studies have indicated even larger potential benefits may be obtained when winglets are used on low aspect ratio

configurations such as fighter aircraft (Refs. 1-6). It was found in the computational work of Refs. 1-6 that one can obtain the same percentage reduction in drag coefficient at the same C_L and ratio of winglet length-to-wing span, independent of wing aspect ratio and leading edge sweep, even at the transonic design point selected for the major emphasis of the current work. Since a low aspect ratio wing has a larger induced drag at the same lift than a high aspect ratio wing, then an equal percentage reduction in drag coefficient at equal lift coefficient results in a larger drag force reduction at low aspect ratio. The present work has been undertaken to design a transonic low aspect ratio wing-winglet wind tunnel model to be constructed and tested in the NASA LaRC 8-foot transonic pressure tunnel, to confirm the numerical drag reduction predictions of Refs. 1-6.

DESIGN PROCEDURE

Designs have been performed for three different wing planforms, all using the same design procedure developed in Refs. 1-2. For each wing planform, an optimum wing-alone geometry and a wing-winglet geometry have been defined. A linear potential flow theory design code (Refs. 7, 8) has been used to define wing-winglet and wing-alone camber surfaces for minimum induced drag at the selected design point of $M = 0.8$, $C_L \approx 0.3$. This design point was chosen as being representative of a cruise condition for heavily loaded lightweight fighters at an altitude of 30,000 feet. The design code was run at $C_L = 0.4$, because addition of a fuselage was found to reduce the calculated C_L by approximately 0.1. A NACA 64A006 thickness distribution has been added to the camber surface, and a cylindrical fuselage having a diameter equal to 0.125 times the wing span, and 5.25 times the wing span in length has been used. For all wing-winglet configurations the wing and winglet geometry have been altered in the vicinity of the wing-winglet juncture, to reduce loading

and eliminate or reduce the strength of any shocks formed in this region. Wing tip airfoil camber has been reduced, and geometric incidence has been reduced for the outboard 10% of the wing, while winglet camber has been reduced and toe out has been increased at the winglet root, following the procedures which were developed in Refs. 1-3. Also, for all current designs an a = 0.8 chordwise loading shape function has been utilized in an effort to eliminate any predicted upper surface trailing edge boundary layer separation, such as was found for the earlier designs which used an a = 1.0 rectangular loading (Ref. 1). This procedure was successful at eliminating predicted upper surface boundary layer separation for an aspect ratio 2.20 wing-winglet and wing in Refs. 2 and 3. Pressure recovery on the upper surface was observed to be more gradual as the value of a was reduced from 1.0 to 0.9 and 0.8, but shocks on the winglet were strengthened slightly. As stated in Ref. 3, there was no predicted boundary layer separation on the wing for the a = 0.8 configuration. However, all three chordwise loading functions yielded essentially the same calculated drag polars. The wing-winglet geometry for this planform is shown in Fig. 1.

Transonic performance predictions for the wing-alone and wing-winglet configurations versus angle of attack have been obtained using the WBPPW transonic small disturbance code of Refs. 9,10 at M = 0.8. Calculated force coefficients, spanloads, and boundary layer separation locations on the wing will be presented for all three wing planforms and the three corresponding wing-winglet configurations. Also, typical calculated pressure coefficient distributions will be presented at several angles of attack.

The low-speed design point selected was M = 0.1, $C_L \cong 0.3$. The selected lift coefficient is the same as that selected for the transonic model design point. Optimum wing-alone and wing-winglet camber surfaces were defined

using the linear theory potential flow design code of Refs. 7 and 8. An a = 0.8 chordwise loading function was used to reduce predicted wing trailing edge boundary layer separation. The camber surface of the wing-winglet design was modified to reduce loading in the wing-winglet juncture region, as was previously done for the transonic wing-winglet design (Refs. 1,2). Further description of these low-speed designs, as well as performance predictions for the wing-alone and wing-winglet geometries obtained, using the WBPPW analysis code, are included in Ref. 6. Calculated force and moment coefficients, normalized spanloads, wing boundary layer separation locations, and pressure coefficient distributions have been presented. These results are quite similar to those obtained previously at transonic flow conditions (Refs. 1-3).

PLANFORM DESCRIPTIONS

Two planforms previously studied in Refs. 1 and 2 have been used in the present design effort. These wing planforms were called cases F and G in Refs. 1 and 2. Also, a third planform has been studied which is essentially configuration G with an unswept trailing edge (called cropped delta G in this study). Definition of these three wing planforms is given in Table 1, while Figs. 1-3 show the resulting wing-winglet design geometries without the fuselage for cases F, G, and cropped delta G, respectively. Wing F has a leading edge sweep of 45° and A = 2.2, while wing G has Λ = 50°, A = 2.2. Both of these wings have a taper ratio of 0.2. The cropped delta G has an unswept trailing edge, with Λ = 50°, A = 2.22, and λ = .203.

Note that the uncambered airfoils having significant positive geometric incidence which are found at the wing root for all of the present designs (Figs. 1-3) are similar to those obtained for higher aspect ratio wings using automated optimization methods and transonic analysis codes, as found in Refs.

11,12. In Reference 11 the starting airfoil geometries included aft-cambered supercritical sections at the wing root, but the twisted, uncambered final root airfoils reduced the configuration drag.

All 3 wing-winglet configurations have winglet planforms with Λ = 50° and a taper ratio of 0.5. Winglet root chord is 60% of the wing tip chord and winglets have been mounted in an aft position. Winglet cant has been fixed at 15° outward from vertical, and all winglets have used a NACA 64A006 thickness distribution. These winglet planform choices are similar to those used in refs. 1-3, and are similar to design recommendations by Whitcomb (Ref. 13) for winglets mounted on transport type wings. Winglet total area is 2.25% of the wing reference area for configurations F and G, and 2.27% for configuration cropped delta G.

Wing-alone design geometries obtained from the linear design code have not been altered. However, in order to obtain successfully converged transonic flow predictions for the wing-winglet geometries using the WBPPW code, it was necessary to modify the linear theory camber surfaces in the wing-winglet juncture region, as discussed in Refs. 1,2, to reduce loading in this region. In addition, for the a = 0.8 chord loading used in the present study it was necessary to further reduce loading in the wing-winglet juncture as shown in Table 2. Also, for the present work, several different winglet geometries (camber and twist) have been analyzed. These winglet geometries are summarized in Fig. 4 for transonic designs and in Fig. 5 for low-speed designs.

The low-speed designs have used the same cropped delta G planform and winglet planform which have been selected for the transonic wind tunnel model, with Λ = 50°, A = 2.22, λ = .203 for the wing. A NACA 63_1-012 thickness distribution has been used for the low-speed design.

PRESENTATION OF PERFORMANCE RESULTS

For the transonic design configurations, predicted performance results to be presented include lift and drag coefficients, pitching moment and wing root bending moment coefficients, typical pressure coefficients, normalized spanloads, and upper surface wing boundary layer separation locations for the wing-alone and the wing-winglet configurations for all three wing planforms, generally for $-4° \leq \alpha \leq 0°$. Note that all force and moment coefficients presented include only the forces and moments on the wing and winglet, but omit those on the fuselage, because of the unreasonably large surface area of the very long fuselage used. Viscous effects on the winglet are estimated by the code using an empirical skin friction correlation. All results for configurations G and cropped delta G have been obtained using 150 crude grid iterations, followed by 150 crude-fine grid iterations using the interacted Bradshaw strip boundary layer on the wing, at a Reynolds number of 3.8×10^6 based upon wing mean aerodynamic chord. This is estimated to be a realistic Reynolds number for the wind tunnel model. Results for configuration F (partly taken from earlier work of Ref. 3) have been obtained using 100 crude grid iterations, followed by 200 crude-fine grid iterations with the interacted strip wing boundary layer at a Reynolds number of 9×10^6. Boundary layer transition has been assumed to occur at $x/c = 0.05$.

Note that for both the wing-alone and wing-winglet configuration F, no converged transonic flow solutions could be obtained for $\alpha > 0.5°$, while all G and cropped delta G configurations would not converge for $\alpha > 0°$. These differences in convergence boundaries may have been influenced by the different Reynolds numbers which were used; the higher Reynolds number for configuration F reduced the amount of predicted boundary layer separation, which in turn may have improved code convergence slightly. Similar difficulty

was encountered in Refs. 1-3 for the previous geometries using an a = 1.0 rectangular chord loading. However, for the present configurations using a = 0.8 chord loadings this difficulty in obtaining converged solutions while including the viscous boundary layer calculation at higher lift coefficients seems to be worsened. Note also that results for a modified cropped delta G wing-winglet are presented (Table 2), where further unloading of the wing-winglet juncture by increased winglet root toe out and wing tip twist was successful at increasing the angle of attack for which converged solutions could be obtained up to α = 1° (C_L = 0.3344, versus C_L = 0.2934 at α = 0°).

The calculated transonic performance prediction results are presented in the following figures: (Force coefficients are also presented in Table 3)

Results	Figure Numbers
Configuration F Force Coefficients	6
Configuration F Spanloads	7
Configuration F Boundary Layer Separation	8
Configuration F Wing-Winglet C_p's	9-11
Configuration G Force Coefficients	12
Configuration G Spanloads	13
Configuration G Boundary Layer Separation	14
Configuration G Wing-Winglet C_p's	15-17
Configuration G Wing-Alone C_p's	18-20
Configuration Cropped Delta G Force Coefficients	21
Configuration Cropped Delta G Spanloads	22
Configuration Cropped Delta G Boundary Layer Separation	23
Cropped Delta G Wing-Winglet C_p's	24-26
Optimum Wing-Alone Cropped Delta G C_p's	27-29
Modified Cropped Delta G Wing-Winglet C_p's	30-33
Same Airfoil Cropped Delta G Wing-Winglet C_p's	34-36
Wing of Cropped Delta G Wing-Winglet C_p's	37-39
Boundary Layer Separation, α = 0°, All Configurations	40

The geometry of the low-speed wing-winglet configuration is given in Fig. 41. Calculated performance results for the low-speed designs are presented in the following figures:

Finally, the results of the low-speed wind tunnel tests are presented in the following figures:

DISCUSSION OF TRANSONIC PERFORMANCE PREDICTIONS

Force Coefficients

Predicted lift and moment coefficients for each of the three different basic wing planforms all look quite similar, and all vary linearly versus angle of attack. Generally, wing-winglet configurations develop slightly less lift at the same α than the corresponding optimum wing-alone configuration. This is due to the modifications which were required in the wing-winglet juncture to reduce loading in this region. Note, however that the effect of adding a winglet to a fixed wing geometry may be seen in Fig. 21 by comparing the wing-winglet C_L with that of the wing of the wing-winglet design (diamond

symbols). Addition of a winglet not only reduces C_D somewhat due to the thrust on the winglet but also increases C_L by about 5% at the same α (by .016 at $C_L \cong .293$ and by .011 at $C_L \cong .206$), due to the endplate effect.

Drag polars and L/D versus C_L also all look similar, where the drag polars appear to be shifted downwards to lower drag levels for the wing-winglet configurations relative to the corresponding optimum wing-alone configurations. Predicted percentage reductions in C_D at equal C_L are presented in Table 4 for all three wing planforms for C_L between 0.18 and 0.26. Note that predicted percent reduction in C_D tends to decrease slightly as C_L increases, and that these percent reductions are comparable for all three wing planforms.

Pitching moment coefficients about the wing apex are not altered greatly for wing-winglet configurations. For example, for the cropped delta G, C_m becomes more negative by 1.5% at $C_L = .18$ and 1.9% at $C_L = .26$ for the wing-winglet relative to the wing-alone. Wing root bending moment coefficients for wing-winglet configurations are increased by about 5-6% relative to the corresponding wing-alone case at equal lift. For the cropped delta G, increases are 5.4% at $C_L = .18$ and 6.0% at $C_L = .26$. These percentage increases are consistent with those observed in Refs. 1-3, and are expected to be related to the wing structural weight penalty due to the winglet.

Comparison of drag polars or lift-to-drag ratios in Fig. 21 for the three different winglet geometries, which have been shown in Fig. 4 (the old, new "modified", and same airfoil designs), indicates that significantly different winglet geometries, mounted to the same wing geometry, yield essentially identical predicted percent reductions in drag coefficient, so long as the same spanload is developed (Fig. 22). As is seen in Fig. 21, these different winglet

geometries all yield nearly identical predicted drag polars. Thus, numerical predictions at M = .8 indicate the same nominal 12% reduction of C_D at $C_L \cong .3$, for a range of winglet camber and twist distributions. This is consistent with earlier results in Ref. 1 where the percent drag coefficient reduction was shown to be independent of wing planform details so long as the spanload is essentially unaltered. These results are also all consistent with the conclusion that percent reduction in C_D should be determined solely by the ratio of winglet length to wing semispan and the spanload distribution (Ref. 1), which is based upon a far field induced drag model. Note that these predicted 12% reductions in C_D neglect the fuselage drag; hence about 6-8% reduction in total drag is expected.

Spanloads

Spanloads for the present work have been defined as the local sectional lift coefficient times the local chord, divided by the configuration mean geometric chord, and normalized by C_L. As a result, total area under the spanload curve is independent of C_L; this area is equal to one. Further, the total area under the curve is unaltered by changes in the upwash field, which will vary as angle of attack is varied. (Note that normal force magnitudes on the winglet may be extracted by dividing by the cosine of the winglet dihedral angle.) Spanload results are shown typically at α = 0°, -2°, -4°, for both the wing-alone and the wing-winglet configurations. Spanload shape does not change greatly with angle of attack for the wing-alone or the wing-winglet configurations. Loading near the centerline is reduced for all configurations, due to the fuselage. This shifts the loading center outboard, and results in higher local Mach numbers on the wing upper surface near the wing tip than otherwise would be required to develop a given C_L value. Loading is higher than elliptical near the wing tip of the wing-alone

configurations. Also, loading outboard on the wing is higher than the theoretical optimum for wing-winglet configurations, except at the wing tip. Loading is also reduced relative to the linear theory theoretical optimum at the winglet root. Similar trends were observed in Refs. 2,3. These reductions in spanload near the wing-winglet juncture are due to the geometry modifications which were made to reduce loading and weaken shocks in this region.

Boundary Layer Separation

Comparison of predicted wing boundary layer separation locations shows variations between the three wing planforms. None of the configurations have any predicted boundary layer separation on the wing lower surface for $-4° \leq \alpha \leq 0°$. The configuration F wing-alone and wing-winglet results show essentially no predicted upper surface boundary layer separation, as first reported in Ref. 3. However, both the G and cropped delta G configurations have predicted boundary layer separation on the wing upper surface, which tends to worsen as α is increased. The lack of predicted boundary layer separation for configuration F is largely the result of the higher Reynolds number which was used.

This is shown most clearly in Fig. 40 where predicted upper surface separation locations at $M = 0.8$, $\alpha = 0°$ are compared for the three wing-alone designs and the four wing-winglet designs. Note that results for the modified cropped delta G wing-winglet are for $\alpha = -0.5°$, because the solution at $\alpha = 0°$ experienced difficulties in the boundary layer calculation. Neither the F or G wing-alone configurations have any predicted boundary layer separation, while the cropped delta G wing has predicted separation near the trailing edge for $0.23 < \eta < .34$ and $.66 < \eta < .9$. No boundary layer separation is observed for the configuration F wing-winglet at $Re = 9 \times 10^6$, while both configurations G

and cropped delta G have predicted boundary layer separation over the entire wing, from the wing-body juncture, where separation is predicted at x/c ≅ .985 to the vicinity of the wing-winglet juncture where separation is predicted at x/c ≅ .93. The modified cropped delta G is somewhat better, but still has predicted upper surface boundary layer separation outboard of η = .76. As a check, one run of the case F wing-winglet at α = -0.5° at Re = 3.8 x 10^6 (C_L = 0.2616) did indicate some wing upper surface boundary layer separation near mid-span and at the wing tip.

The predicted boundary layer separation locations from the WBPPW code have been monitored versus the iteration count, as summarized in Table 5. Generally, the predicted separation region initially grows and then decreases in size as the iteration count increases. The predicted separation region may be further reduced in size with a greater number of iterations. Also, the reduced number of initial crude grid iterations used for configuration F (100 versus 150) may have slightly influenced the boundary layer separation prediction, by reducing the steepness of any regions of rapid pressure recovery.

Pressure Coefficient Distributions

Pressure coefficient distributions for all configurations appear quite similar to one another at nearly equal C_L values. Also, C_p distributions on the wing of each wing-winglet configuration are essentially identical to those of the corresponding wing-alone configuration except at the wing tip, where the presence of the winglet results in additional loading relative to the wing-alone. Pressure distributions at α = 0° all are quite similar to those obtained previously in Refs. 1-3. Use of the a = 0.8 chordwise loading function results in more gradual pressure recovery on the upper surface near the trailing edge relative to results with a = 1.0, as seen previously in Ref. 3.

Mid-chord shocks are found on the inboard surfaces of the lower half of the winglets for all four wing-winglet configurations for $\alpha > -2°$ ($C_L > 0.2$). Calculated chordwise pressure distributions change quite significantly versus angle of attack, even though there is not much variation in normalized spanload.

As angle of attack is decreased to $\alpha = -4°$, pressure suction spikes are observed on the lower surfaces of all wing-alone and wing-winglet configurations near the leading edge. The level of these suction spikes at $\alpha = -4°$ appear to be quite similar for all 3 wing-alone and 5 wing-winglet configurations. The development of such leading edge suction spikes is due to the relatively small nose radius of the 64A006 thickness distribution utilized for the present design geometries.

Pressure distributions for the two wings analyzed for the cropped delta G planform are quite similar. However the wing of the wing-winglet design has slightly greater suction on the upper surface near the leading edge.

Calculated upper and lower surface pressure distributions on the winglet, and on the wing near the tip, are at times observed to cross near the trailing edge. This is believed to be due to the frozen streamwise wake modeling utilized in the WBPPW code.

DISCUSSION OF LOW-SPEED PERFORMANCE PREDICTIONS

All general observations made for force coefficients of the transonic designs also apply to the M = 0.1 low-speed designs shown in Fig. 41. Predicted drag coefficient reduction for the original wing-winglet design relative to the optimum wing-alone design is 11.7% at $C_L = 0.26$. This is comparable to predicted percent reductions for the transonic designs. Note that converged performance results were obtained for the low-speed configurations at much higher C_L values than for the transonic design.

Comparison of drag polars and lift-to-drag ratios (Fig. 42) for the three low-speed winglet designs shown in Fig. 5 (using a single winglet airfoil, the original winglet design, and the uncambered winglet design) again show similar predicted performance benefits for all three winglet geometries relative to the optimum wing-alone configuration. Calculated lift-to-drag ratios for the low-speed configurations are unreasonably high for small C_L values, apparently because of unreasonably low (even negative) pressure drag coefficient values at low C_L values.

Spanloads (Fig. 43) also look nearly identical to those presented for the transonic designs. This has been observed to be true for all three of the winglet geometries. Thus, it also appears that at low speeds there are again several different winglet geometries which will generate nearly the same spanload, and hence, yield the same percentage reduction in drag coefficient.

The predicted wing upper surface boundary layer separation (Fig. 44) for the low-speed designs is also somewhat similar to behavior at M = 0.8. Of course, pressure coefficient distributions (Figs. 45-59) for the low-speed designs are significantly different from those for the thinner transonic designs, most noticably in the wing-winglet juncture region. Note that calculated C_p distributions at the winglet root at $\alpha = 4°$ are not realistic for all three winglet geometries.

DISCUSSION OF LOW-SPEED WIND-TUNNEL RESULTS

As described in Ref. 6, the low-speed wind-tunnel model has been constructed using the wing geometry of the M = 0.1 wing-winglet cropped delta G design, for which performance predictions have been presented in Figs. 42-60. Tests have been conducted at velocities of 104 and 149 ft/sec in the 32 inch by 45 inch cross section low speed wind-tunnel at WVU. The

model has a wing span of 27" and a wing reference area of 2.27 ft^2. The model has been constructed using aluminum ribs and spars, filled with auto body filler, and hand finished. A simple, nearly cylindrical fuselage houses a six component strain gage balance. The model mounts to a sting and angle-of-attack mechanism which is adjustable between $-8° \leq \alpha \leq 16°$. The winglets have been constructed from aluminum plates to the proper winglet planform. These flat-plate winglets were attached to the wing tips using screws and wedge-shaped blocks which yielded approximately 7 degrees of toe out. The winglets were attached in approximately a vertical orientation. Body filler was then used to fashion a smooth fillet between the wing tip and the lower portion of the winglet leading edge, as well as to form a cambered airfoil with a rounded leading edge. This construction technique yielded winglet airfoils with more camber and twist than for the design winglet geometry from the design code of Refs. 7 and 8. Boundary layer transition trips were placed on the wing upper and lower surfaces; these trips were sized according to criteria in Ref. 14, and located at 0.05 of the local wing chord.

Force data has been obtained both for the wing-winglet model and the wing without winglets, but fitted with rounded wing tips. Since the winglets were attached in essentially a vertical orientation, both configurations had the same projected wing span. Preliminary results of these wind-tunnel entries have been presented in Ref. 6. The present results are generally consistent with the earlier data analysis. However, the present results are expected to be more accurate since the data was reduced using the full balance calibration, including nonlinear interactions. Also, the measured fuselage chamber pressure was used to correct the drag measurement to free stream static pressure conditions, and the nominal angle of attack has been corrected

for observed sting deflections. However, no further corrections, such as for blockage or jet boundary effects, have been applied to the data.

Measured lift coefficients are increased in magnitude by the addition of the winglets, both at U = 104 ft/sec (Fig. 61) and at U = 149 ft/sec (Fig. 62). This endplate effect was also predicted by the numerical results. Measured C_L values are quite repeatable (Fig. 61). Measured pitching moment coefficients, calculated about the quarter mean aerodynamic chord, are more negative for the wing-winglet configuration than for the wing-alone.

Measured total drag coefficient is lower and lift-to-drag ratio is higher for the wing-winglet configuration at both test velocities above a lift coefficient of between 0.4 and 0.5. This measured drag reduction due to the winglet is maintained up to a nominal lift coefficient of 1.0 (Fig. 61). At lift coefficients below 0.4 the wing-alone configuration has a lower measured drag. It is believed that the relatively high observed C_L value before the winglets lead to a drag reduction is most likely due to the relatively large amount of toe out used on the wind-tunnel model (7°). This toe out is approximately the amount used for the uncambered winglet geometry shown in Fig. 5, while the wind-tunnel model had a cambered winglet. Thus, the wind-tunnel model winglet geometry would be expected to function properly at higher C_L values where larger local inflow angles over the wing near the wing tip would be expected. Note that repeatability of the measured drag for the wing-winglet configuration is not as good as is observed for the lift and pitching moment coefficients at the lower velocity (Fig. 61). Maximum magnitudes of measured rolling and yawing moment coefficients are +.0023 and -.0038, respectively. Maximum side force coeffcient is +.0697 for a winglet run, and +.0428 for a no winglet run. Using the average measured drag the observed drag reduction at 104 ft/sec is 18% at C_L = .7 and 10% at C_L = 1.0, while at 149 ft/sec the

drag reduction is 13% at C_L = 0.7.

WINGLETS ON GENERAL RESEARCH FIGHTER MODEL

One additional numerical design study which has been conducted as a part of the present work has been an assessment of the effectiveness of an "add-on" winglet design for the existing NASA Langley general research fighter model, as described in Ref. 15. All wings for this model are uncambered. It was thought that if sufficient potential for drag reduction existed, it would be relatively inexpensive to simply attach winglets to the existing wing panels.

For this study, the lower-sweep wing for the model was used, with A = 2.5, Λ = 44°, λ = 0.2, with a NACA 64A006 thickness distribution at the root tapering to a NACA 64A004 thickness distribution at the tip. Various winglet geometries were added to the basic wing and the performance was assessed versus angle of attack using the analysis code of Refs. 9, 10, at a Mach number of 0.8. Predicted performance for an uncambered winglet on this wing was initially reported in Ref. 5. More recently a cambered winglet has been designed, using the winglet tip airfoil for the cropped delta G configuration. The wing and uncambered winglet geometry are shown in Fig. 63.

Predicted force coefficients for these two winglet designs are compared with wing-alone performance in Fig. 64. It is seen that these two winglet designs have a very limited drag reduction potential. The cambered winglet design yields the larger predicted drag reduction, of about 4.5% at C_L = 0.25. This is only about 40% of the predicted drag reduction for the other designs having cambered wings.

Typical calculated C_p distributions for these configurations are summarized in Figs. 65-67. Results for the cambered winglet at α = 6° and 4° are shown in Figs. 65 and 66, respectively, while results for the uncambered winglet at α

= 6° are shown in Fig. 67. Since the wing is uncambered, all wing chordwise C_p distributions are nearly triangular, with most loading occurring near the leading edge. Cambered winglet pressures look similar to those observed on the F, G, and cropped delta G configurations. Pressures for the uncambered winglet look similar to those observed on the wing, except that suction spikes at the leading edge are more extreme.

It appears that perhaps one reason for the poorer predicted drag reduction for the general research fighter may be the smaller loading on the wing in the vicinity of the winglet. As seen in Fig. 68, predicted normalized spanload is approximately 0.4 near the wing tip for the cambered winglet design on the general research fighter, while this value is approximately 0.5 for configurations F (Fig. 7) G (Fig. 13), and cropped delta G (Fig. 22). As a result of this relatively small potential drag reduction, plans to build this model were abandoned.

CONCLUSION AND RECOMMENDATIONS

Predicted transonic flow performance results have been presented for eight different low aspect ratio configurations (three wing designs and five wing-winglet designs) for a design point of M = 0.8, $C_L \approx 0.3$. All wing-winglet designs yield essentially the same predicted percent drag reduction relative to the corresponding wing-alone design, independent of wing planform and winglet camber and twist. However, since it is felt that the cropped delta G wing planform is most representative of wing planforms for current and next generation fighter wings, this will be the configuration which will be constructed for the wind tunnel test, even though this planform had the worst predicted boundary layer separation characteristics. The same winglet airfoil cropped delta G wing-winglet and cropped delta G wing-alone geometries will be constructed to fit to a simplified cylindrical fuselage with

an ogive nose, to allow a fair comparison between the drag of the wing-winglet relative to the wing-alone. Predicted drag reductions due to the winglet of about 12% at C_L = 0.26, neglecting the fuselage, should correspond to approximately a 6-8% total drag reduction when the fuselage forces are included.

Since the configurations selected for the transonic tunnel test do have some predicted boundary layer separation, it is recommended that some redesign of both configurations be performed using the automated design method of Smith (Ref. 16), which uses the methodology of the airfoil design method of Campbell (Ref. 17). In particular, pressure recovery should be made more gradual near the trailing edge, to eliminate the predicted trailing edge boundary layer separation for both the wing-alone and wing-winglet designs. Also, it may be possible to improve flow in the vicinity of the wing-body juncture. It may also be desirable to increase the nose radius slightly to reduce the leading edge pressure spikes away from the design point. However, this may be a disadvantage if the model is tested at supersonic Mach numbers.

A similar low-speed design study has also been performed for the cropped delta G wing planform at M = 0.1, using the same design methodology and analysis code as has been used for the transonic designs. All of the conclusions for the predicted effects of winglets at transonic Mach numbers also apply at these lower speeds.

Finally, design and testing of a low aspect ratio wing-winglet model designed at M = 0.1 has been summarized. The measured drag coefficient reduction is the same order of magnitude as the predicted drag coefficient reduction based on numerical modeling.

ACKNOWLEDGEMENTS

The present numerical design effort has been supported by NASA Langley Research Grant NAG-1-625, Mr. Richard L. Campbell, technical monitor. All aerodynamic calculations have been made using the NASA Langley computer complex, accessed from WVU via Telenet. NASA Langley also has provided the strain gage balance on loan. Students Tim Cox, David Jenkins, Jeff Tuttle, and the second author participated in the design and construction of the angle-of-attack mechanism, and the wind tunnel model design as a senior year undergraduate project during the Spring 1988 semester. Data reduction for the low-speed wind-tunnel data has been performed by Mr. Charles H. Fox, Jr. and Mr. Bruce Graham at NASA Langley.

REFERENCES

1. Kuhlman, J. M. and Liaw, P., "Winglets on Low Aspect Ratio Wings," J. of Aircraft, Vol. 25, No. 10, October 1988, pp. 932-941.

2. Kuhlman, J. M., Liaw, P., and Cerney, M. J., "Theoretical/Numerical Study of Feasibility of Use of Winglets on Low Aspect Ratio Wings at Subsonic and Transonic Mach Numbers to Reduce Drag," NASA CR-4174, August 1988.

3. Kuhlman, J. M., Cerney, M. J., and Liaw, P., "Transonic Low Aspect Ratio Wing-Winglet Designs," Paper AIAA-87-0007, presented at AIAA 26th Aerospace Sciences Meeting, Reno, NV, Jan. 11-14, 1988.

4. Liaw, C.-H. P., "The Use of Winglets on Low Aspect Ratio Wings for Drag Reduction at Transonic Speeds," MSAE Thesis, West Virginia University, Mechanical and Aerospace Engineering Dept., Morgantown, WV, June 1987.

5. Cerney, M. J., "Numerical Design Study of Winglets on Low Aspect Ratio Wings Using Supercritical Airfoil Technology," MSAE Thesis, West Virginia University, Mechanical and Aerospace Engineering Dept., Morgantown, WV, May 1988.

6. Kuhlman, J. M. and Brown, C. K., "Computational Design of Low Aspect Ratio Wing-Winglets for Transonic Wind-Tunnel Testing," Paper AIAA-89-0644, presented at AIAA 27th Aerospace Sciences Meeting, Reno, NV, Jan. 9-12, 1989.

7. Kuhlman, J. M. and Shu, J.-Y., "Computer Program Documentation for a Subcritical Wing Design Code Using Higher Order Farfield Drag Minimization," NASA CR-3457, September 1981.

8. Kuhlman, J. M., "Higher Order Farfield Drag Minimization for a Subcritical Wing Design Code," J. of Aircraft, Vol. 17, No. 9, September 1980, pp. 648-655.

9. Boppe, C. W. and Stern, M. A., "Simulated Transonic Flows for Aircraft with Nacelles, Pylons, and Winglets," Paper AIAA-80-0130, presented at AIAA 18th Aerospace Sciences Meeting, Pasadena, CA, January 14-16, 1980.

10. Boppe, C. W., "Aerodynamic Analysis of Aircraft with Nacelles, Pylons, and Winglets at Transonic Speeds," NASA CR-4066, April 1987.

11. Haney, H. P., Johnson, R. R., and Hicks, R. M., "Computational Optimization and Wind Tunnel Test of Transonic Wing Designs," Paper AIAA-79-0080, presented at AIAA 17th Aerospace Sciences Meeting, Jan. 15-17, 1979, New Orleans, LA; see Fig. 12.

12. Henne, P. A., "An Inverse Transonic Wing Design Method," Paper AIAA-80-0330, presented at AIAA 18th Aerospace Sciences Meeting, Jan. 14-16, 1980, Pasadena, CA; see Figs. 13,14.

13. Whitcomb, R. T., "A Design Approach and Selected Wind-Tunnel Results at High Subsonic Speeds," NASA TN D-8260, July 1976.

14. Braslow, A. L. and Knox, E. C., "Simplified Method for Determination of Critical Height of Distributed Roughness Particles for Boundary-Layer Transition at Mach Numbers from 0 to 5, NACA TN 4363, 1958.

15. Huffman, J. K., "Effect of Vertical-Tail Location on the Aerodynamic Characteristics at Subsonic Speeds of a Close-Coupled Canard Configuration," NASA TN D-7947, Aug. 1975.

16. Smith, L. A., "PPWFLEX: A Method for the Design of Transonic Flexible Wings," M.S. Thesis, School of Engineering and Applied Science, George Washington University, Feb. 1988.

17. Campbell, R. L. and Smith, L. A., "A Hybrid Algorithm for Transonic Airfoil and Wing Design," Paper AIAA-87-2552, presented at AIAA 5th Applied Aerodynamics Conference, Aug. 17-19, 1987, Monterey, CA.

Table 1. Wing Planform Definition

1.	CASE F	A = 2.2	TR = 0.2	SWEEP = 45°
2.	CASE G	A = 2.2	TR = 0.2	SWEEP = 50°
3.	CROPPED DELTA G	A = 2.22	TR = 0.203	SWEEP = 50°

Table 2. Incidence Variation for Wing-Winglets at M = 0.8
Using a = 0.8 Chord Loading

	Change in Wing Tip Incidence at η = (0.91,0.97,1.0)	Change in Winglet Incidence at ζ = (0,.42,.80,1.0)
CASE F	0°, 0°, -1°	-5°, -3°, -1°, 0°
CASE G	-0.6°, -1.2°, -1.3°	-3.9°, -2.5°, -0.9°, 0°
CROPPED DELTA G	-0.6°, -1.2°, -1.3°	-3.9°, -2.5°, -0.9°, 0°
MODIFIED CROPPED DELTA G	-1°, -1.8°, -1.9°	-4.5°, -3°, -0.9°, 0°
CROPPED DELTA G, SINGLE WINGLET AIRFOIL	-1.0°, -1.8°, -1.9°	-1.5°, -0.75°, -0.5°, +1.2°
GENERAL RESEARCH FIGHTER, SINGLE WINGLET AIRFOIL	0°, 0°, 0°	1°, 9°

Table 3. Calculated Force and Moment Coefficients

Configuration F

α	C_L	C_D	C_m	C_B	Configuration
0.0	.28616	.01870	-.2546	.14628	FWING
-1.0	.24538	.01380	-.2265	.12551	FWING
-2.0	.20326	.00984	-.1971	.10390	FWING
-3.0	.16040	.00700	-.1670	.08178	FWING
-4.0	.11432	.00568	-.1345	.05765	FWING
0.0	.27881	.01536	-.2522	.15118	FWWLT
-1.0	.23507	.01077	-.2205	.12803	FWWLT
-2.0	.19042	.00740	-.1882	.10422	FWWLT
-3.0	.14428	.00541	-.1548	.07949	FWWLT
-4.0	.09667	.00514	-.1206	.05371	FWWLT

Configuration G

α	C_L	C_D	C_m	C_B	Configuration
0.0	.29192	.01978	-.2908	.15008	GWING
-0.5	.27466	.01779	-.2786	.14144	GWING
-1.0	.25110	.01504	-.2580	.12936	GWING
-1.5	.22984	.01303	-.2408	.11838	GWING
-2.0	.21174	.01173	-.2280	.10910	GWING
-2.5	.18979	.01014	-.2099	.09760	GWING
-3.0	.16652	.00887	-.1905	.08545	GWING
-3.5	.14347	.00806	-.1717	.07355	GWING
-4.0	.12070	.00773	-.1535	.06153	GWING
0.0	.29390	.01770	-.2937	.15984	GWWLT
-0.5	.27124	.01516	-.2744	.14766	GWWLT
-1.0	.	.	.	.	GWWLT
-1.5	.22679	.01102	-.2373	.12376	GWWLT
-2.0	.20481	.00954	-.2194	.11196	GWWLT
-2.5	.18225	.00831	-.2008	.09979	GWWLT
-3.0	.15923	.00745	-.1818	.08705	GWWLT
-3.5	.13388	.00685	-.1601	.07361	GWWLT
-4.0	.11043	.00693	-.1412	.06060	GWWLT

Table 3. (Continued) - Calculated Force and Moment Coefficients

Configuration Cropped Delta G

α	C_L	C_D	C_m	C_B	Configuration
0.0	.29279	.01971	-.2907	.15044	CWNGOPT
-0.5	.27364	.01746	-.2761	.14097	CWNGOPT
-1.0	.25238	.01511	-.2587	.12999	CWNGOPT
-1.5	.23003	.01295	-.2402	.11848	CWNGOPT
-2.0	.21162	.01165	-.2270	.10920	CWNGOPT
-2.5	.18708	.00981	-.2058	.09622	CWNGOPT
-3.0	.16658	.00890	-.1902	.08556	CWNGOPT
-3.5	.14299	.00808	-.1708	.07332	CWNGOPT
-4.0	.11959	.00777	-.1519	.06092	CWNGOPT
0.0	.27769	.01844	-.2733	.14335	CWNGNOT
-0.5	.25815	.01616	-.2582	.13363	CWNGNOT
-1.0	.23633	.01379	-.2399	.12250	CWNGNOT
-1.5	.21561	.01194	-.2235	.11216	CWNGNOT
-2.0	.19506	.01035	-.2074	.10147	CWNGNOT
-2.5	.17402	.00900	-.1908	.09088	CWNGNOT
-3.0	.15088	.00778	-.1715	.07826	CWNGNOT
-3.5	.12788	.00707	-.1528	.06670	CWNGNOT
-4.0	.10475	.00676	-.1342	.05445	CWNGNOT
0.0	.29344	.01730	-.2949	.15959	CWLTOLD
-0.5	.27181	.01488	-.2769	.14814	CWLTOLD
-1.0	.	.	.	.	CWLTOLD
-1.5	.22862	.01107	-.2415	.12477	CWLTOLD
-2.0	.20594	.00944	-.2224	.11267	CWLTOLD
-2.5	.18278	.00821	-.2031	.10011	CWLTOLD
-3.0	.16091	.00754	-.1857	.08840	CWLTOLD
-3.5	.13517	.00688	-.1632	.07429	CWLTOLD
-4.0	.11080	.00692	-.1430	.06096	CWLTOLD
1.0	.33443	.02268	-.3286	.18121	CWLTNEW
-0.5	.26995	.01472	-.2748	.14687	CWLTNEW
-1.0	.24789	.01259	-.2564	.13492	CWLTNEW
-1.5	.22561	.01084	-.2379	.12261	CWLTNEW
-2.0	.20356	.00937	-.2197	.11107	CWLTNEW
-2.5	.18022	.00831	-.2006	.09806	CWLTNEW
-3.0	.15831	.00754	-.1826	.08659	CWLTNEW
-3.5	.13301	.00701	-.1608	.07264	CWLTNEW
-4.0	.10839	.00712	-.1403	.05918	CWLTNEW
0.0	.28594	.01690	-.2856	.15379	CWLTSMF
-2.0	.19979	.00921	-.2149	.10761	CWLTSMF
-4.0	.10481	.00662	-.1357	.05583	CWLTSMF

Table 3. (Continued) - Calculated Force and Moment Coefficients

Low Speed Cropped Delta G Configuration

α	C_L	C_D	C_m	C_B	Configuration
4.0	.42788	.04950	-.40145	.21880	WINGOPT
2.0	.36482	.03584	-.34989	.18729	WINGOPT
0.5	.31469	.02670	-.30886	.16182	WINGOPT
0.0	.29607	.02363	-.29312	.15247	WINGOPT
-2.0	.22166	.01337	-.23138	.11439	WINGOPT
-3.0	.18495	.00965	-.20226	.09553	WINGOPT
-4.0	.14568	.00630	-.17022	.07490	WINGOPT
4.0	.43355	.04653	-.41527	.23391	WLTCAMB
3.0	.40172	.03967	-.38862	.21761	WLTCAMB
2.0	.36923	.03330	-.36187	.20055	WLTCAMB
1.0	.33646	.02755	-.33534	.18339	WLTCAMB
0.5	.31674	.02423	-.31790	.17317	WLTCAMB
0.0	.29937	.02165	-.30370	.16419	WLTCAMB
-1.0	.26026	.01620	-.26996	.14356	WLTCAMB
-2.0	.22174	.01170	-.23765	.12318	WLTCAMB
-3.0	.17957	.00758	-.20119	.10111	WLTCAMB
-4.0	.14284	.00522	-.17277	.08123	WLTCAMB
4.0	.42858	.04577	-.40894	.22915	WLTFLAT
3.0	.39645	.03908	-.38200	.21261	WLTFLAT
2.0	.36420	.03296	-.35548	.19580	WLTFLAT
1.0	.32898	.02683	-.32554	.17766	WLTFLAT
0.0	.29158	.02102	-.29357	.15833	WLTFLAT
-1.0	.25754	.01664	-.26665	.14018	WLTFLAT
-2.0	.21628	.01168	-.23073	.11848	WLTFLAT
-3.0	.17719	.00799	-.19833	.09788	WLTFLAT
-4.0	.13654	.00492	-.16458	.07611	WLTFLAT
4.0	.40926	.04631	-.38375	.21143	WINGNOT
3.0	.37825	.03955	-.35824	.19608	WINGNOT
2.0	.34753	.03349	-.33374	.18043	WINGNOT
1.0	.31303	.02722	-.30478	.16329	WINGNOT
0.0	.27820	.02168	-.27634	.14556	WINGNOT
-1.0	.24302	.01677	-.24791	.12754	WINGNOT
-2.0	.20646	.01236	-.21832	.10883	WINGNOT
-3.0	.16881	.00863	-.18776	.08933	WINGNOT
-4.0	.13006	.00561	-.15657	.06940	WINGNOT
12.0	.65005	.11094	-.60118	.33790	WLTSAMF
8.0	.54922	.07738	-.51320	.28984	WLTSAMF
4.0	.42781	.04540	-.40823	.22912	WLTSAMF
3.0	.39589	.03853	-.38141	.21267	WLTSAMF
2.0	.36311	.03218	-.35426	.19562	WLTSAMF
1.0	.32983	.02640	-.32705	.17807	WLTSAMF
0.0	.29041	.02008	-.29224	.15783	WLTSAMF
-4.0	.13712	.00452	-.16564	.07630	WLTSAMF
-6.0	.05262	.00116	-.09598	.03104	WLTSAMF
-7.0	.00696	.00058	-.05687	.00619	WLTSAMF
-8.0	-.0385	.00119	-.01983	-.0184	WLTSAMF

Table 3. (Concluded) - Calculated Force and Moment Coefficients

General Research Fighter Model Configuration

α	C_L	C_D	Configuration
0.0	.00000	.00298	WNGONLY
2.0	.08278	.00662	WNGONLY
4.0	.16327	.01439	WNGONLY
6.0	.24766	.02662	WNGONLY
0.0	.00025	.00331	WLTFOLD
2.0	.08859	.00706	WLTFOLD
4.0	.17451	.01527	WLTFOLD
6.0	.26076	.02786	WLTFOLD
0.0	-.0010	.00403	WLTSMFL
1.0	.04946	.00489	WLTSMFL
2.0	.08510	.00694	WLTSMFL
3.0	.12759	.01017	WLTSMFL
4.0	.16887	.01448	WLTSMFL
5.0	.21169	.01988	WLTSMFL
6.0	.25511	.02652	WLTSMFL

Table 4. WIBCO-PPW Predicted Percentage Drag Reductions Due to Winglets at M = 0.8 Using a = 0.8 Chord Loading

	C_L = 0.18	C_L = 0.22	C_L = 0.26
CASE F	18%	16%	12.7%
CASE G	14.8%	14.6%	12.7%
CROPPED DELTA G	14.7%	15.4%	13.3%
MODIFIED CROPPED DELTA G	12.2%	15.3%	13.5%
CROPPED DELTA G, SINGLE WINGLET AIRFOIL	10.6%	16.1%	13.2%

Table 5. Predicted Upper Surface Boundary Layer Separation Locations Versus Iterations for Modified Cropped Delta G Wing-Winglet at M = 0.8, α = -0.5° (150 crude grid iterations)

x/c for Boundary Layer Separation

η	154 its	214 its	254 its	314 its	354 its	414 its
.145	.985					
.195	.983					
.245	.983					
.295	.979					
.347	.980					
.400	.978					
.455	.972					
.511	.969					
.570	.967		.999			.996
.631	.965					
.695	.963		.972			
.763	.960		.957	.997	.978	.990
.836	.955	.979	.955	.976	.948	.979
.914	.956	.952	.951	.951	.947	.957

Table 5. (Concluded) - Predicted Upper Surface Boundary Layer Separation Locations Versus Iterations for Cropped Delta G Optimum Wing-Alone at M = 0.8, α = -0.5° (150 crude grid iterations)

x/c for Boundary Layer Separation

η	154 its	214 its	254 its	314 its	354 its	414 its	450 its
.139	.984						
.186	.982						
.234	.980						
.282	.975						
.332	.976						.996
.382	.973			.995		.994	
.435	.968			.993		.990	
.488	.967			.990		.996	
.544	.962			.985	.988		
.603	.955		.965	.990	.996	.990	
.665	.951		.959	.990	.995	.987	
.730	.945	.997		.990	.994	.985	1.000
.799	.942	.992		.987		.991	.993
.874	.940	.988	.996		.997	.992	.994
.956	.951				.998		

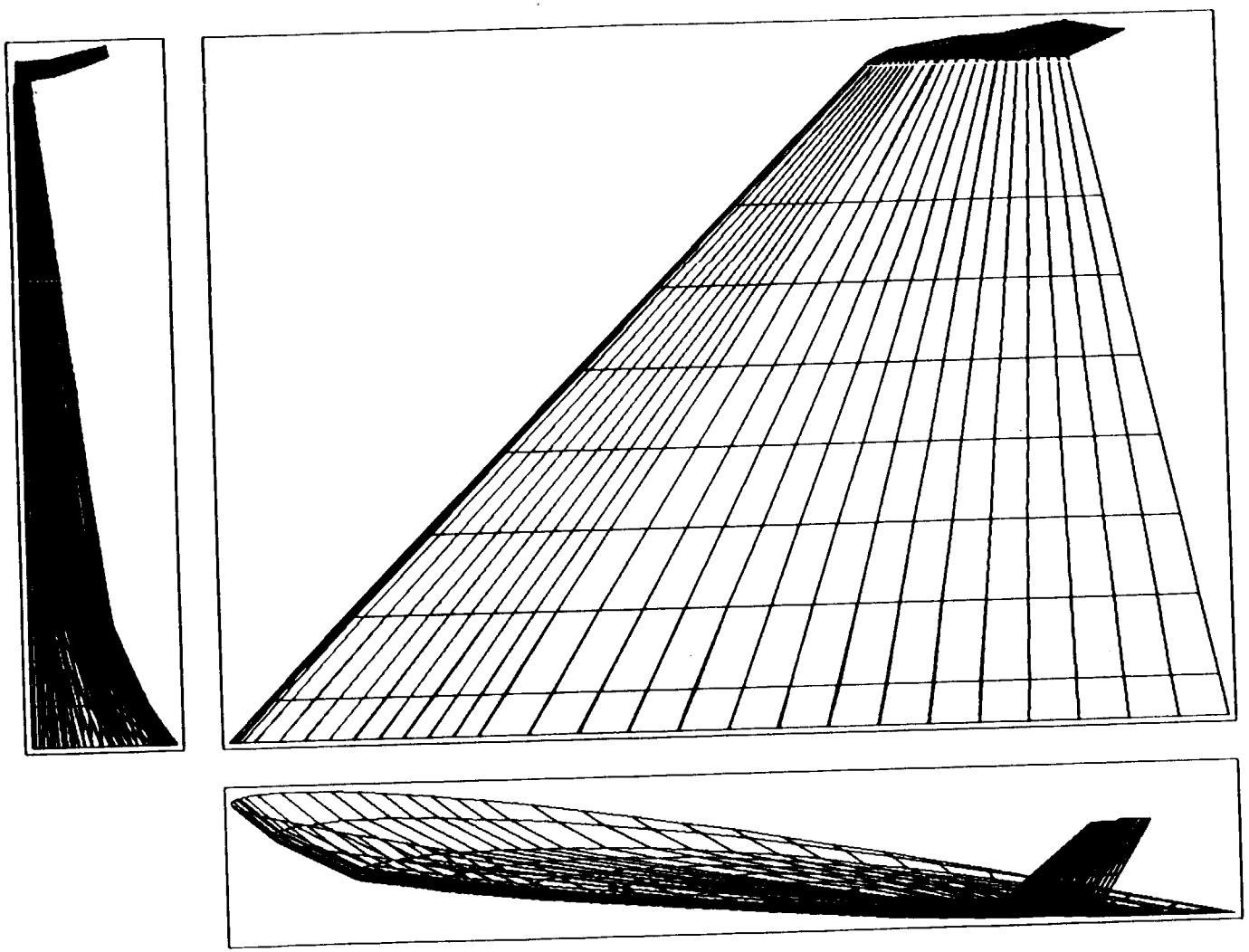

Fig. 1 Wing-Winglet geometry for configuration F (A = 2.20, Λ = 45°, λ = 0.2).

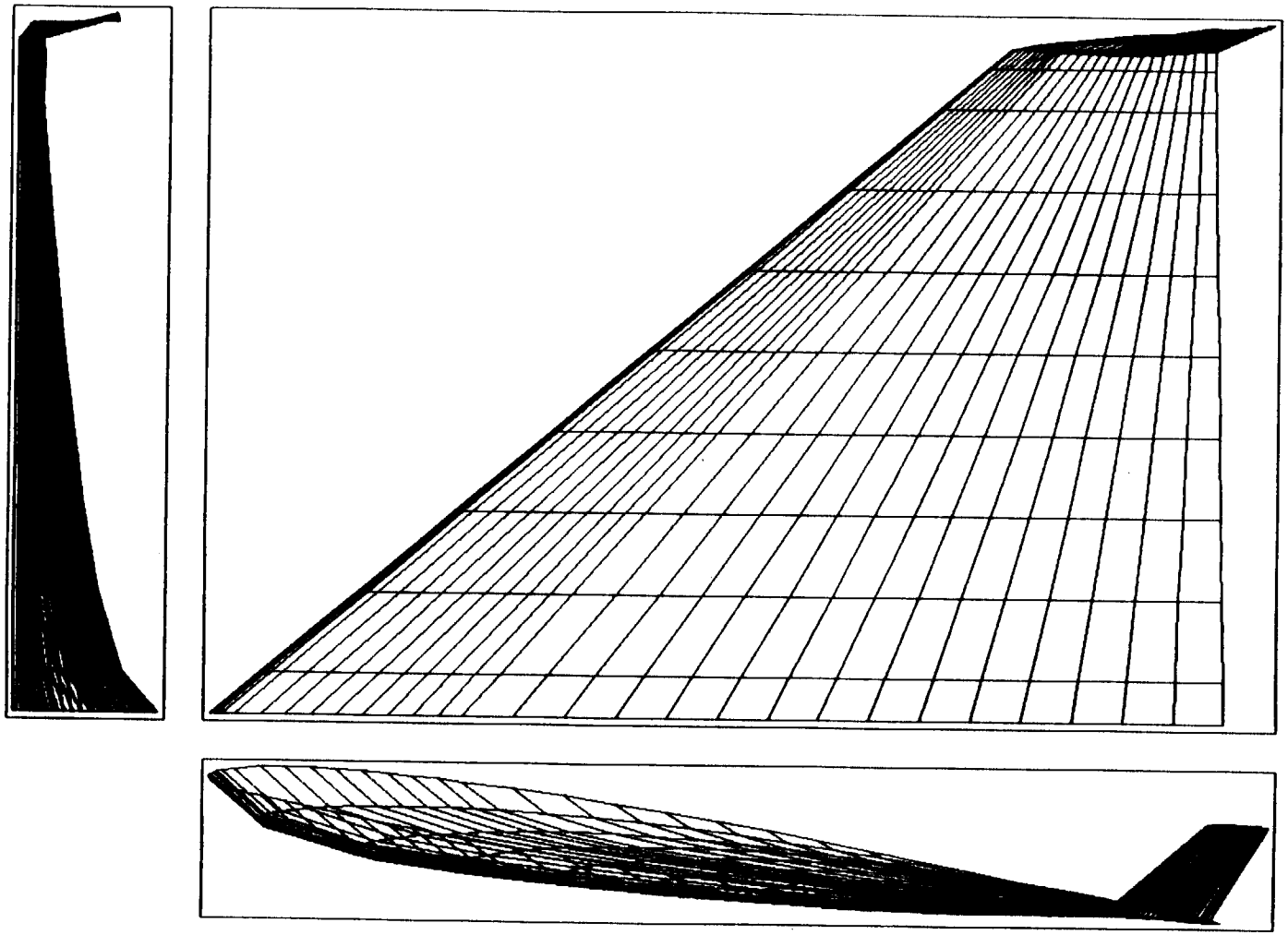

Fig. 2 Wing-winglet geometry for configuration G (A = 2.20, Λ = 50°, λ = 0.2).

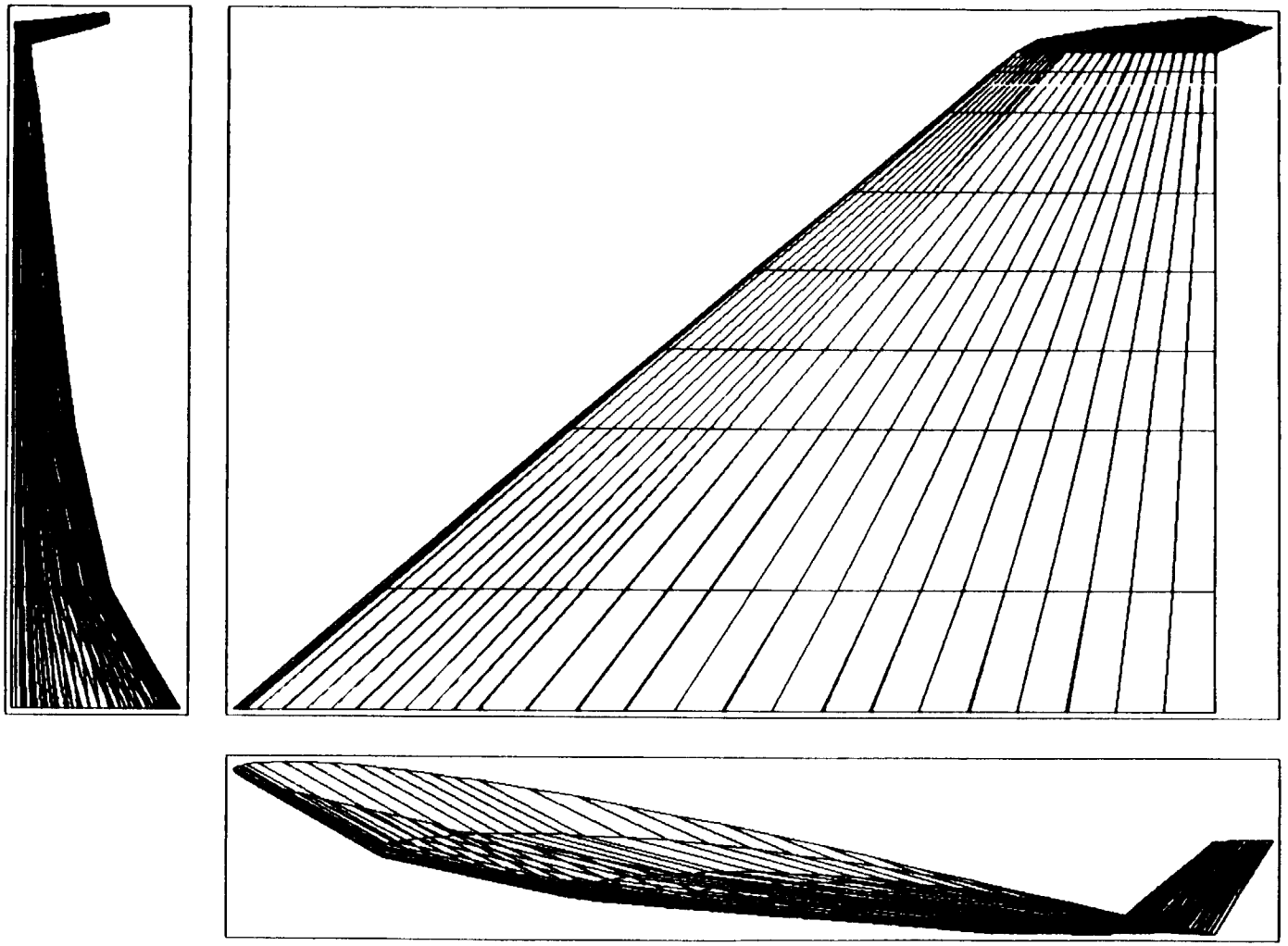

Fig. 3 Wing-winglet geometry for configuration cropped delta G (A = 2.22, Λ = 50°, λ = 0.203).

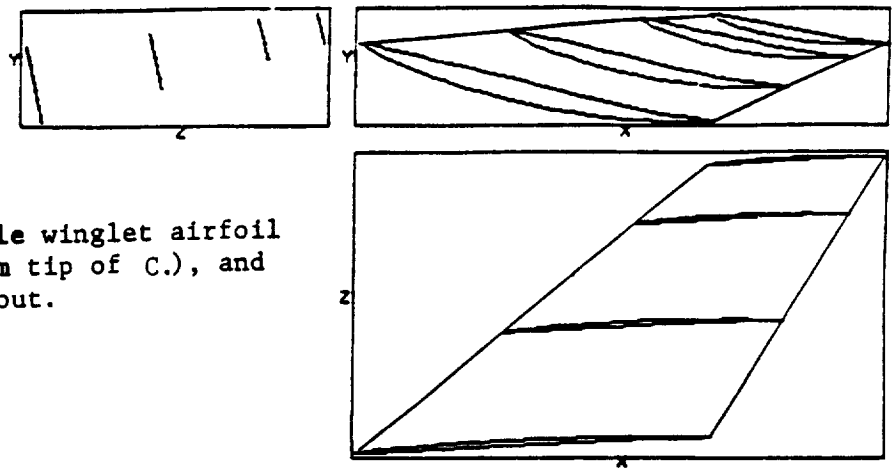

A. Single winglet airfoil (from tip of C.), and toe out.

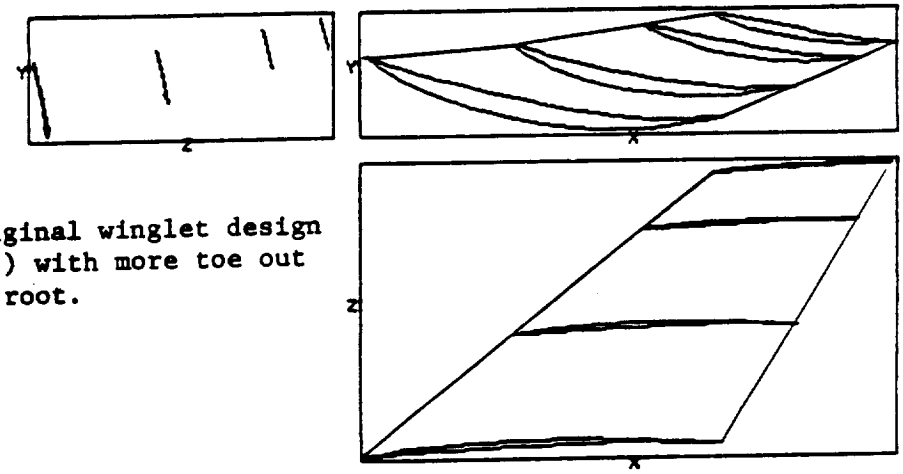

B. Original winglet design (C.) with more toe out at root.

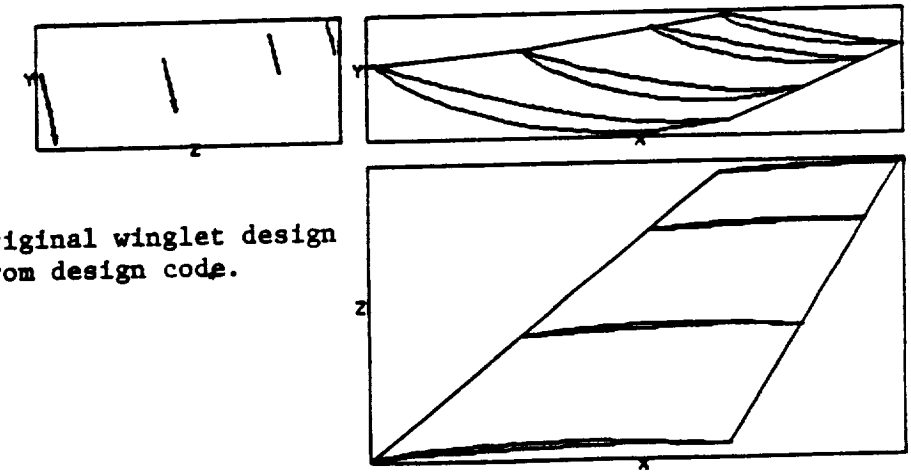

C. Original winglet design from design code.

Figure 4 Winglet geometries analyzed at M=0.8 on cropped delta G wing planform.

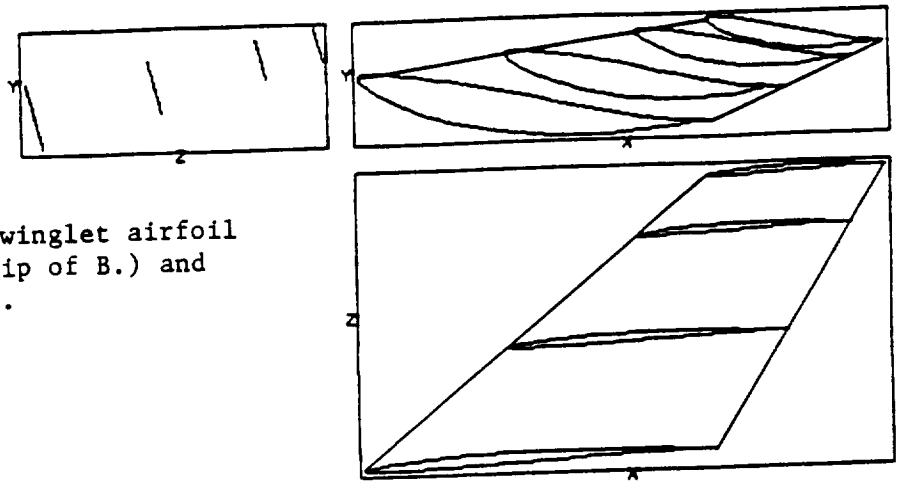

A. Single winglet airfoil (from tip of B.) and toe-out.

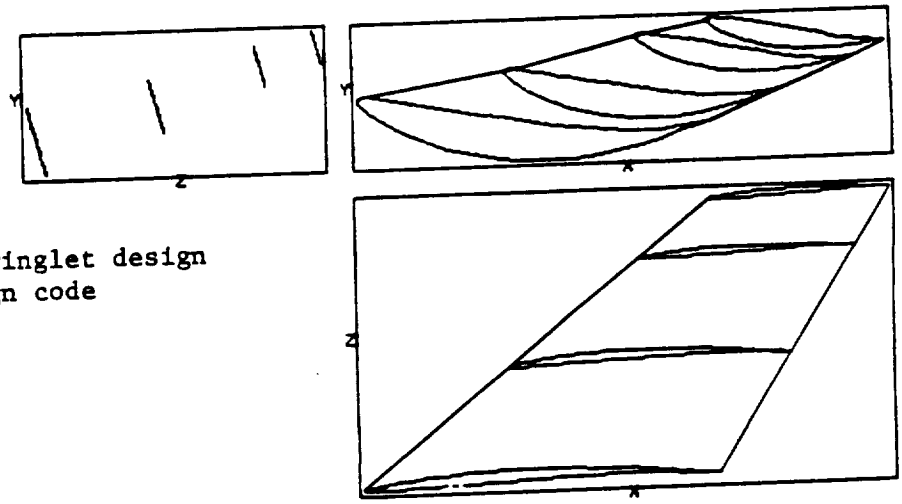

B. Original winglet design from design code

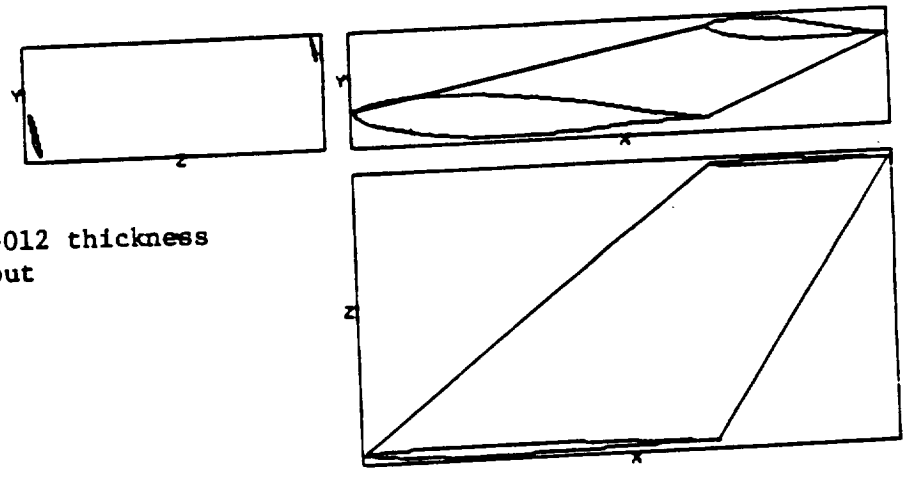

C. NACA 63_1-012 thickness and toe-out

Figure 5 Winglet geometries analyzed at M=0.1 on cropped delta G wing planform.

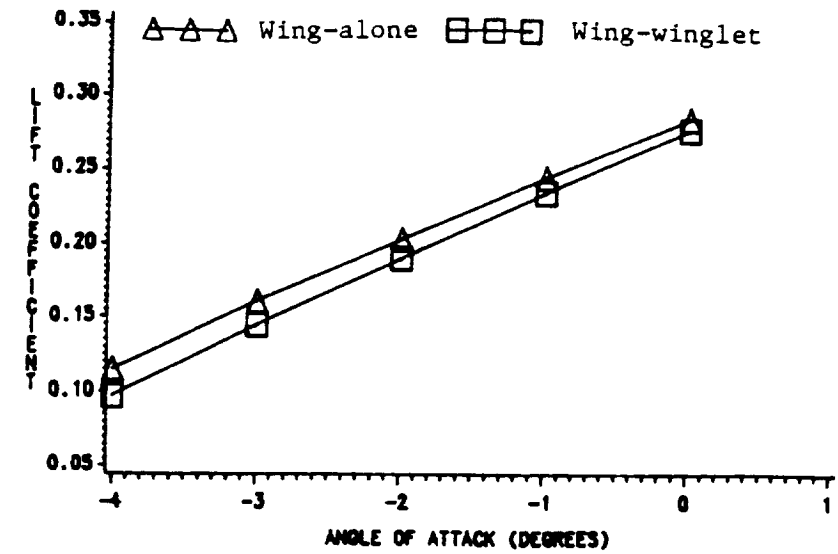

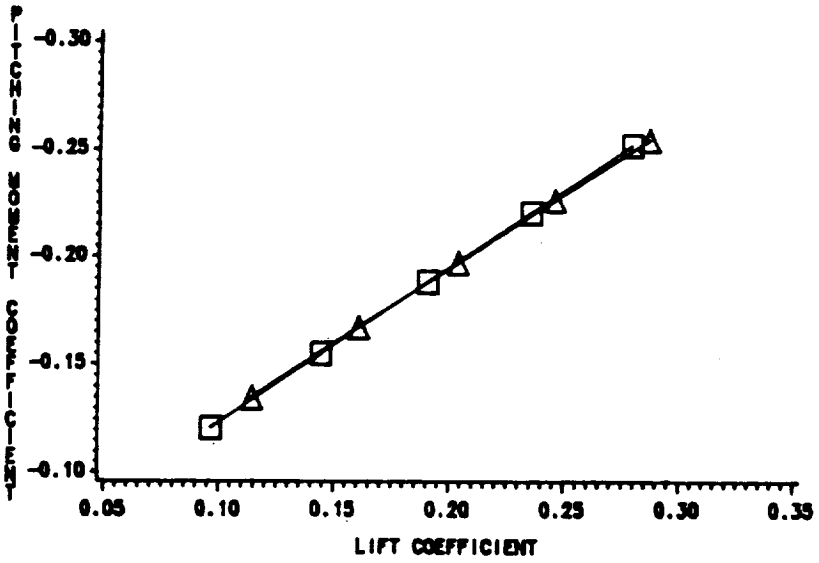

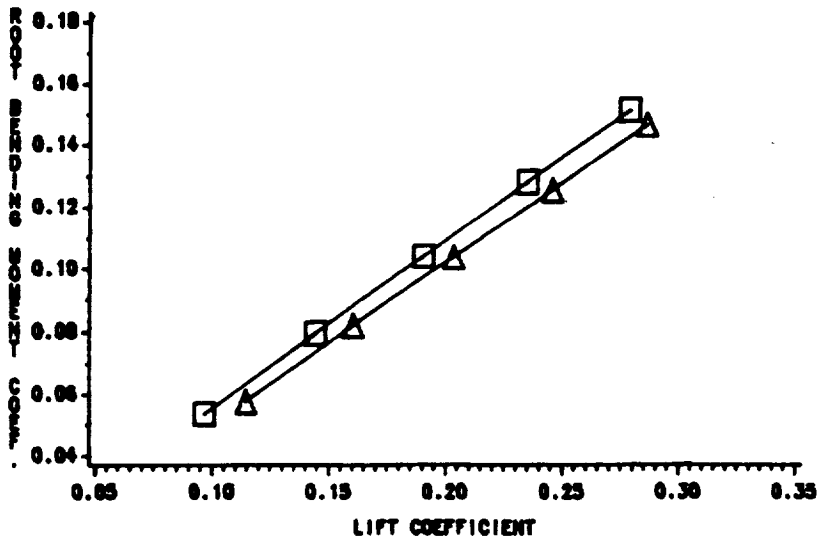

Fig. 6. Predicted performance of wing-alone and wing-winglet configurations F at M = 0.8; C_L - α, C_m - C_L, C_B - C_L.

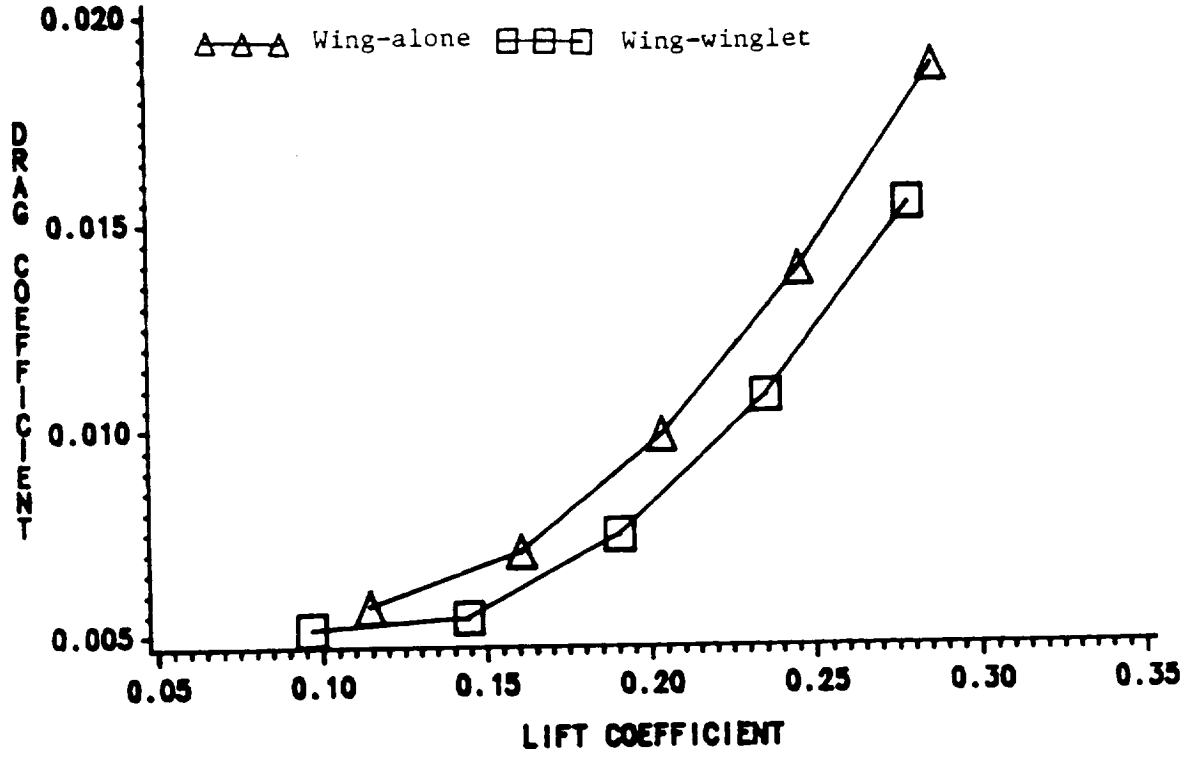

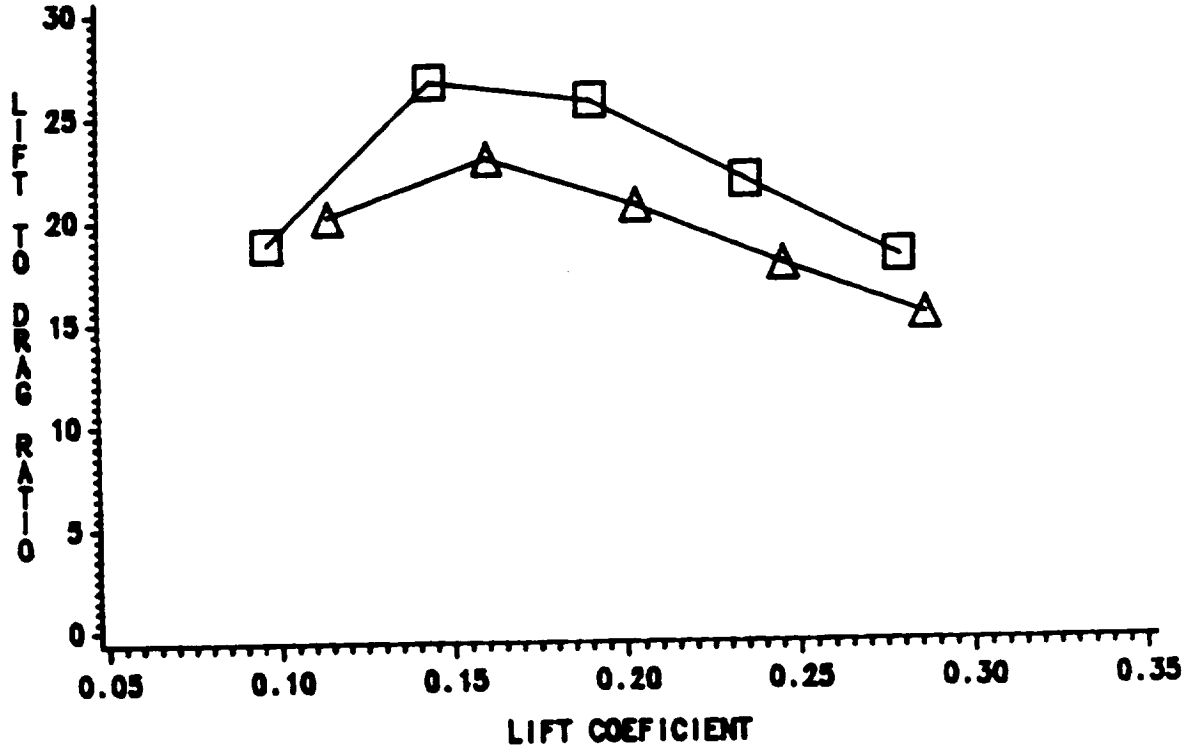

Fig. 6. (Concluded) - Predicted performance of wing-alone and wing-winglet configurations F at M = 0.8; drag polar and L/D - C_L.

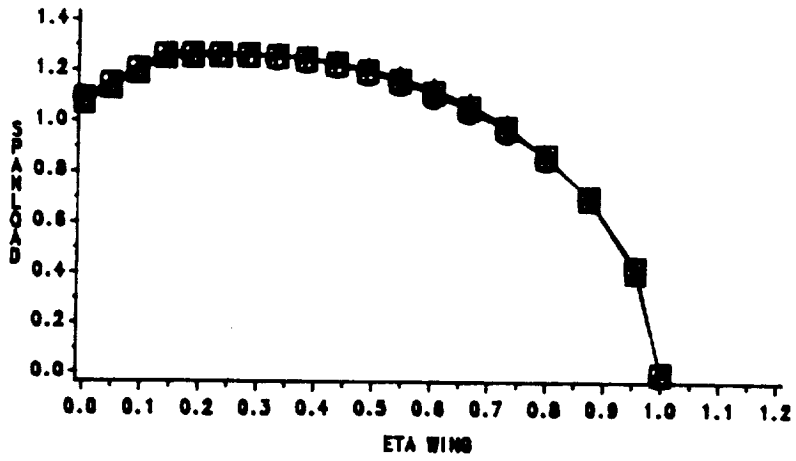

Wing-alone

DIAMOND: A=1 TRIANGLE: A=2
CIRCLE: A=0 SQUARE: A=4

Angle of attack (deg)

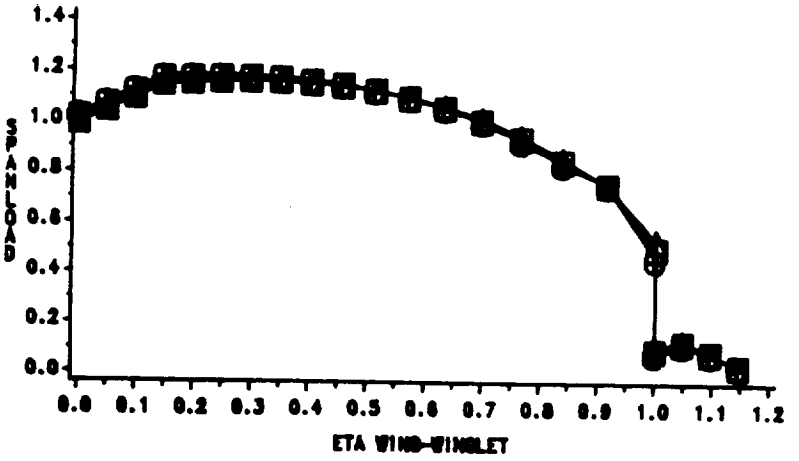

Wing-winglet

Fig. 7. Calculated normalized spanloads for wing-alone and wing-winglet configurations F at M = 0.8.

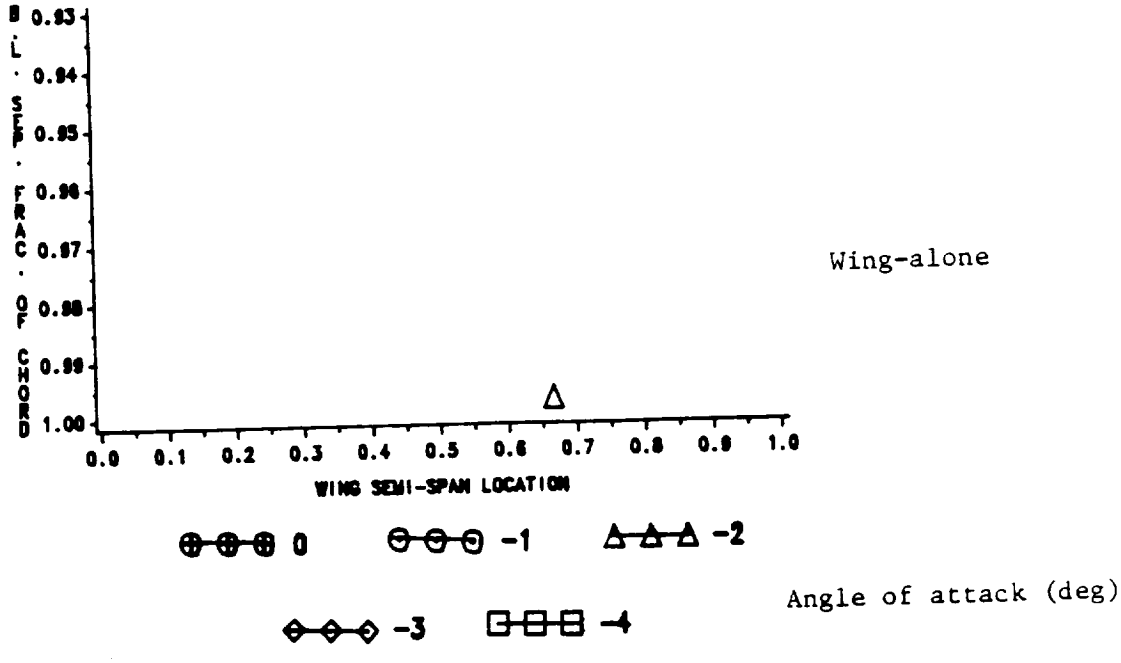

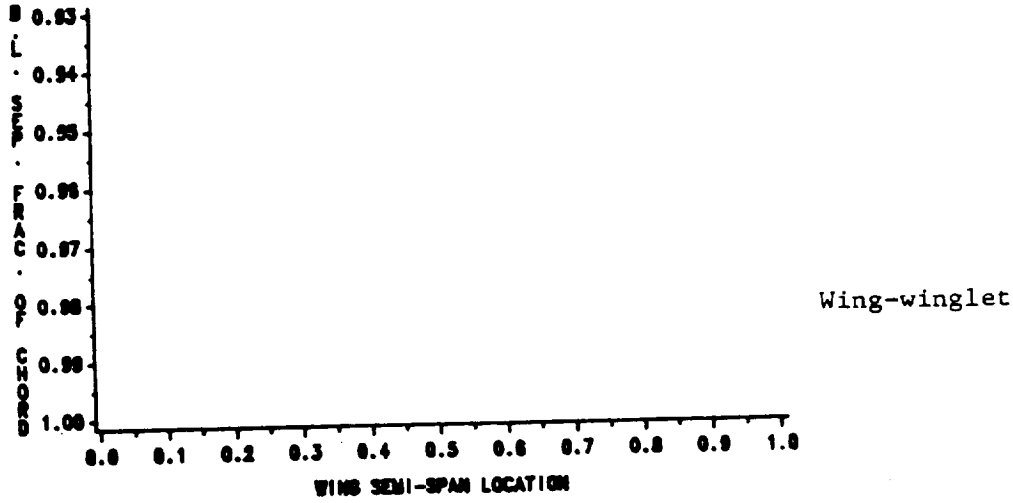

Fig. 8. Predicted upper surface boundary layer separation locations for wing-alone and wing-winglet configurations F at M = 0.8.

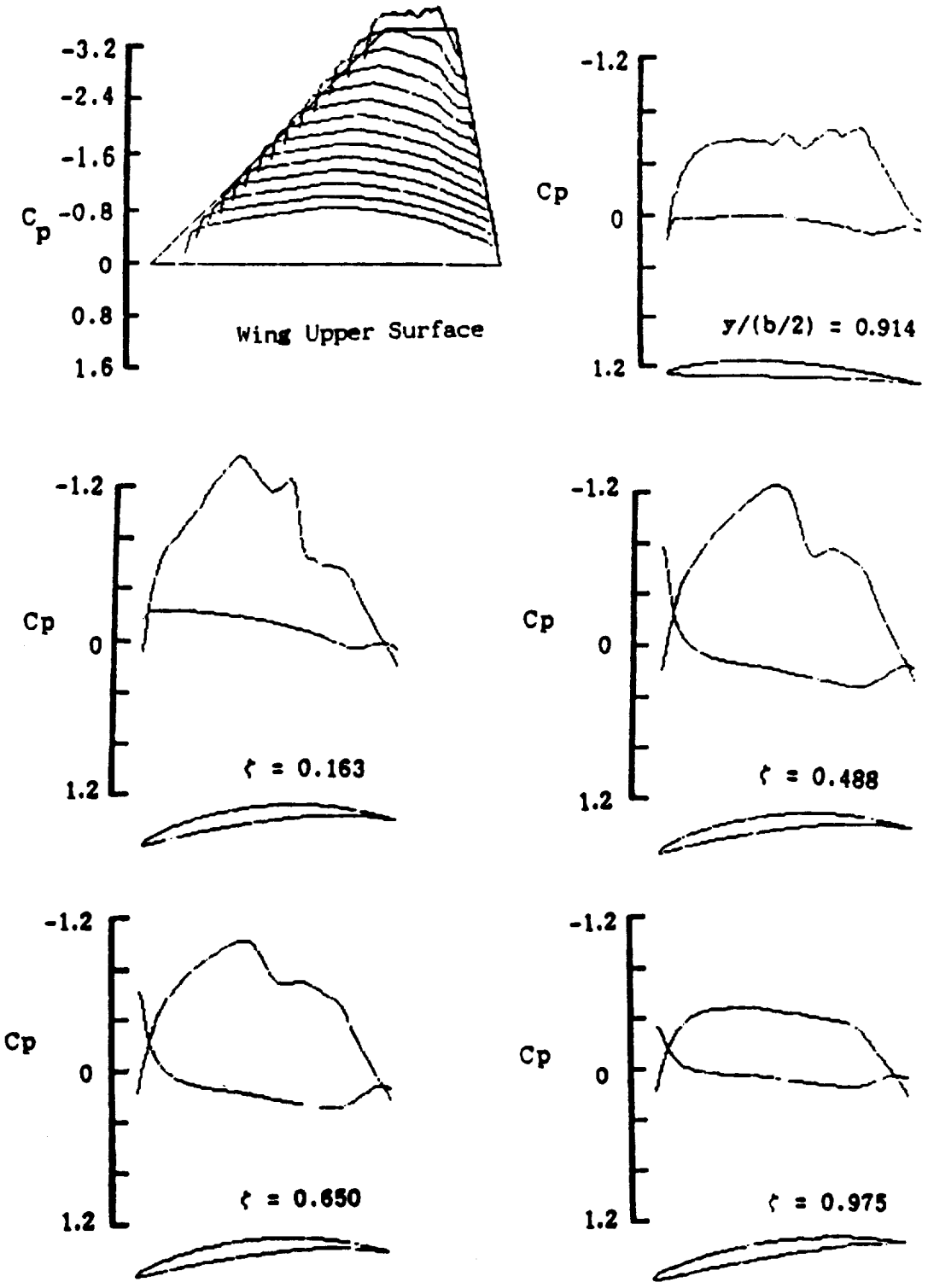

Fig. 9. Calculated wing-winglet C_p distributions for configuration F at M = 0.8, $\alpha = 0°$.

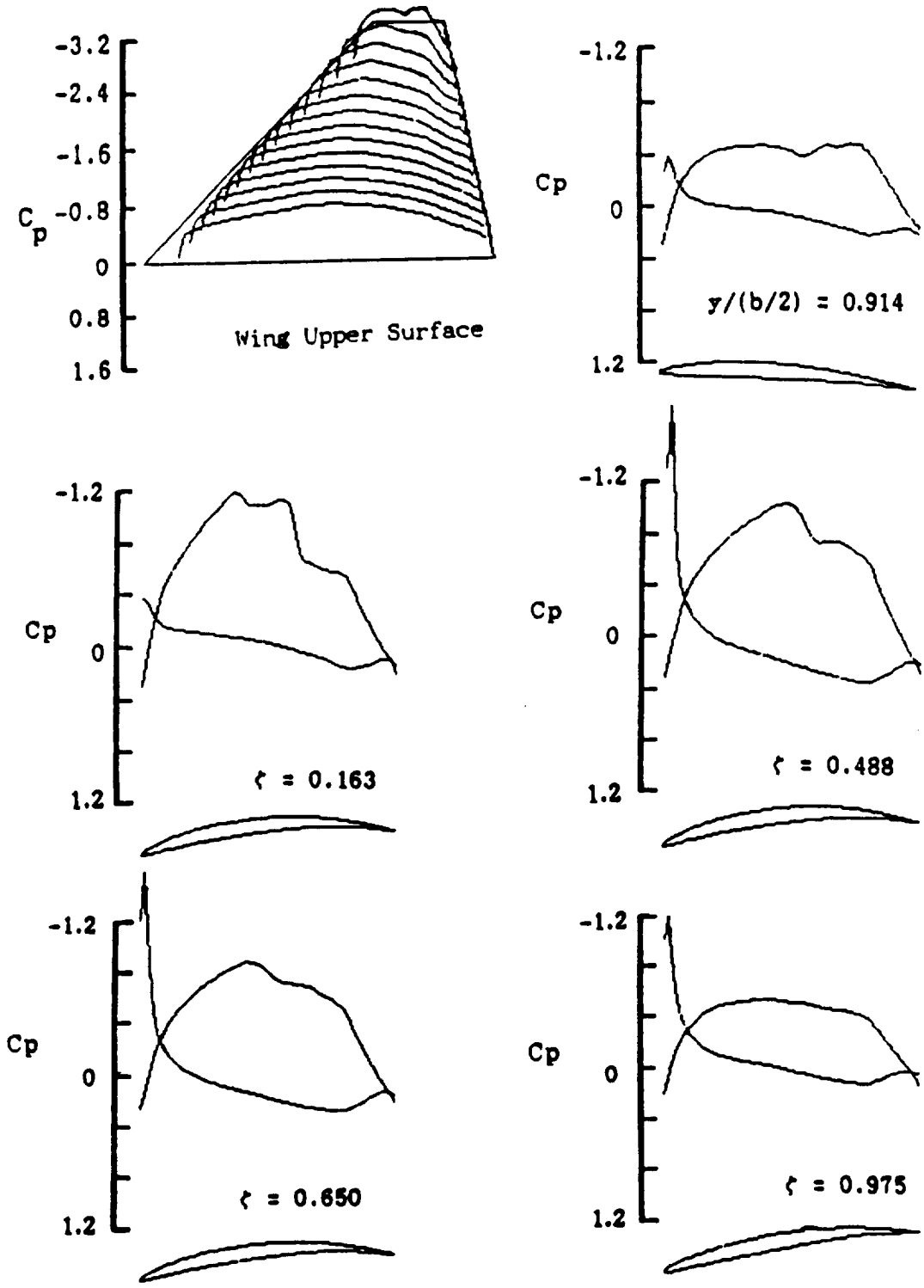

Fig. 10. Calculated wing-winglet C_p distributions for configuration F at M = 0.8, α = -1.5°.

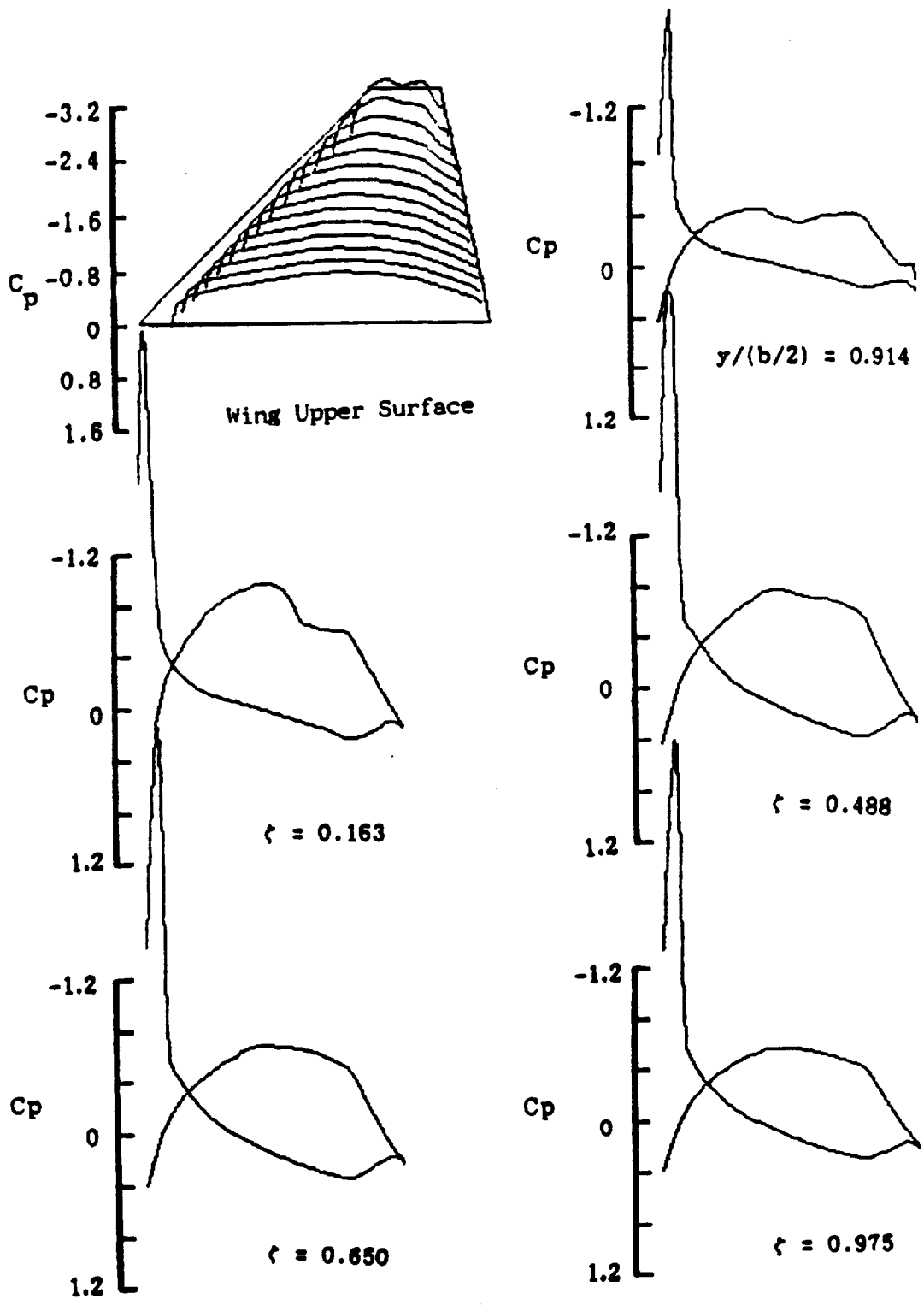

Fig. 11. Calculated wing-winglet C_p distributions for configuration F at M = 0.8, α = -4°.

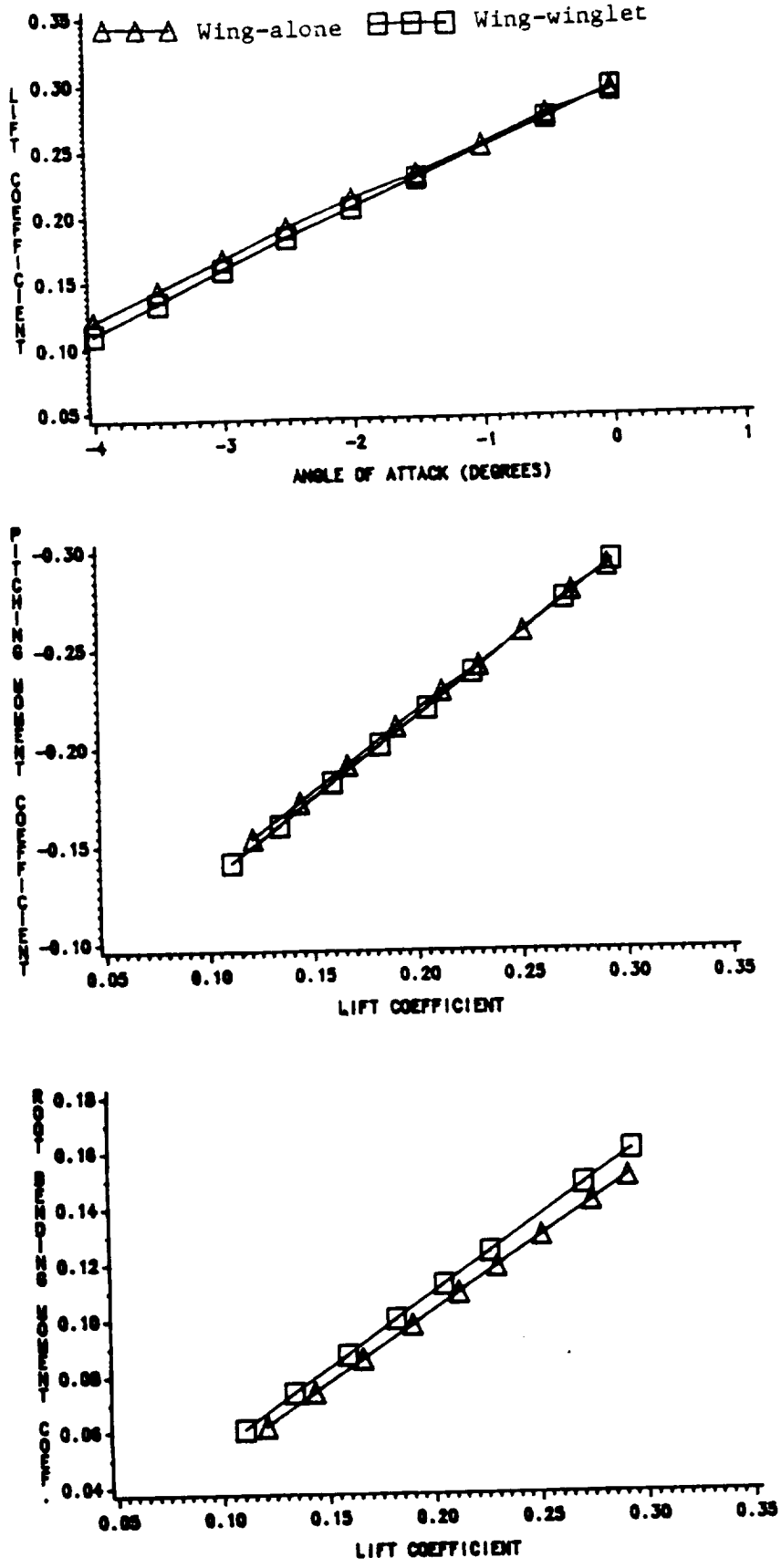

Fig. 12. Predicted performance of wing-alone and wing-winglet configurations G at M = 0.8; C_L - α, C_m - C_L, C_B - C_L.

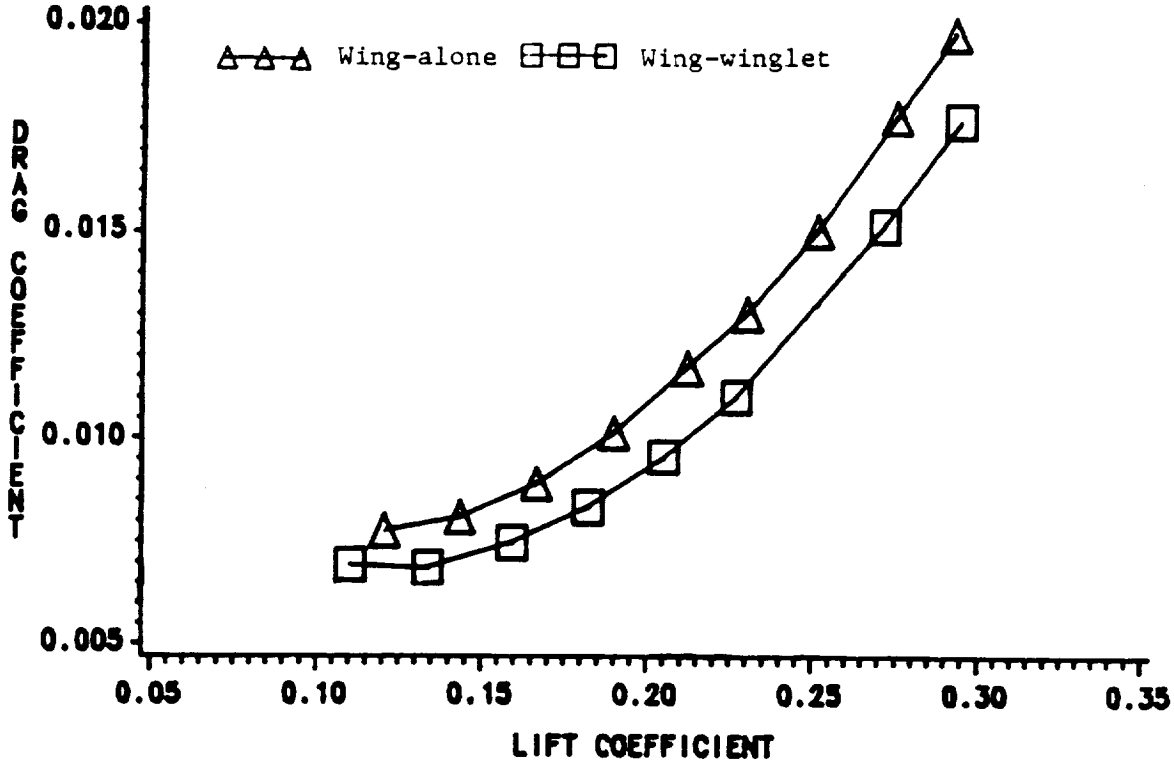

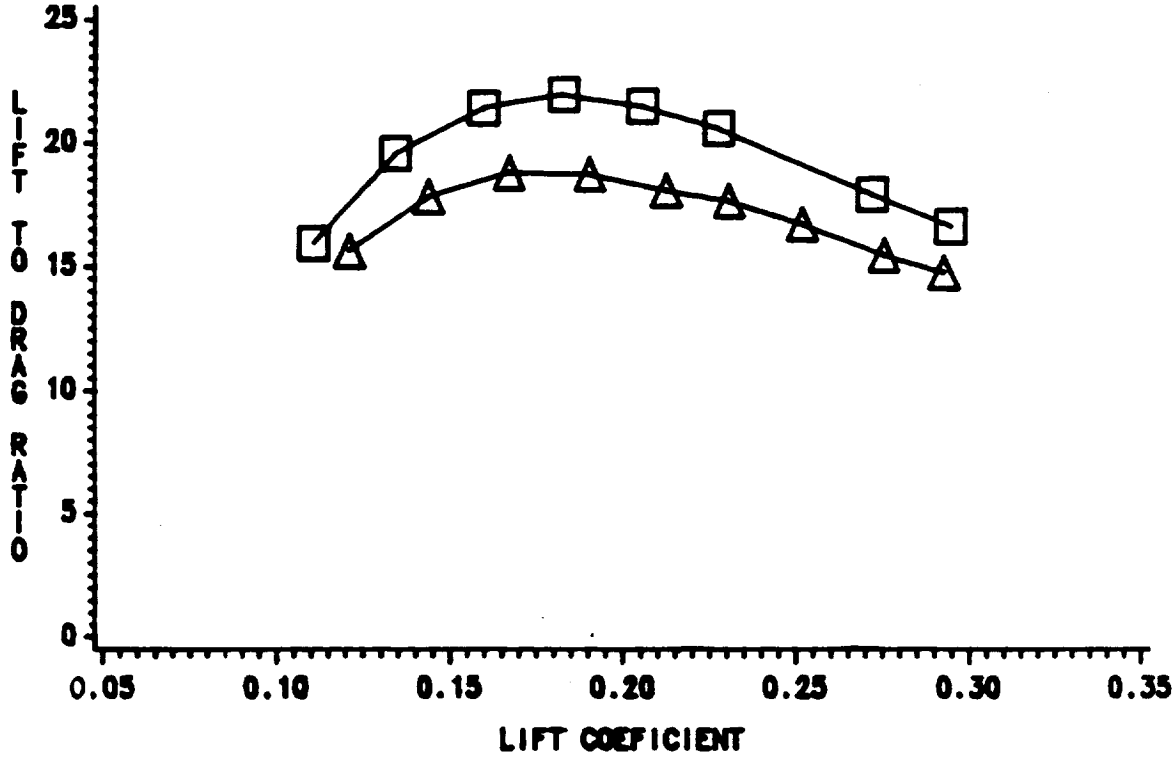

Fig. 12. (Concluded) - Predicted performance of wing-wlone and wing-winglet configurations G at M = 0.8; drag polar and L/D - C_L.

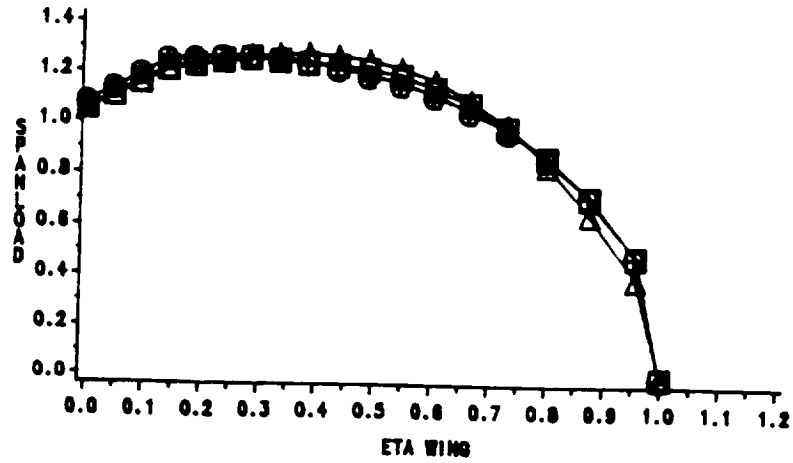

Wing-alone

DIAMOND: A=1 TRIANGLE: A=2
CIRCLE: A=0 SQUARE: A=4

Angle of attack (deg)

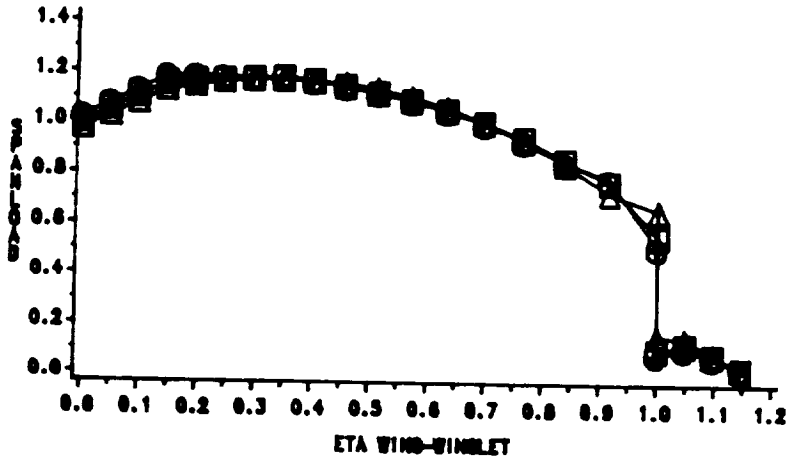

Wing-winglet

Fig. 13. Calculated normalized spanloads for wing-alone and wing-winglet configurations G at M = 0.8.

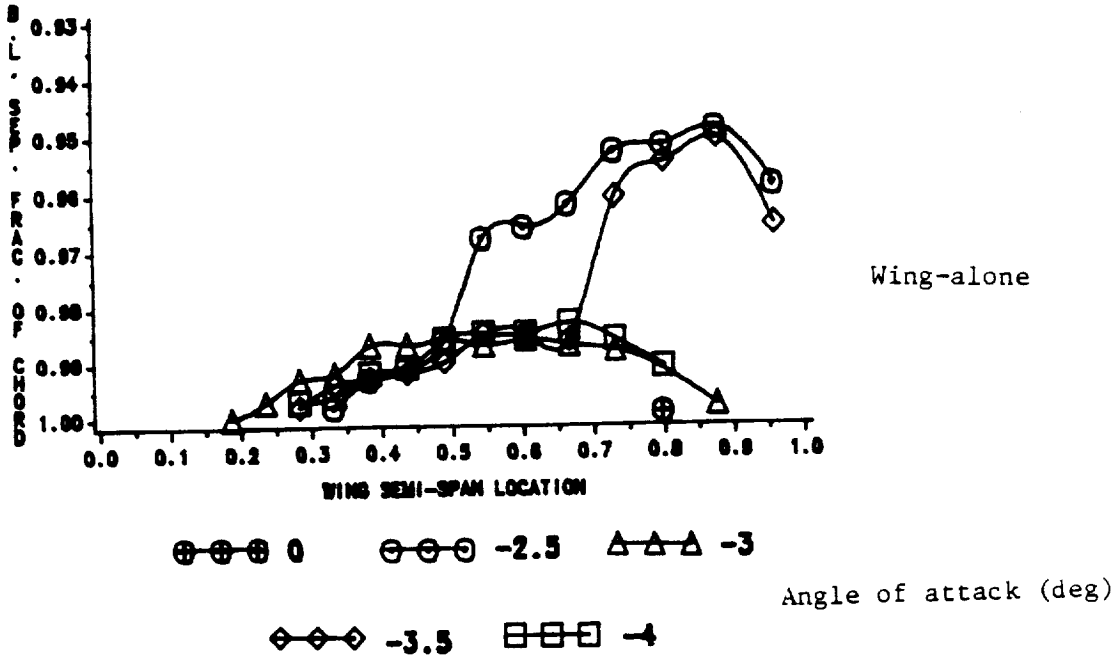

Fig. 14. Predicted upper surface boundary layer separation locations for wing-alone and wing-winglet configurations G at M = 0.8.

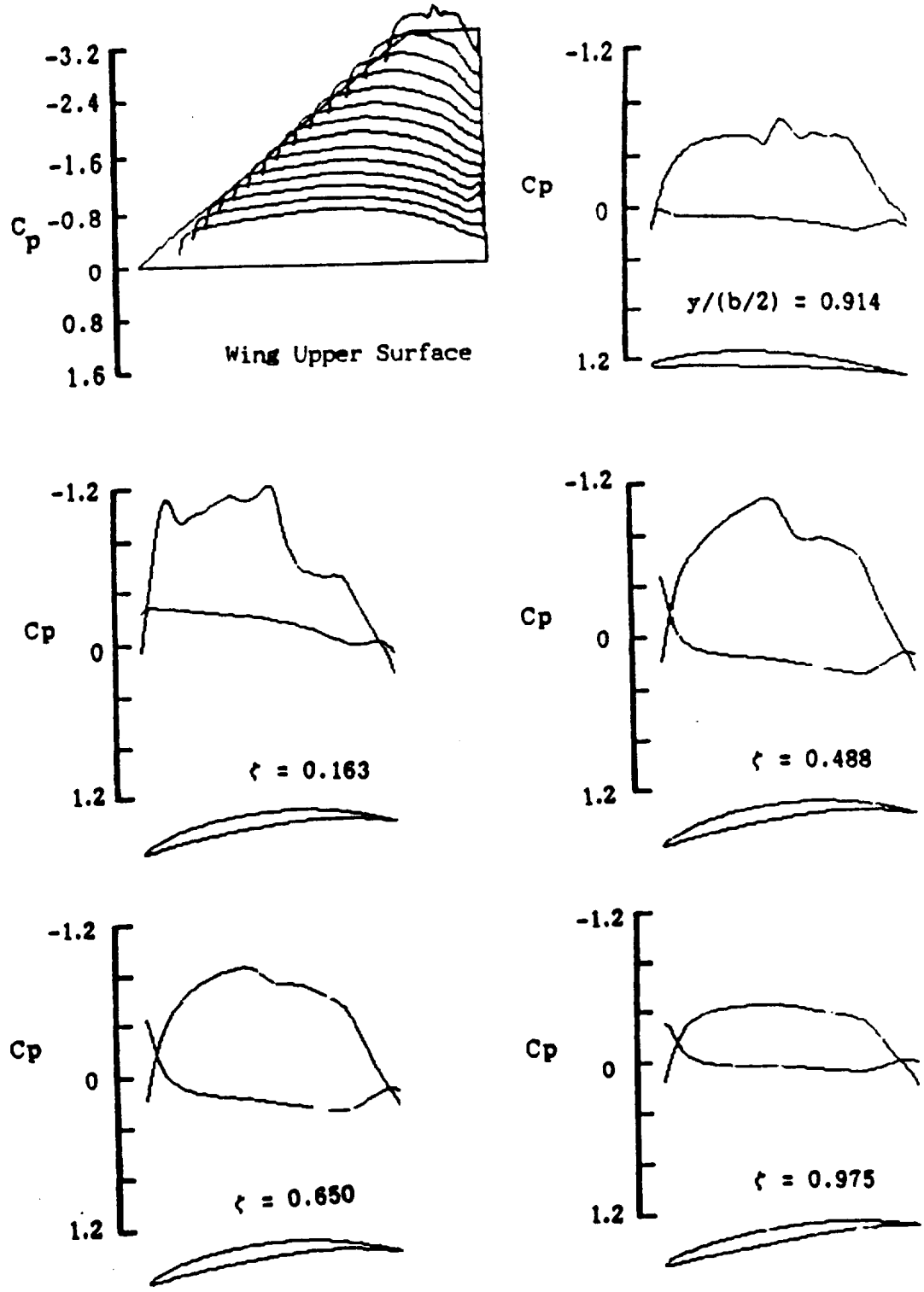

Fig. 15. Calculated wing-winglet C_p distributions for configuration G at M = 0.8, α = 0°.

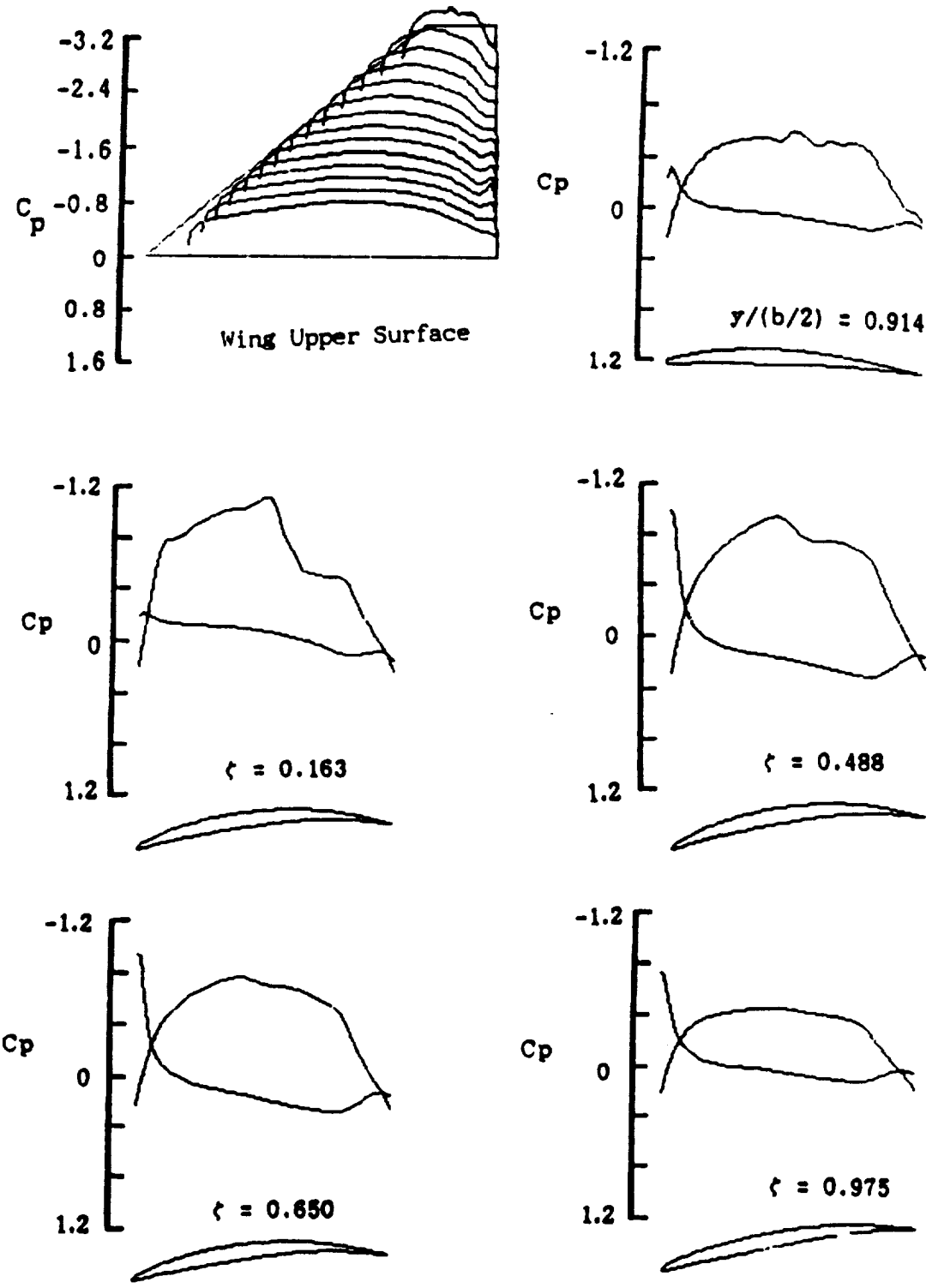

Fig. 16. Calculated wing-winglet C_p distributions for configuration G at M = 0.8, α = -1.5°.

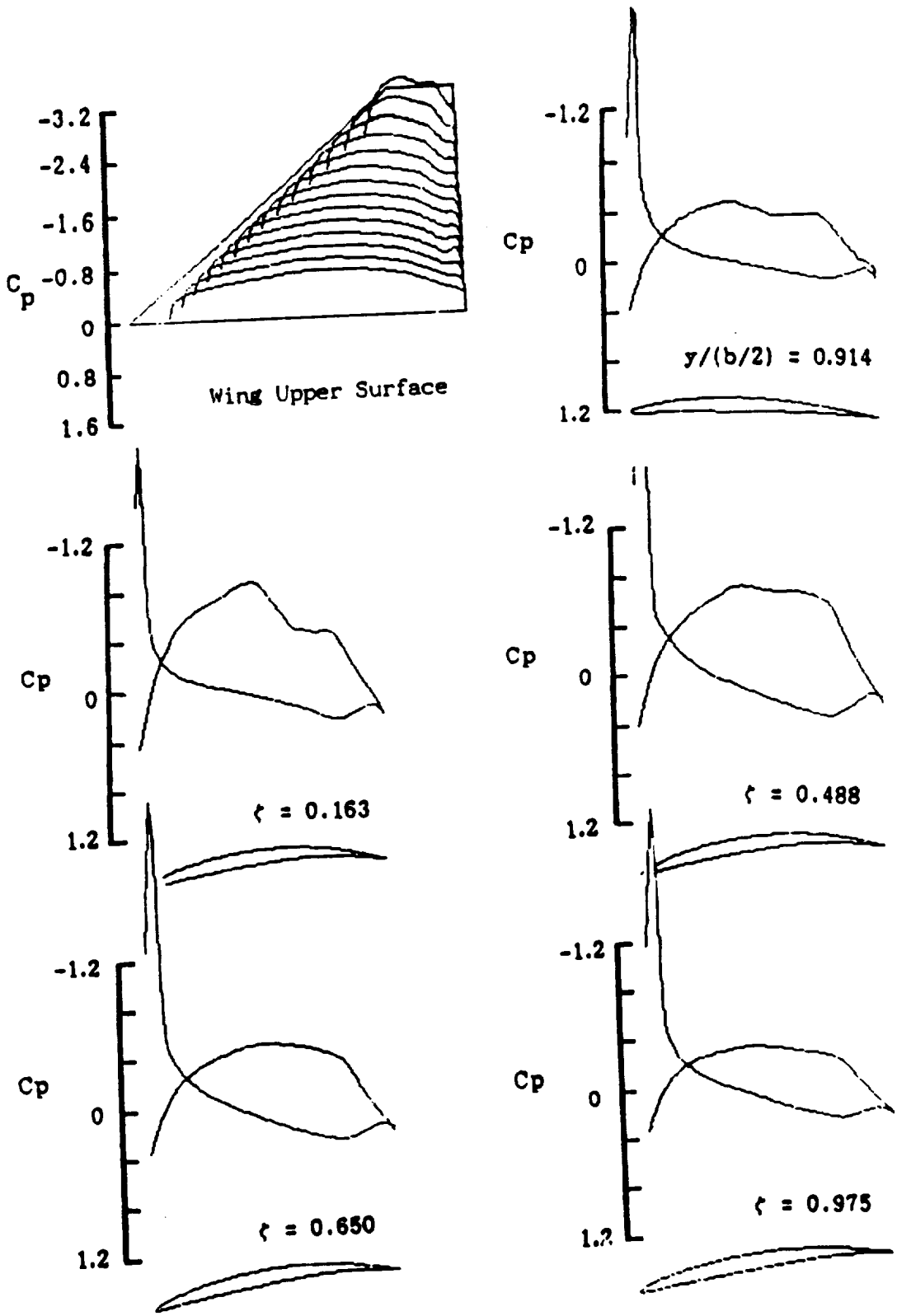

Fig. 17. Calculated wing-winglet C_p distributions for configuration G at M = 0.8, $\alpha = -4°$.

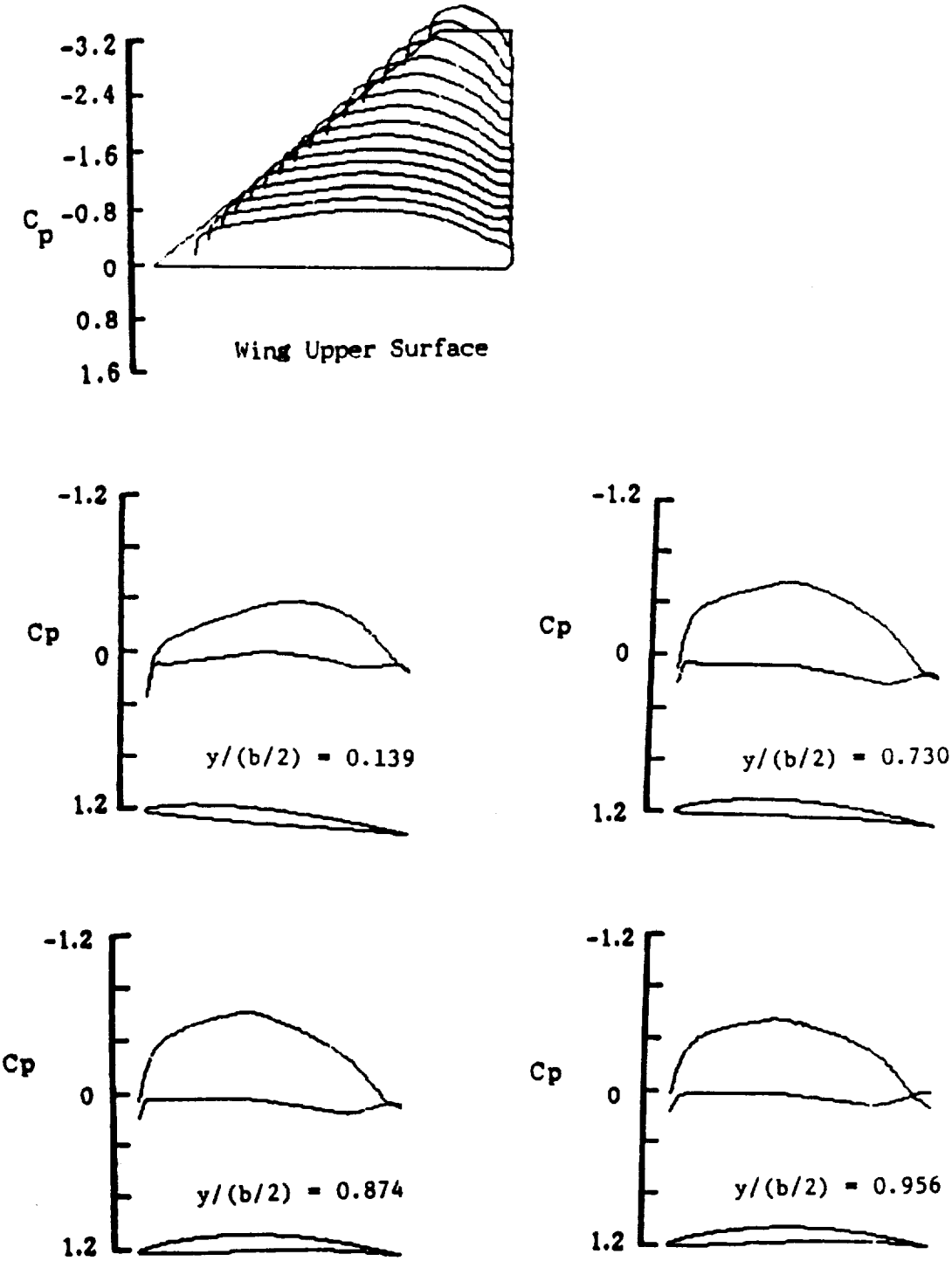

Fig. 18. Calculated wing-alone C_p distributions for configuration G at M = 0.8, $\alpha = 0°$.

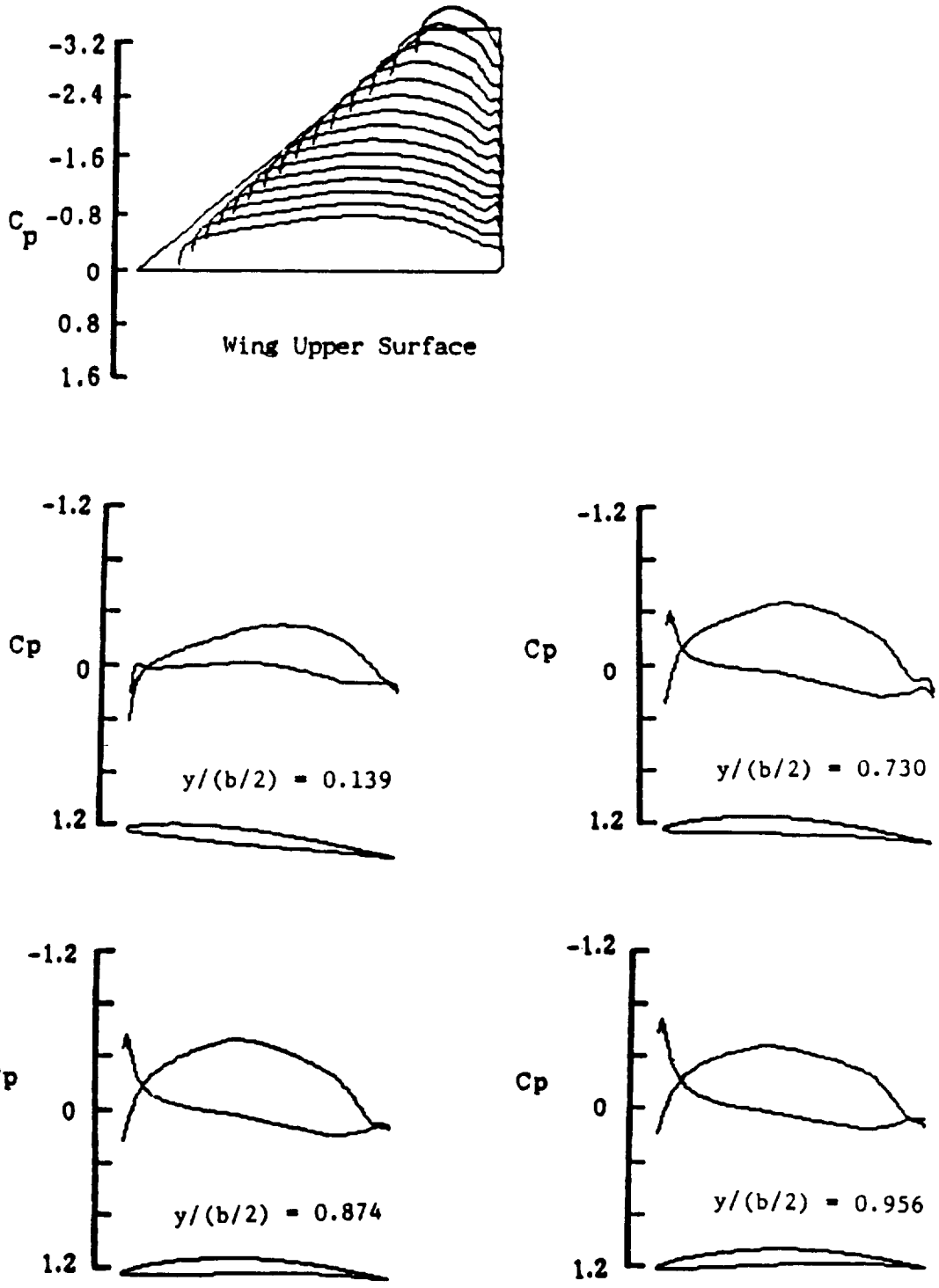

Fig. 19. Calculated wing-alone C_p distributions for configuration G at M = 0.8, $\alpha = -2°$.

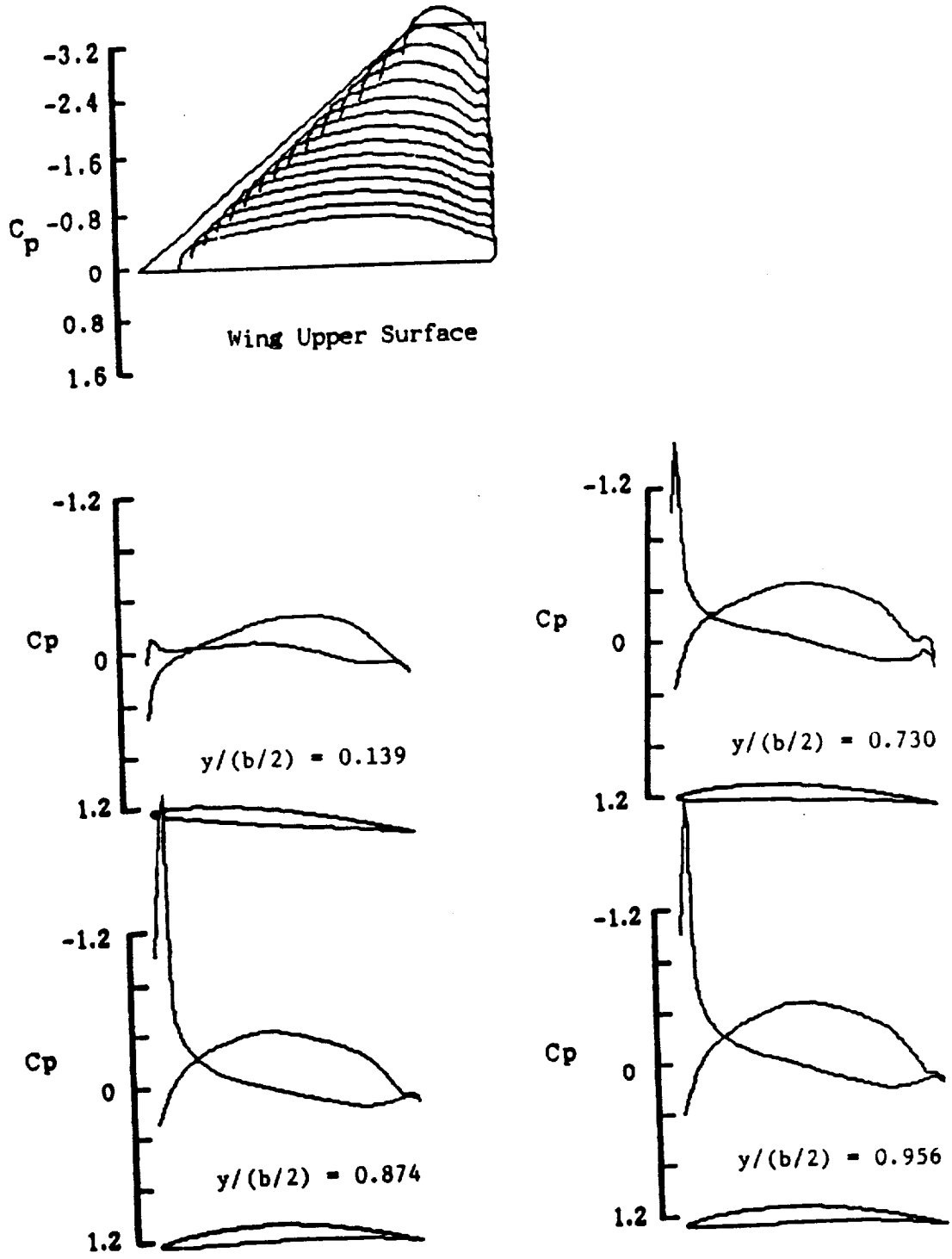

Fig. 20. Calculated wing-alone C_p distributions for configuration G at M = 0.8, $\alpha = -4^\circ$.

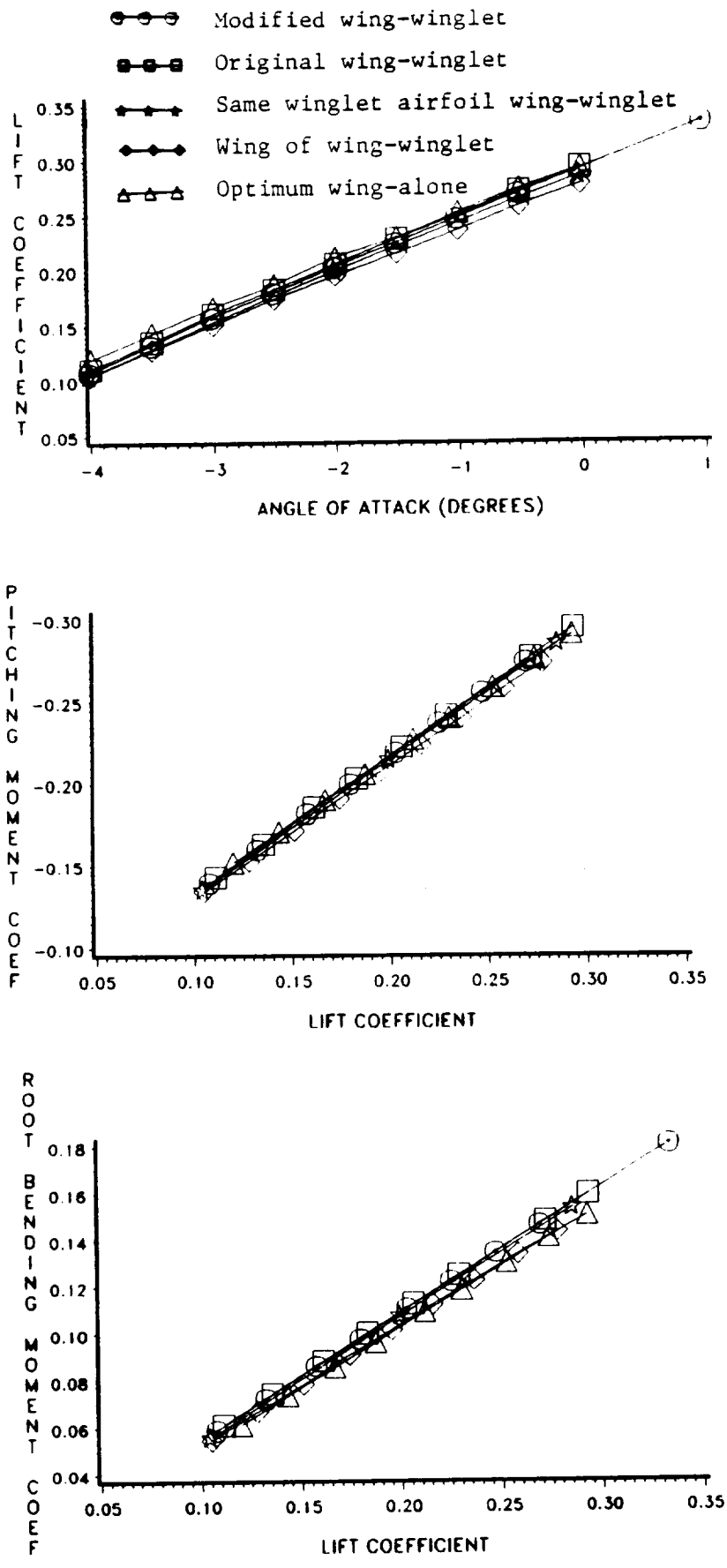

Fig. 21. Predicted performance of wing-alone and wing-winglet configurations cropped delta G at M = 0.8; $C_L - \alpha$, $C_m - C_L$, $C_B - C_L$.

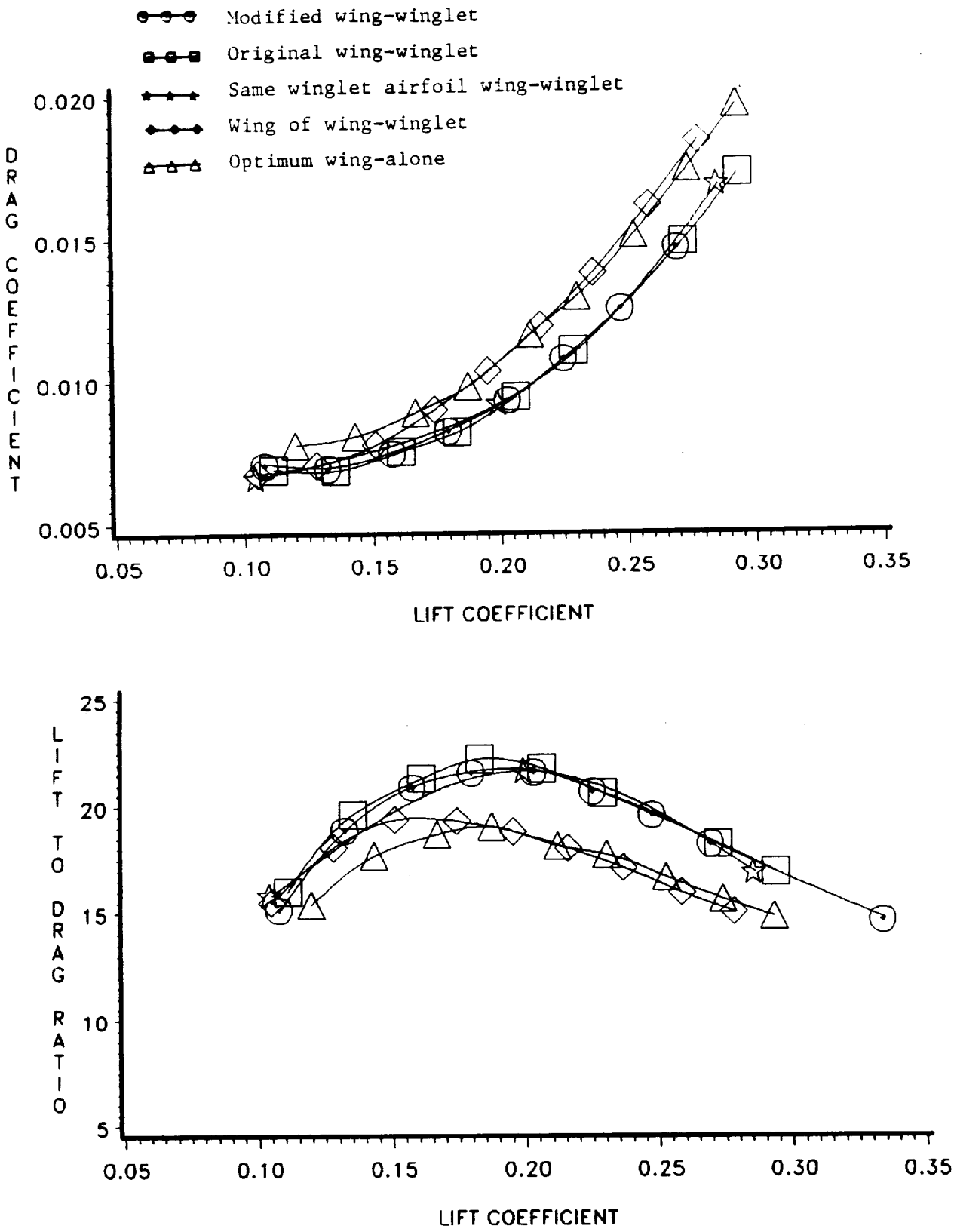

Fig. 21. (Concluded) - Predicted performance of wing-alone and wing-winglet configurations cropped delta G at M = 0.8; drag polar and L/D - C_L.

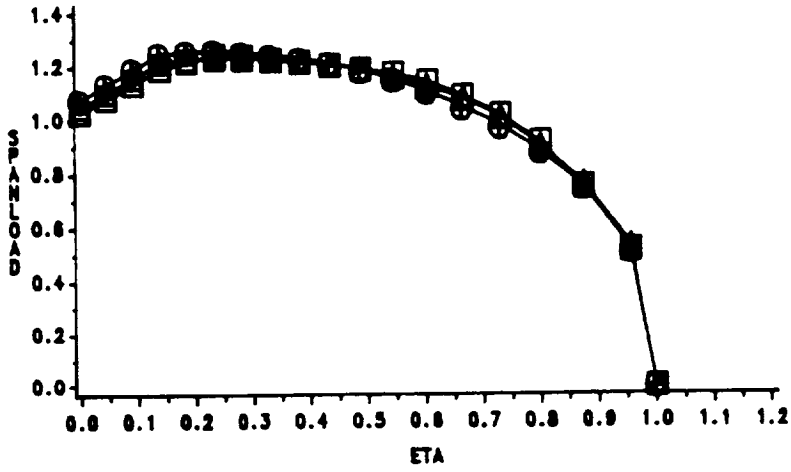

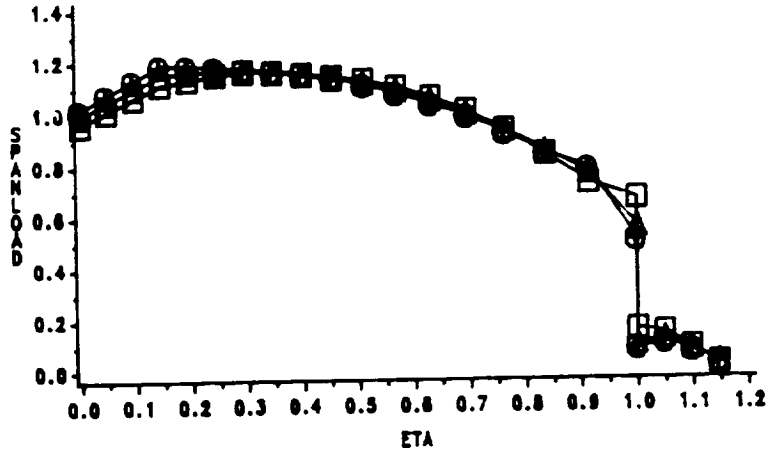

Fig. 22. Calculated normalized spanloads for wing-alone and wing-winglet configurations cropped delta G, wing of wing-winglet and wing-winglet at M = 0.8.

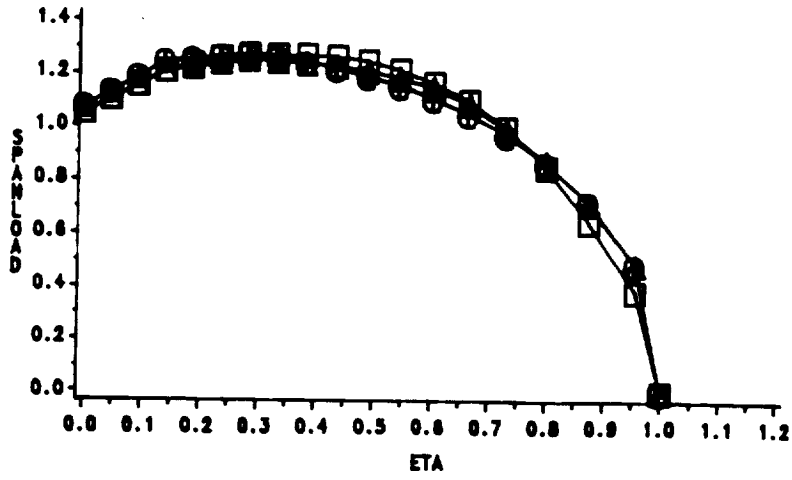

Wing-alone

DIAMOND: A=1 TRIANGLE: A=2
CIRCLE: A=0 SQUARE: A=4

Angle of attack (deg)

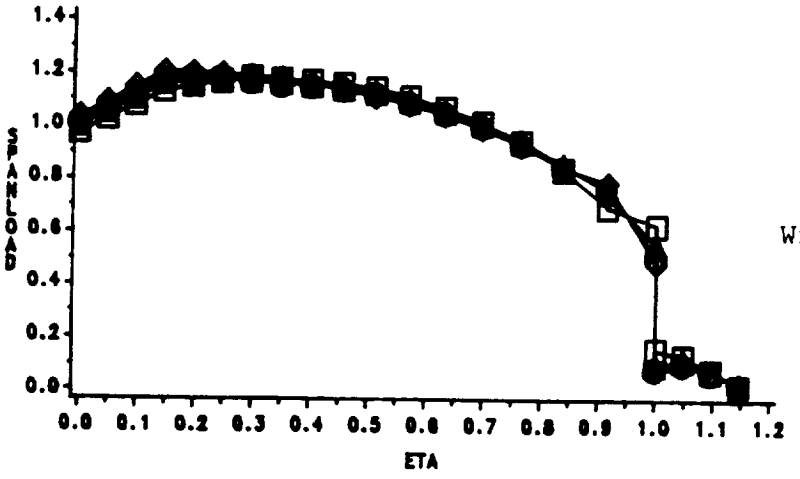

Wing-winglet

Fig. 22 Calculated normalized spanloads for wing-alone and wing-winglet configurations cropped delta G, optimum wing and modified wing-winglet at M = 0.8.

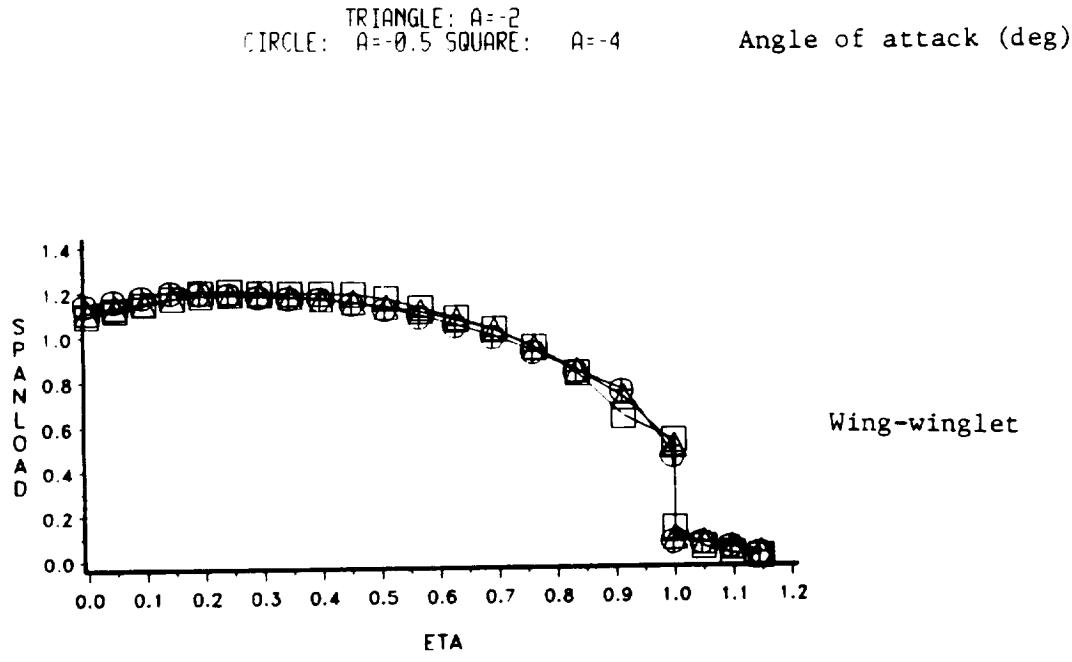

Fig. 22 (Concluded) Calculated normalized spanloads for same winglet airfoil cropped delta G configuration at M = 0.8.

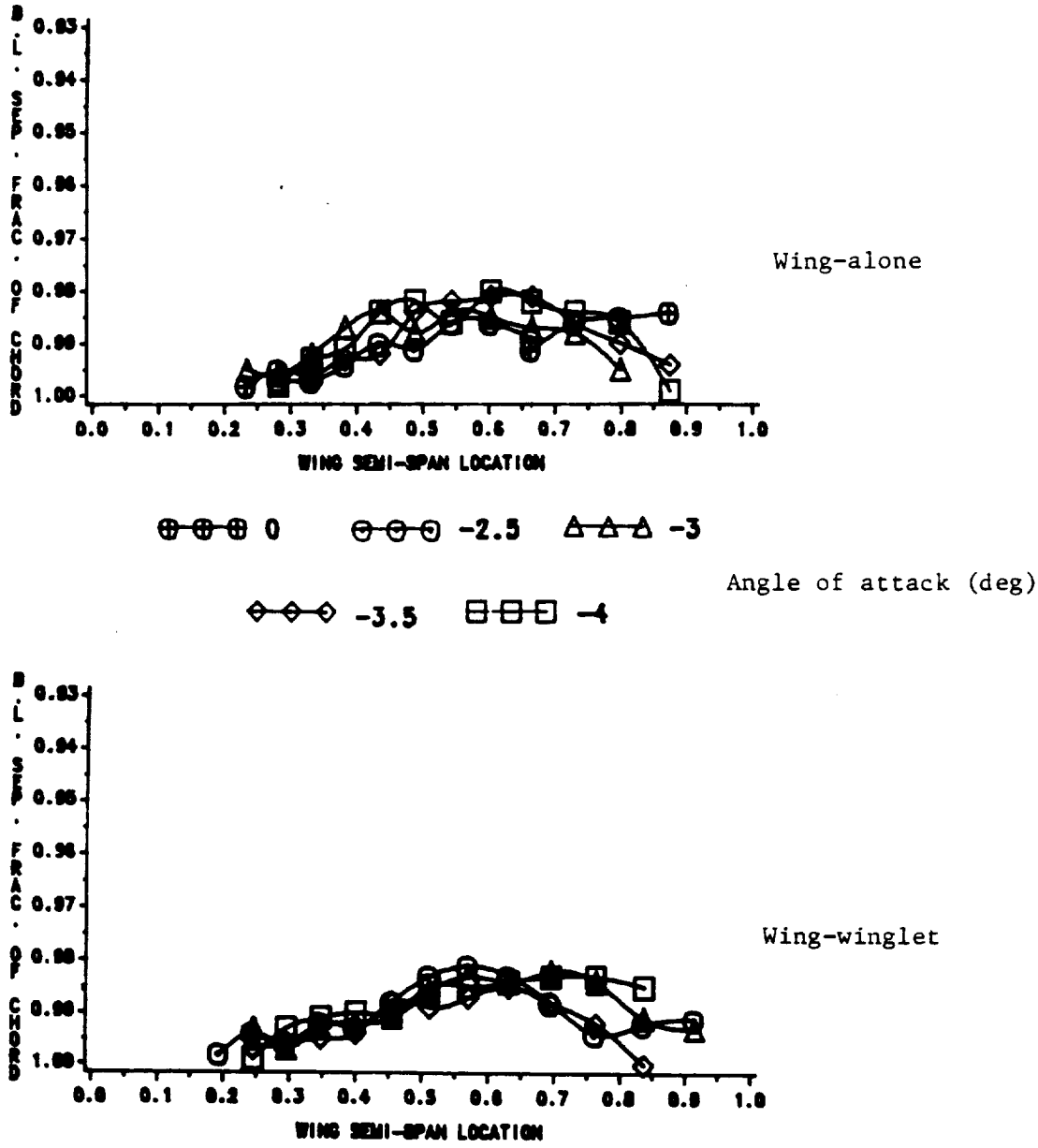

Fig. 23 Predicted upper surface boundary layer separation locations for wing-alone and wing-winglet configurations cropped delta G, optimum wing and modified wing-winglet at M = 0.8.

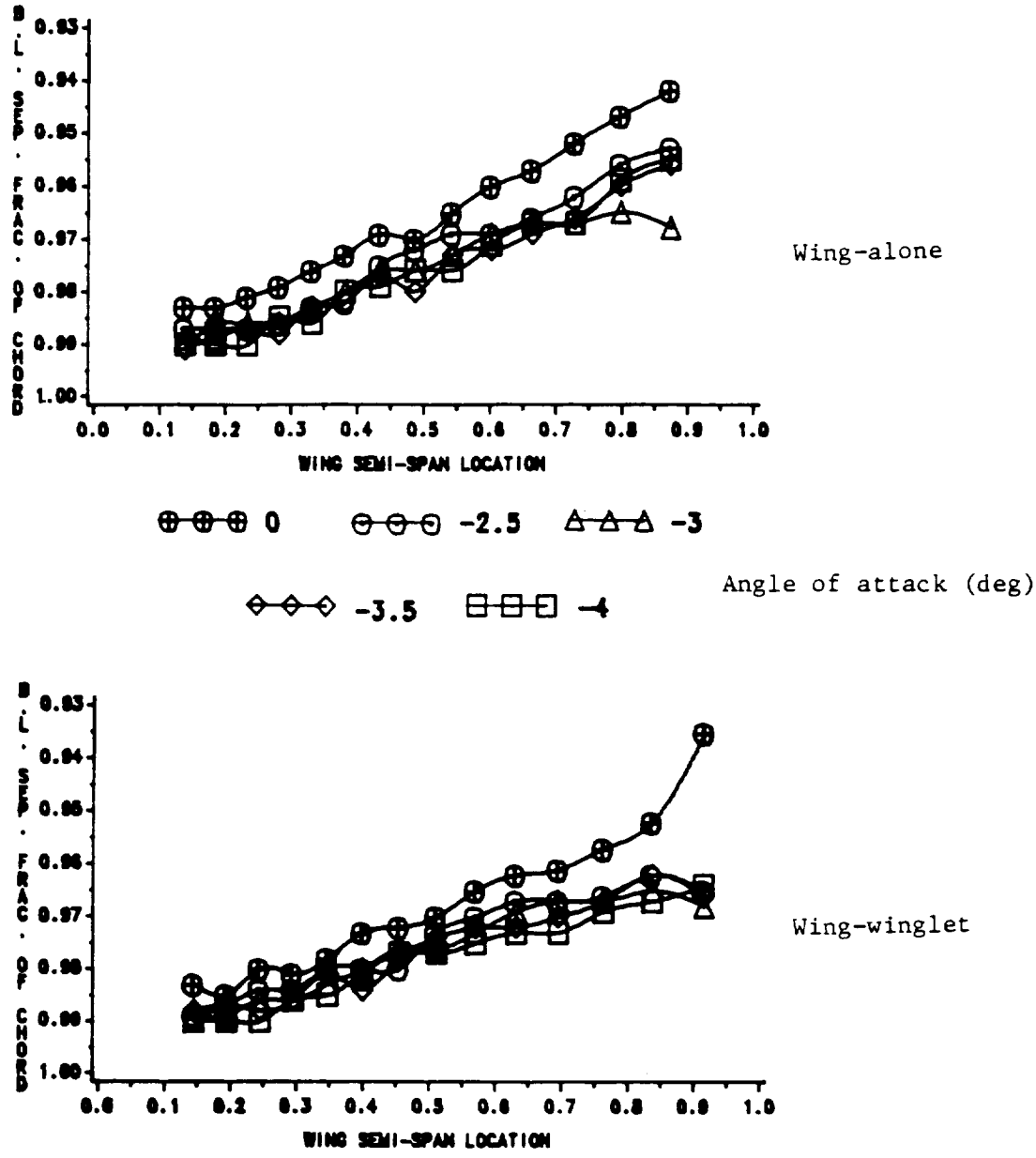

Fig. 23 Predicted upper surface boundary layer separation locations for wing-alone and wing-winglet configurations cropped delta G, wing of wing-winglet and wing-winglet at M = 0.8.

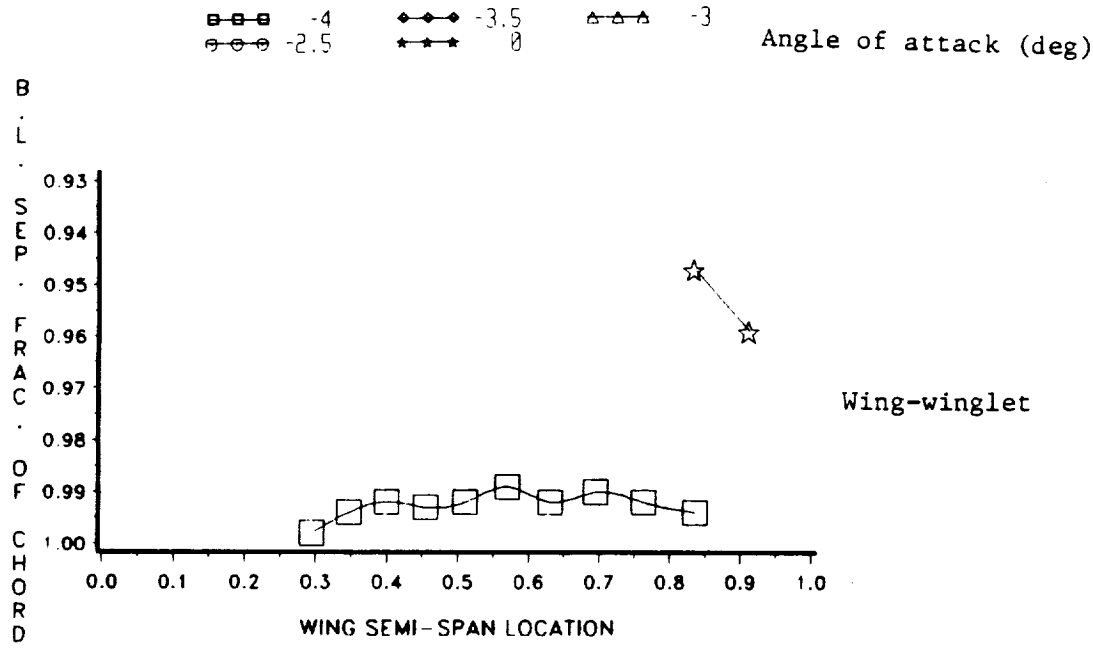

Fig. 23 (Concluded) Predicted upper surface boundary layer separation locations for same winglet airfoil cropped delta G configuration at M = 0.8.

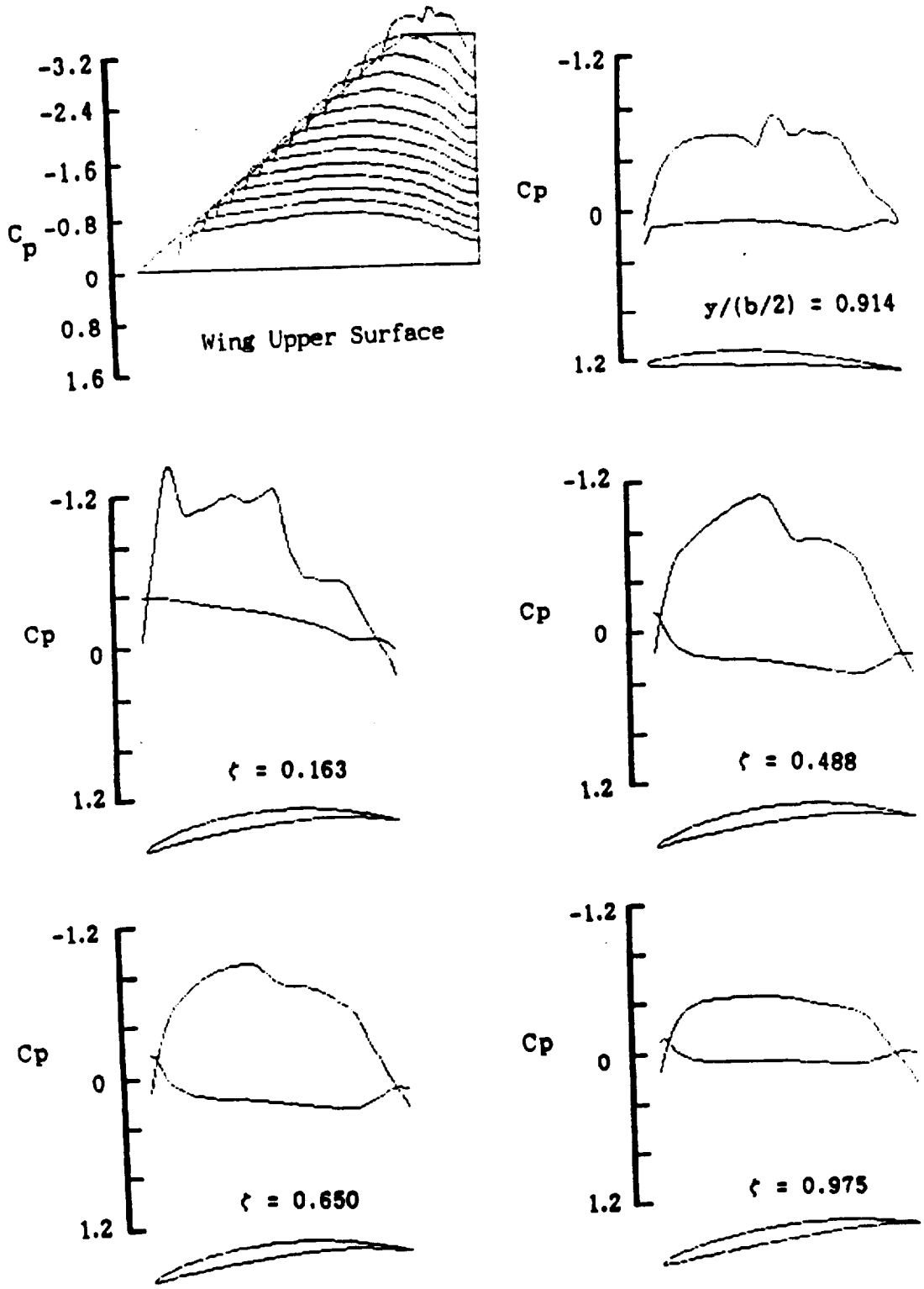

Fig. 24 Calculated wing-winglet C_p distributions for configuration cropped delta G at M = 0.8, $\alpha = 0°$.

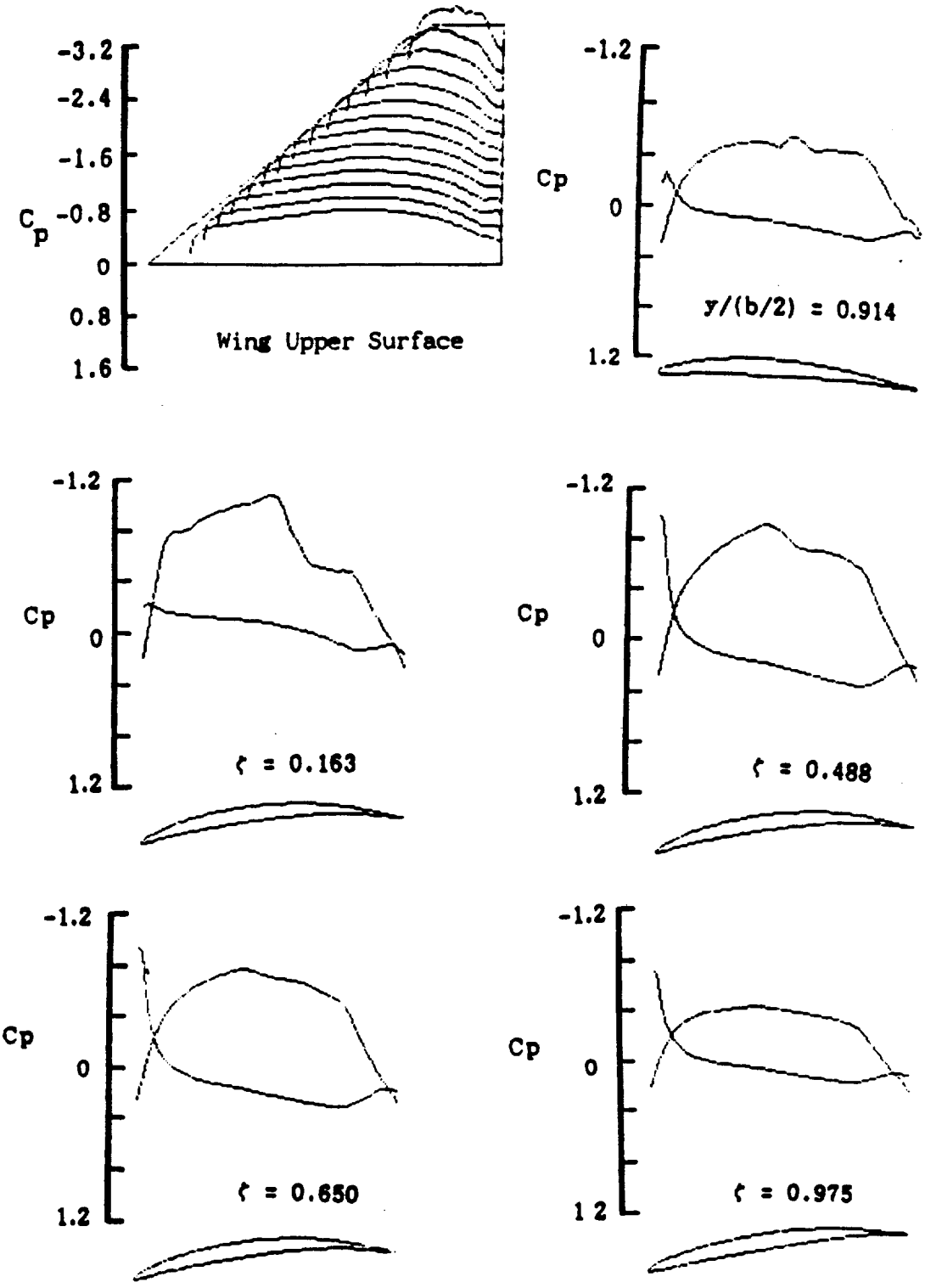

Fig. 25 Calculated wing-winglet C_p distributions for configuration cropped delta G at M = 0.8, α = -2°.

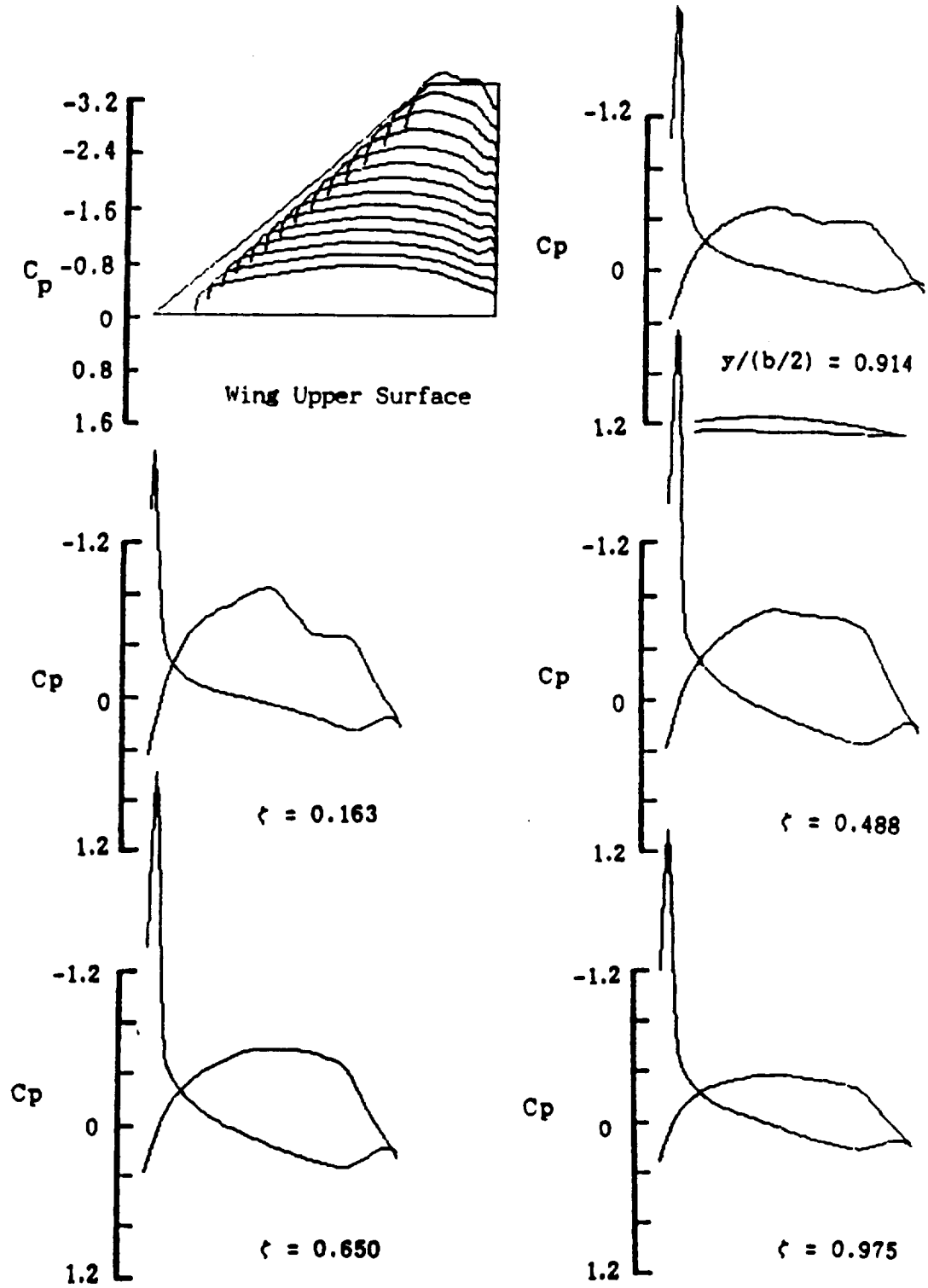

Fig. 26 Calculated wing-winglet C_p distributions for configuration cropped delta G at M = 0.8, $\alpha = -4^\circ$.

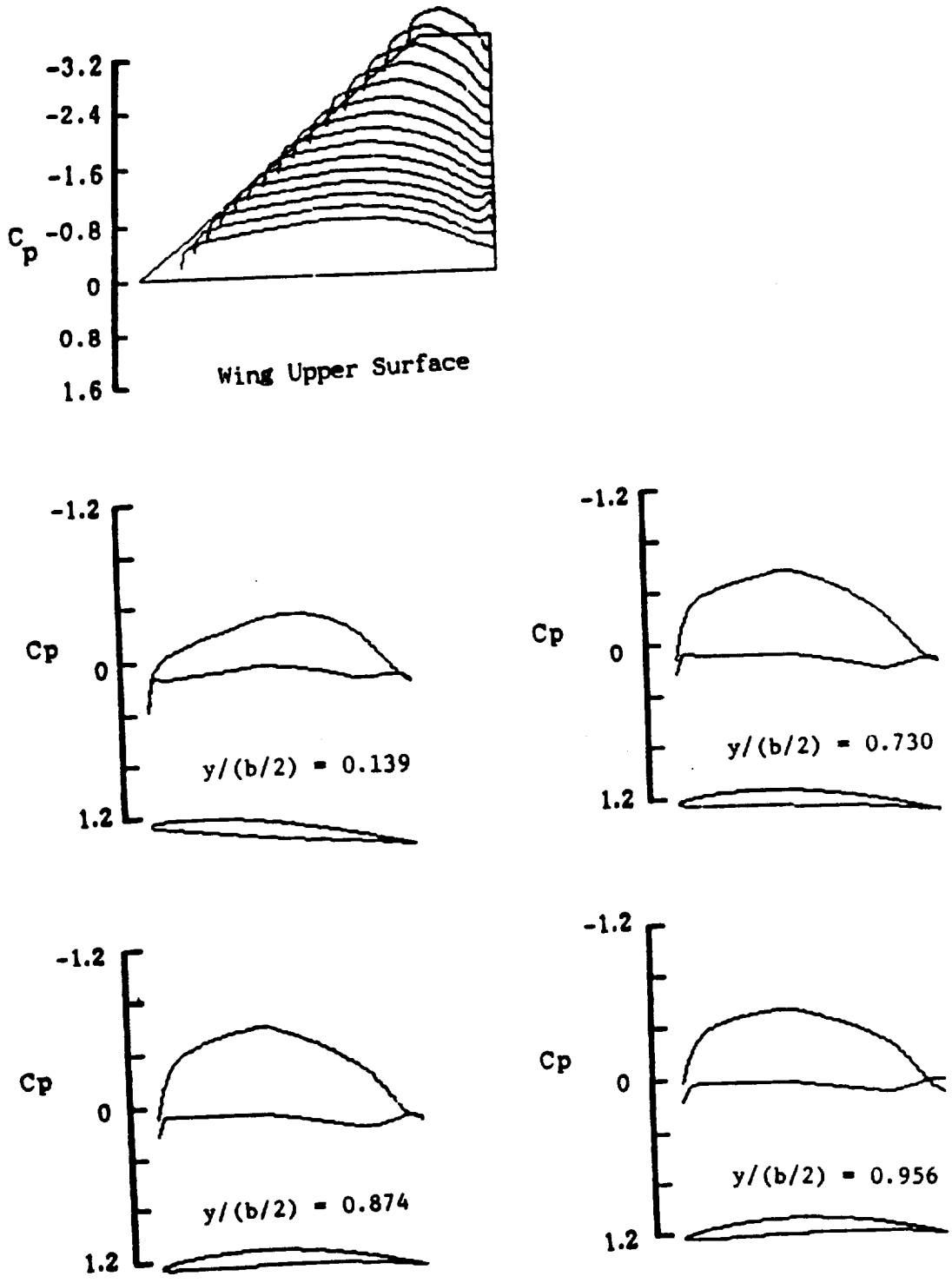

Fig. 27 Calculated wing-alone C_p distributions for configuration cropped delta G at M = 0.8, $\alpha = 0°$.

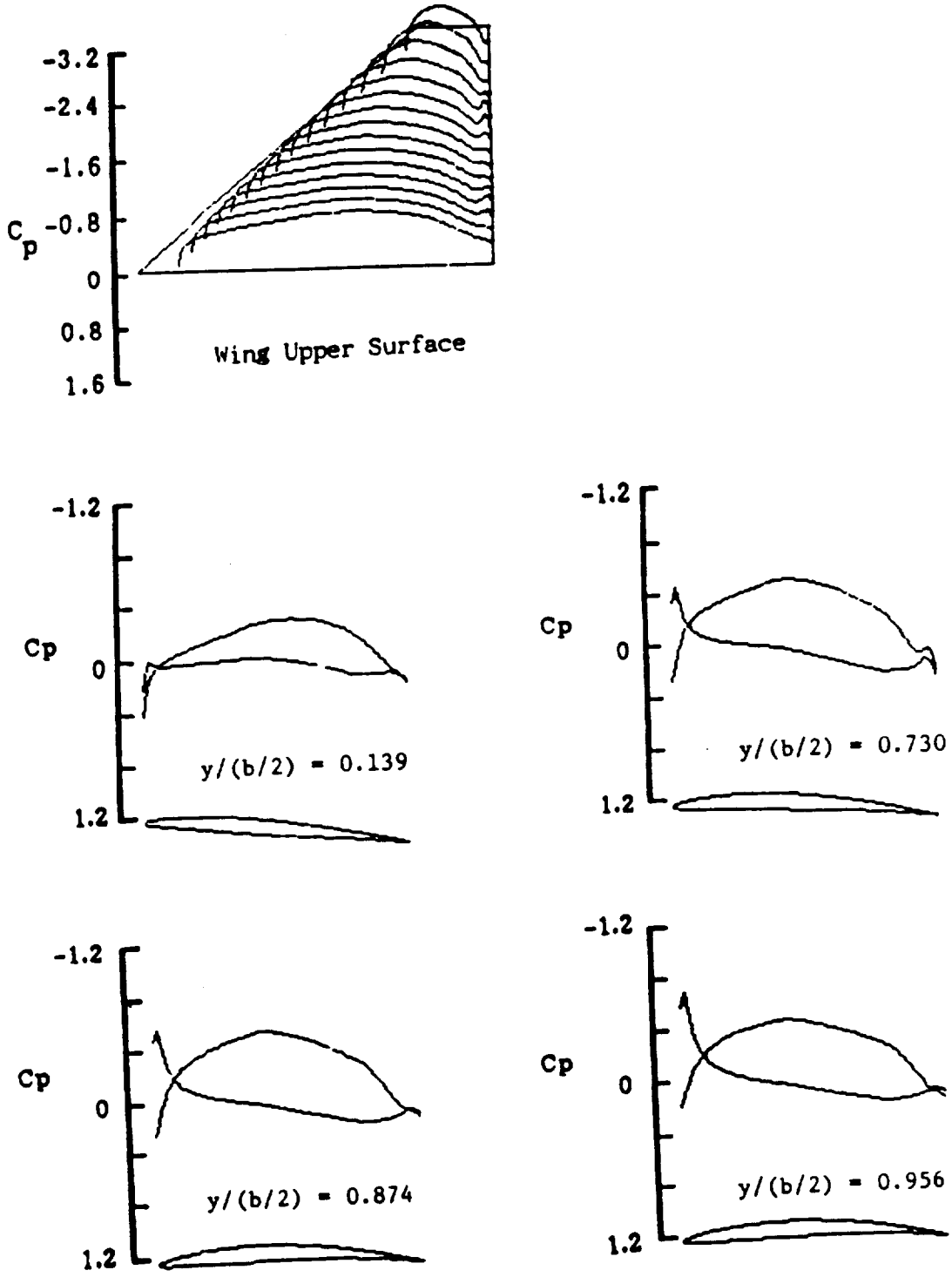

Fig. 28 Calculated wing-alone C_p distributions for configuration cropped delta G at M = 0.8, α = -2°.

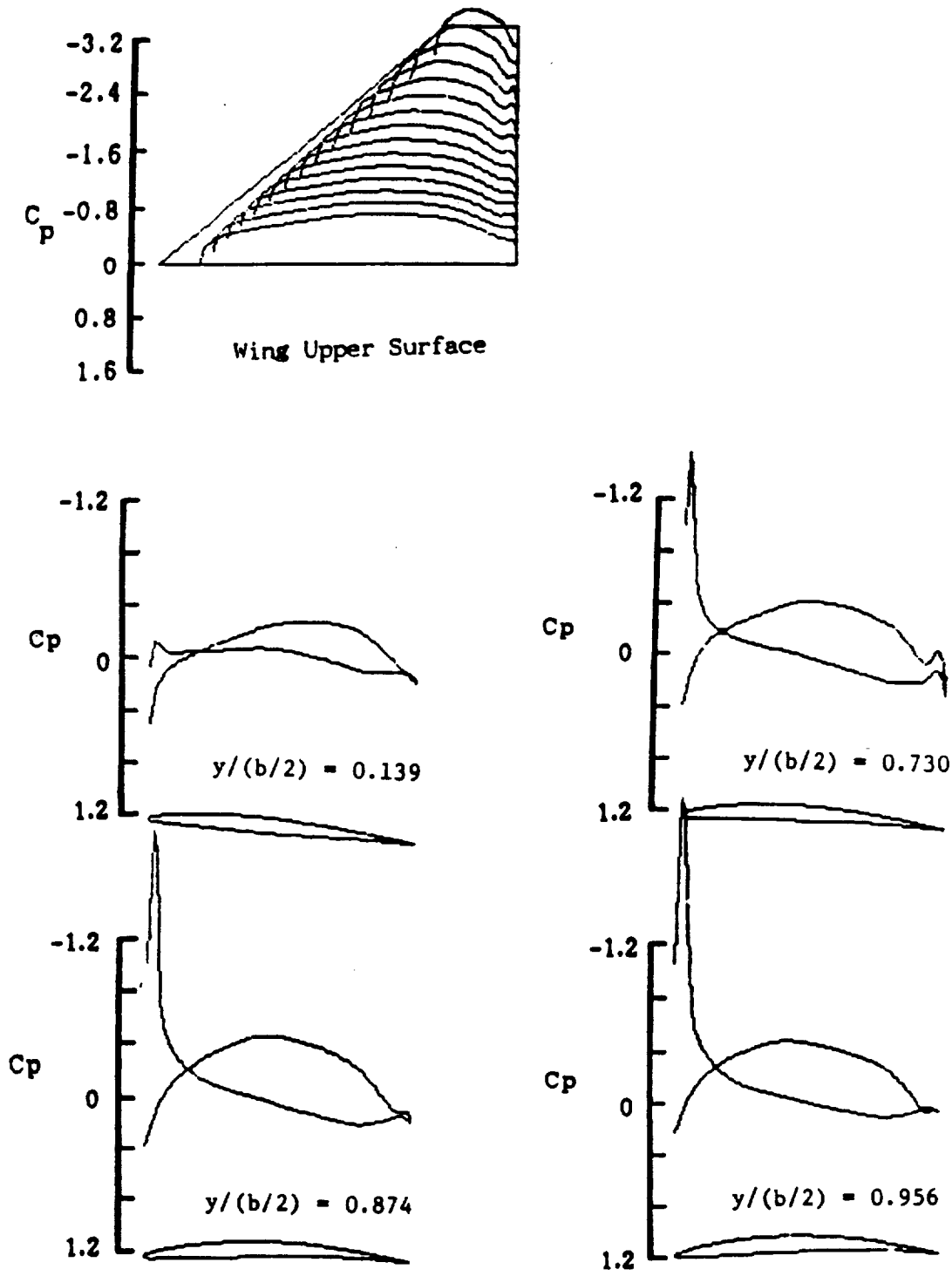

Fig. 29 Calculated wing-alone C_p distributions for configuration cropped delta G at M = 0.8, α = -4°.

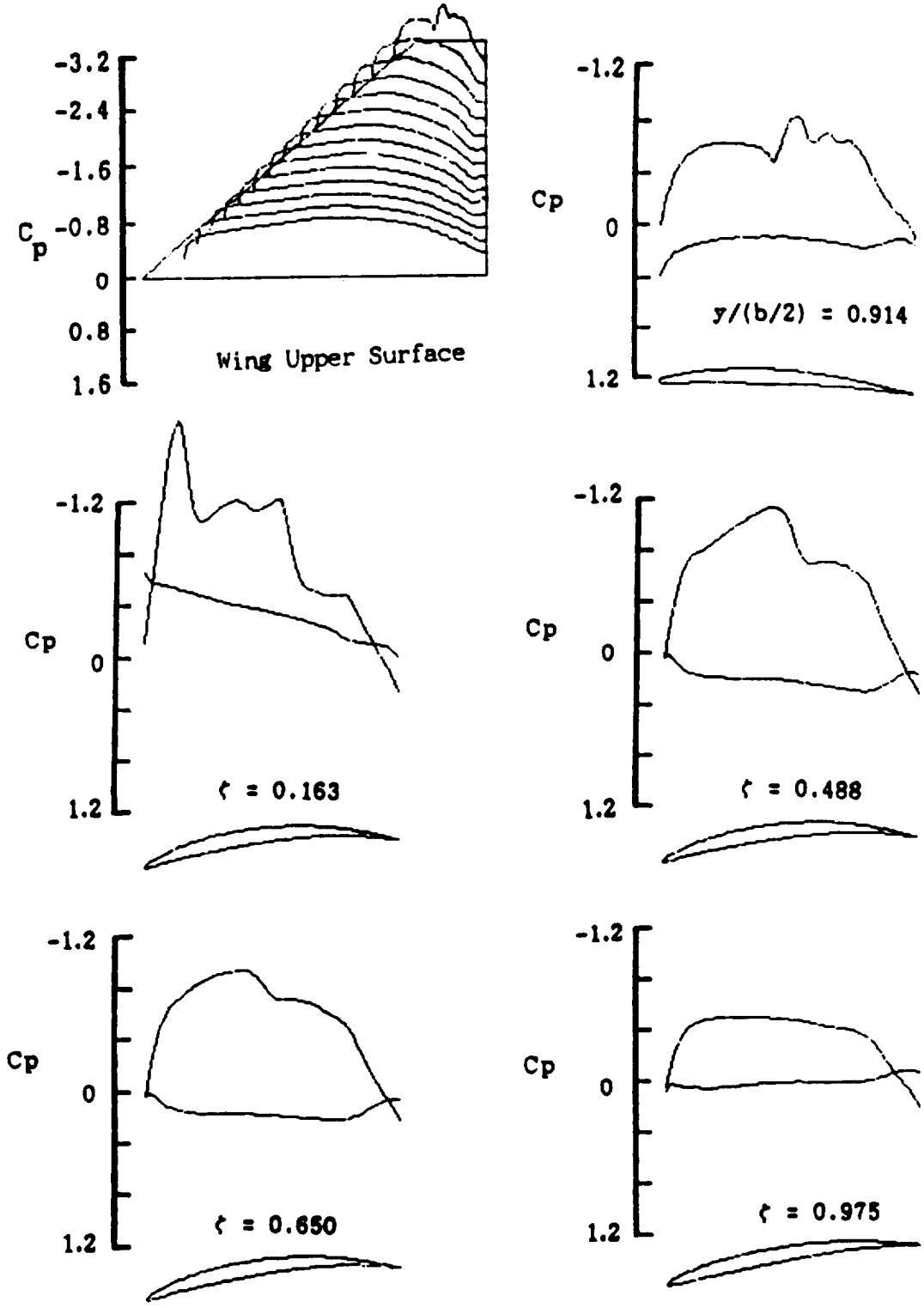

Fig. 30 Calculated wing-winglet C_p distributions for configuration modified cropped delta G at M = 0.8, α = +1°.

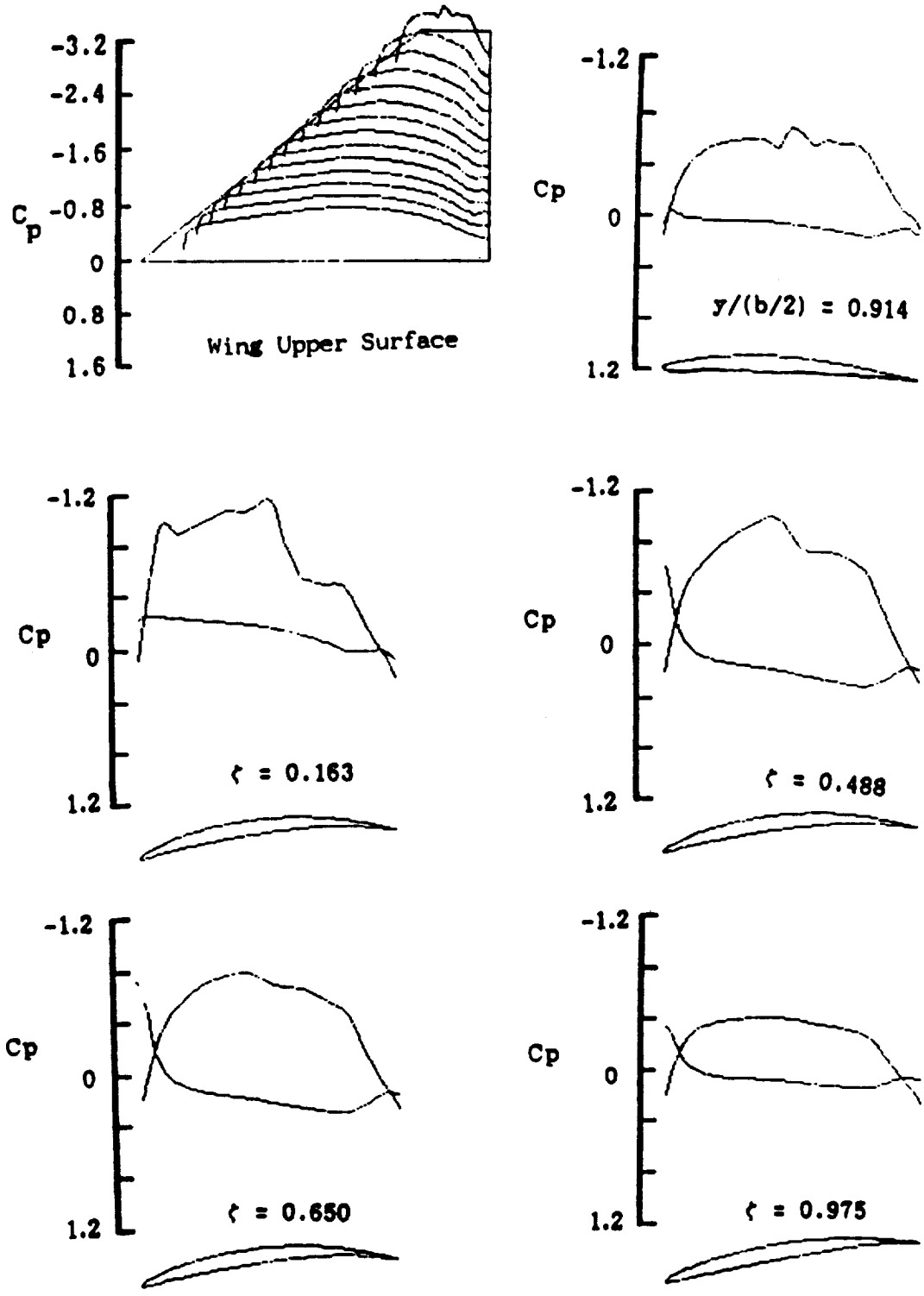

Fig. 31 Calculated wing-winglet C_p distributions for configuration modified cropped delta G at M = 0.8, α = -0.5°.

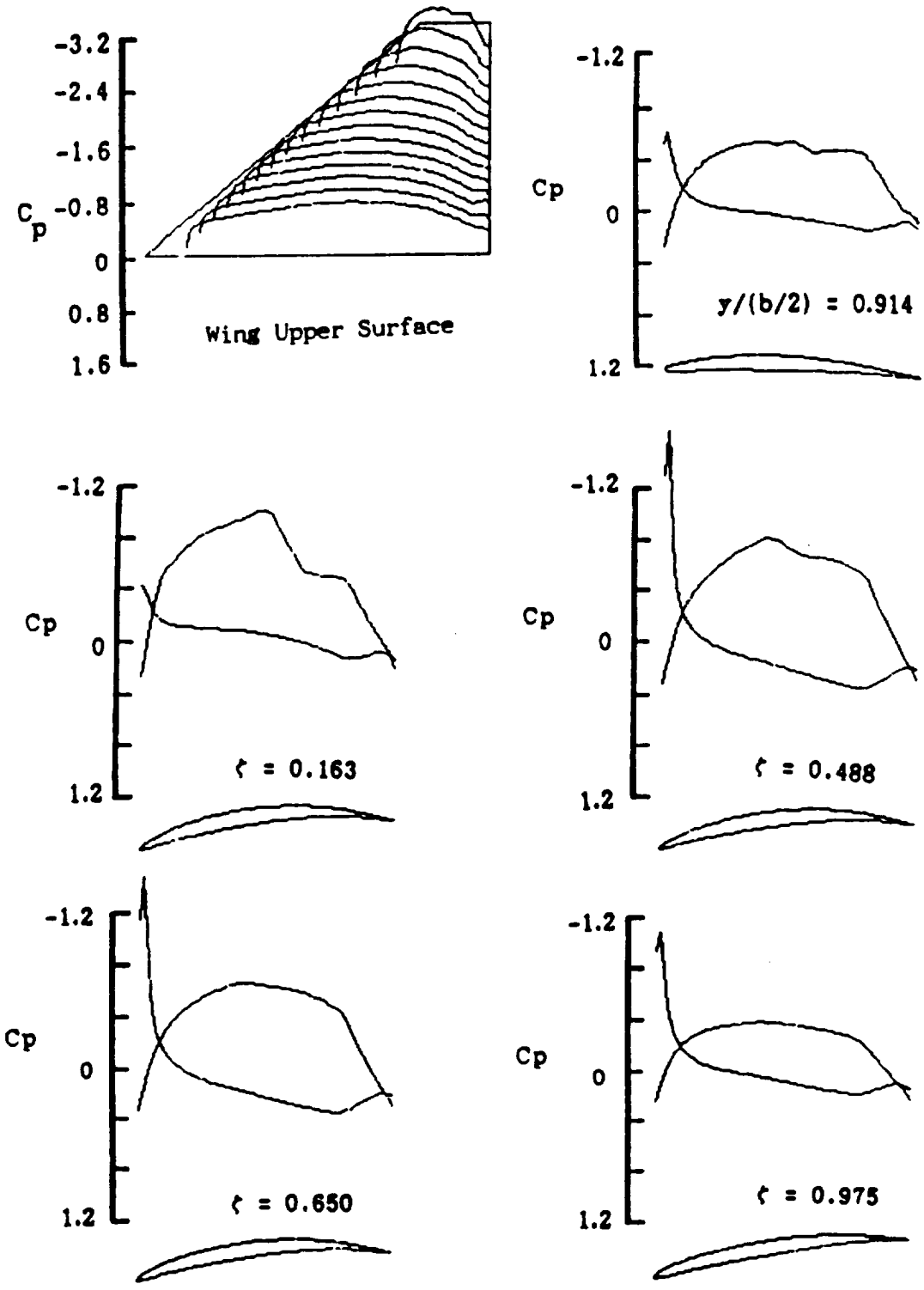

Fig. 32 Calculated wing-winglet C_p distributions for configuration modified cropped delta G at M = 0.8, α = -2°.

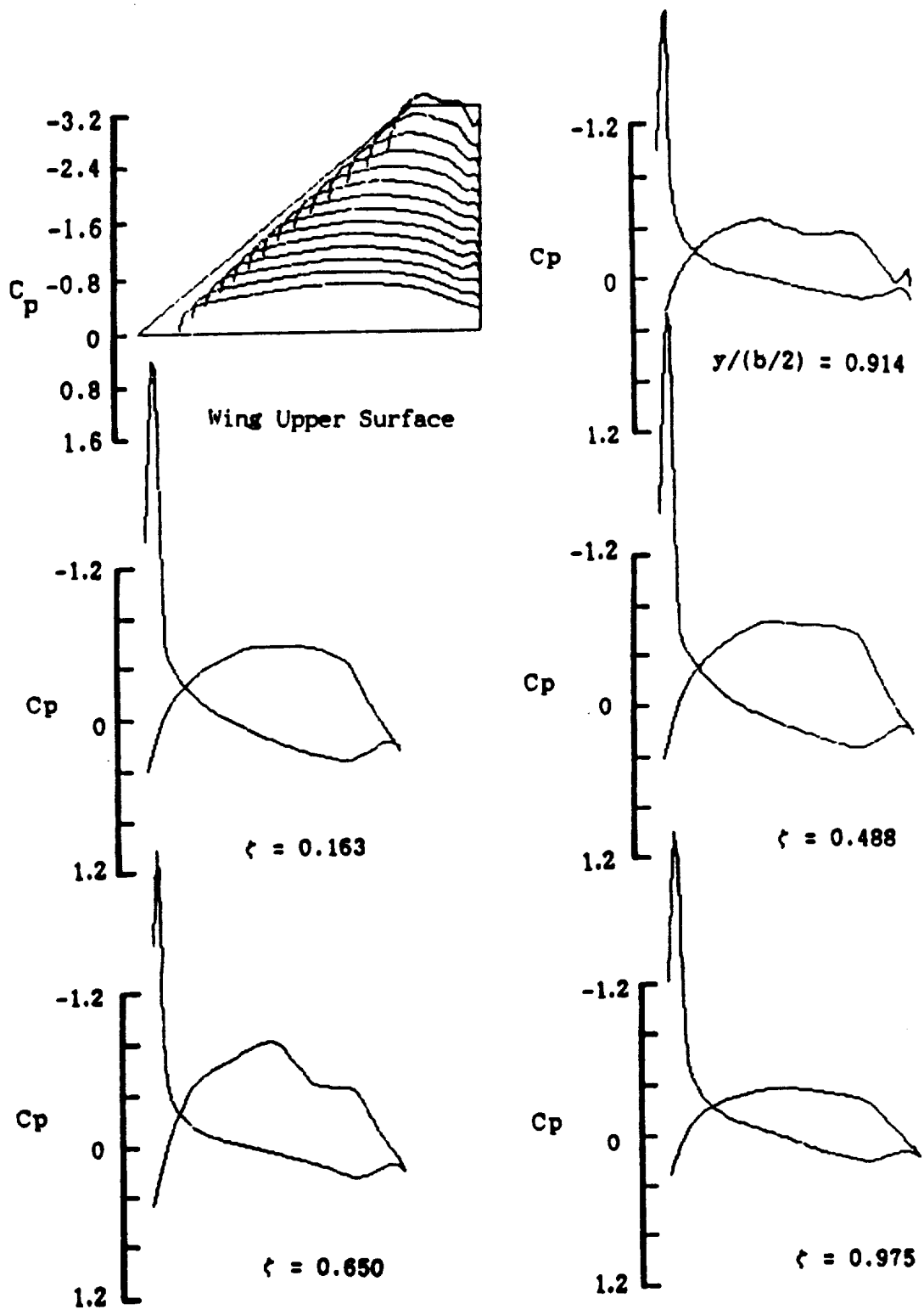

Fig. 33 Calculated wing-winglet C_p distributions for configuration modified cropped delta G at M = 0.8, $\alpha = -4°$.

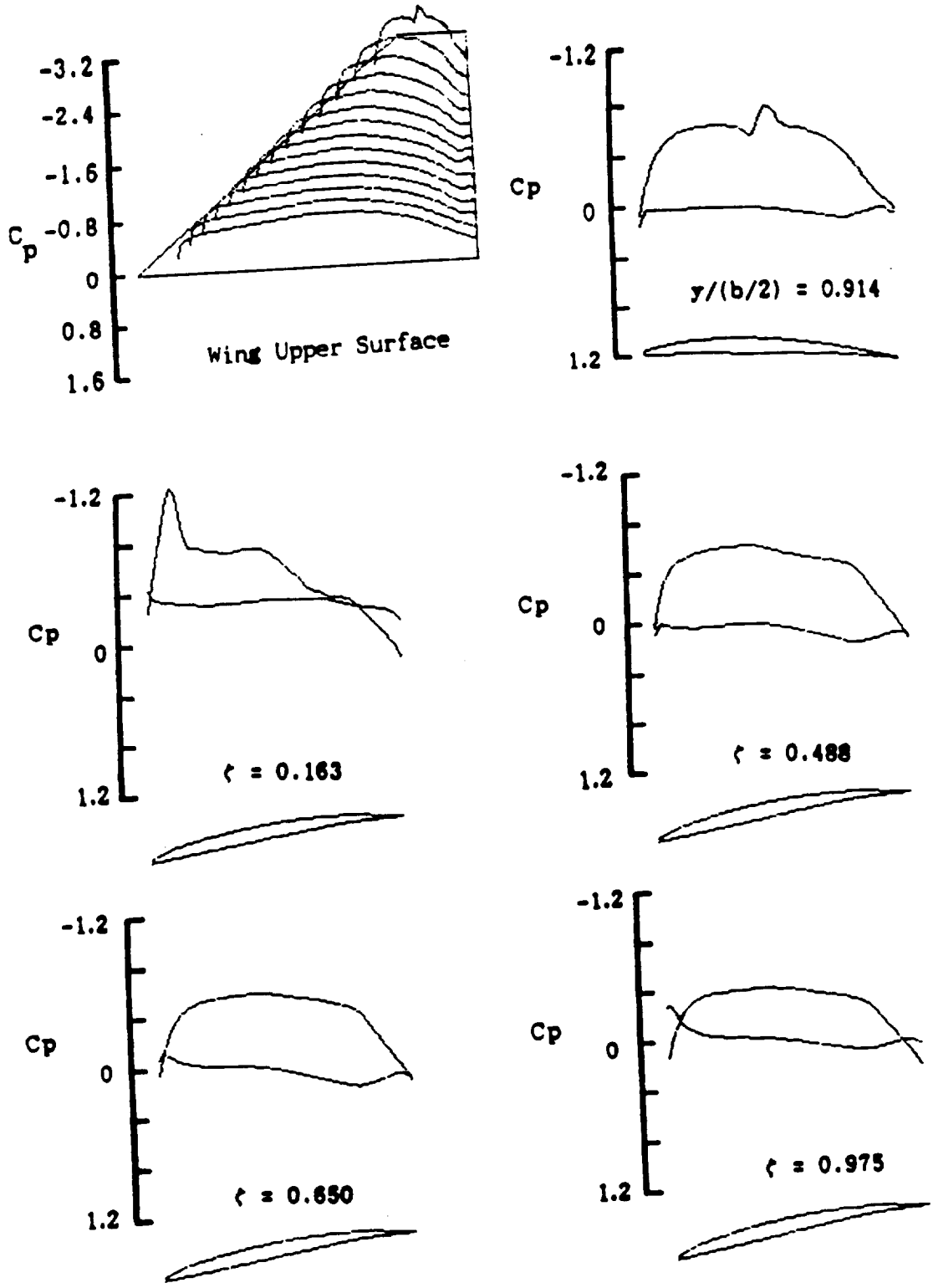

Fig. 34 Calculated C_p distributions for same winglet airfoil cropped delta G configuration at M = 0.8, α = 0°.

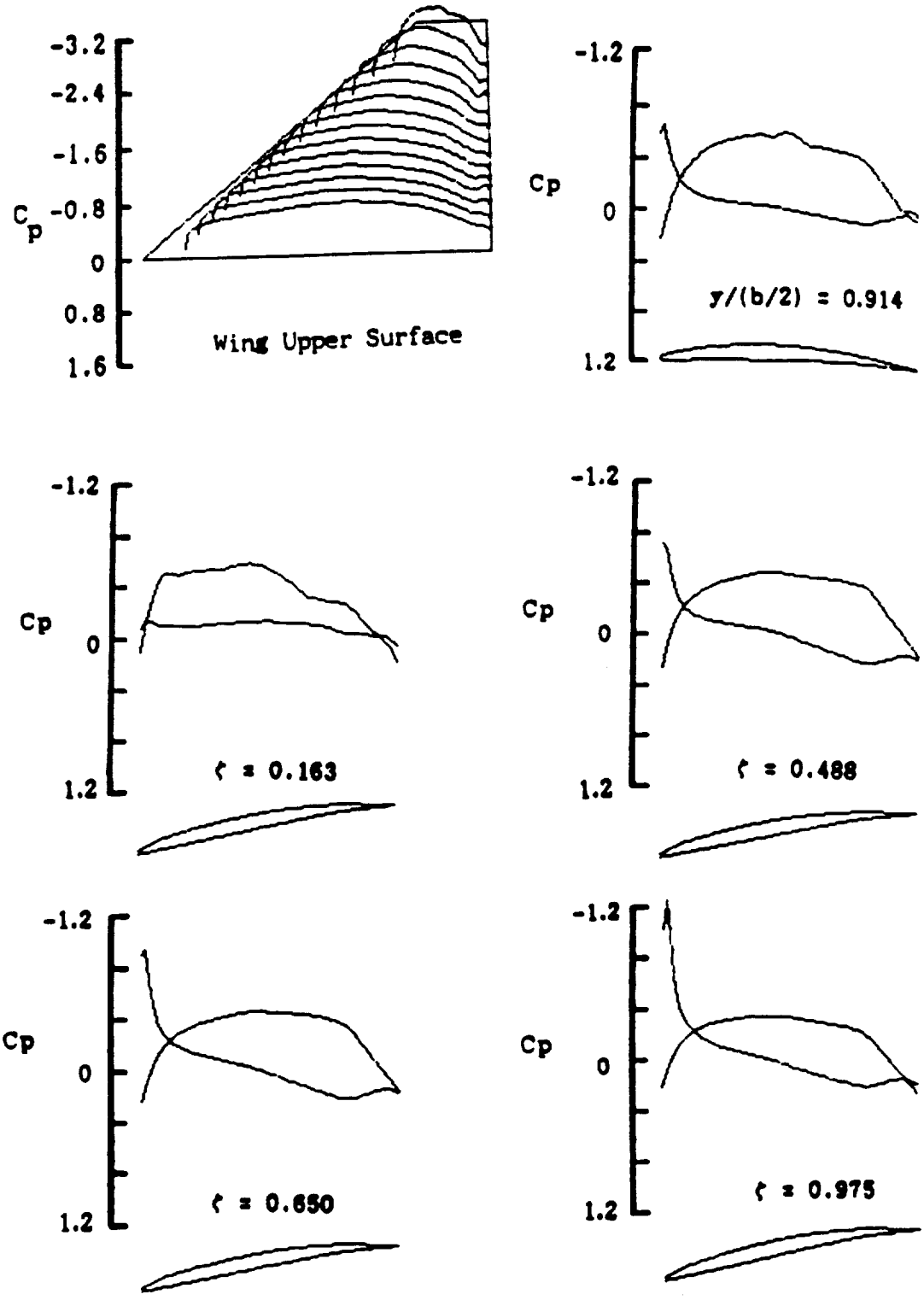

Fig. 35 Calculated C_p distributions for same winglet airfoil cropped delta G configuration at M = 0.8, α = -2°.

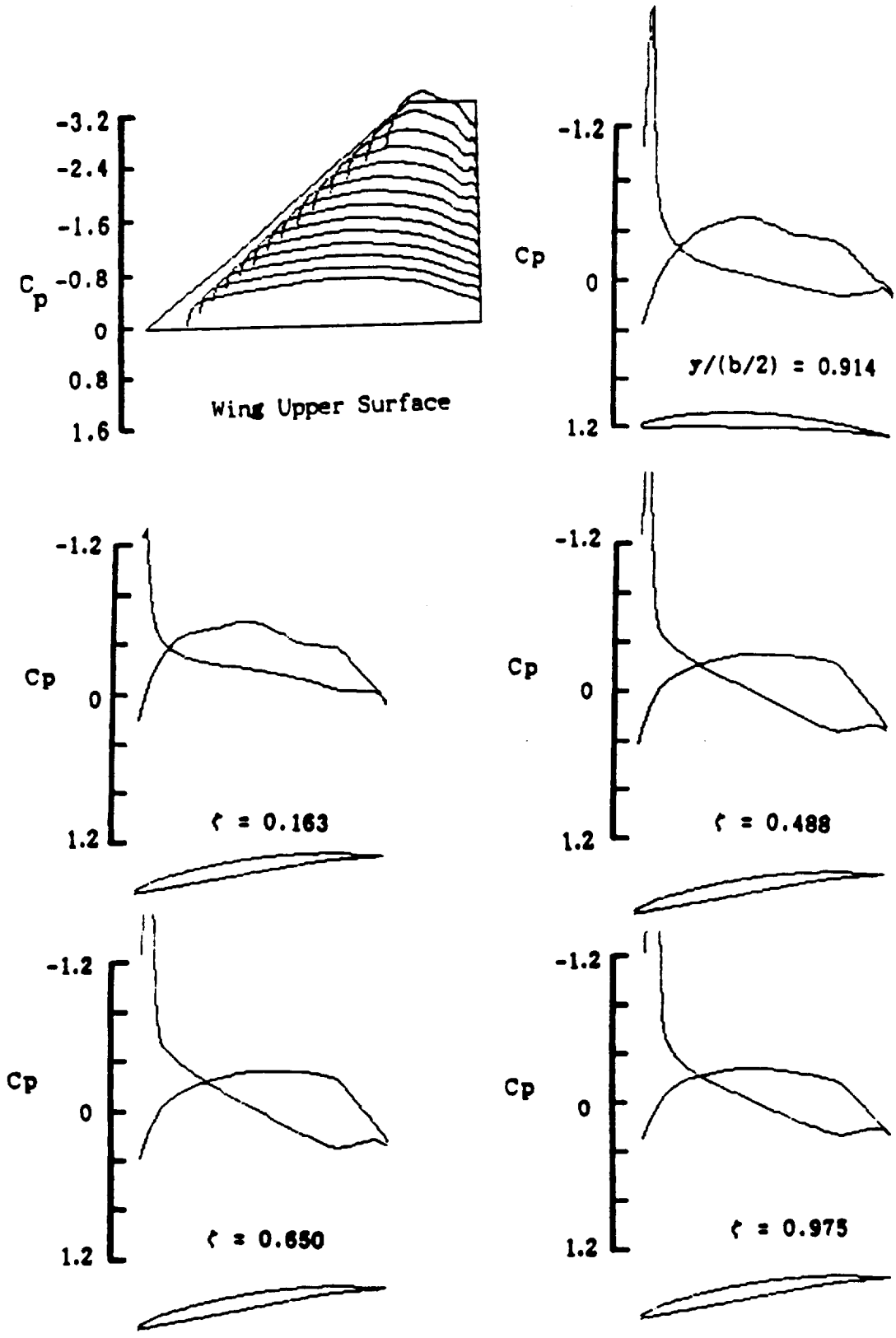

Fig. 36 Calculated C_p distributions for same winglet airfoil cropped delta G configuration at M = 0.8, α = -4°.

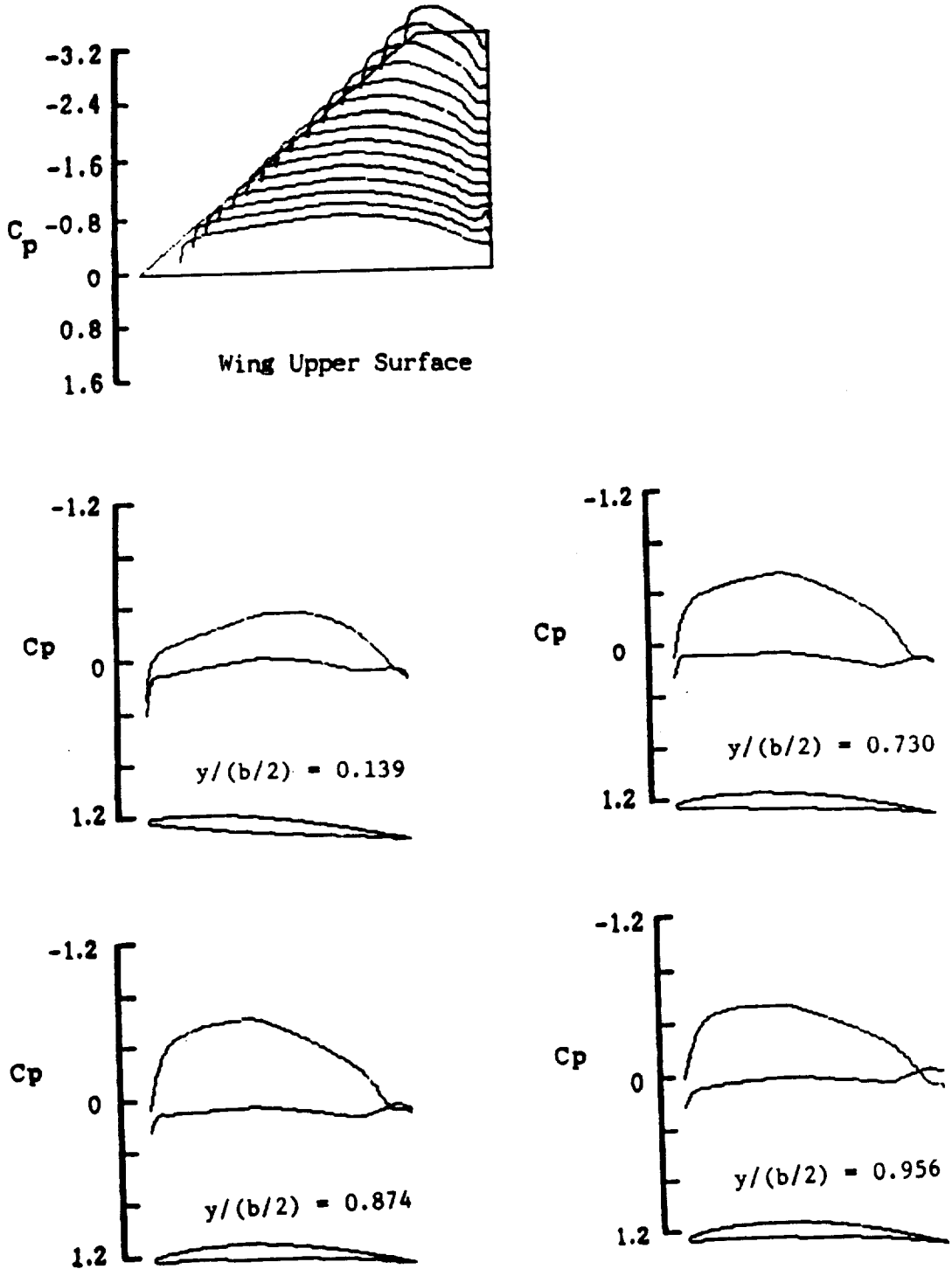

Fig. 37 Calculated wing-alone C_p distributions for wing of cropped delta G wing-winglet at M = 0.8, α = 0°.

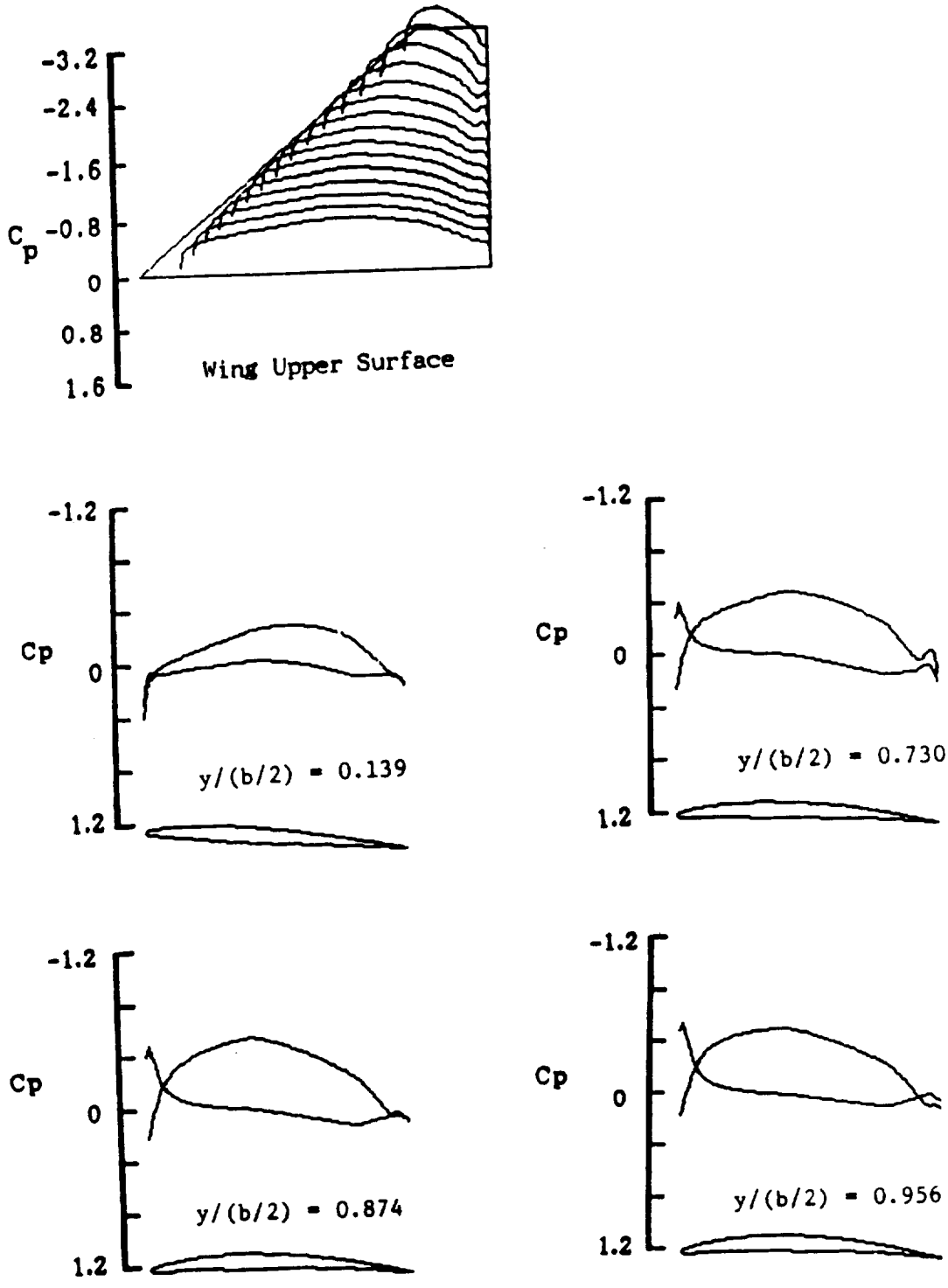

Fig. 38 Calculated wing-alone C_p distributions for wing of cropped delta G wing-winglet at M = 0.8, α = -2°.

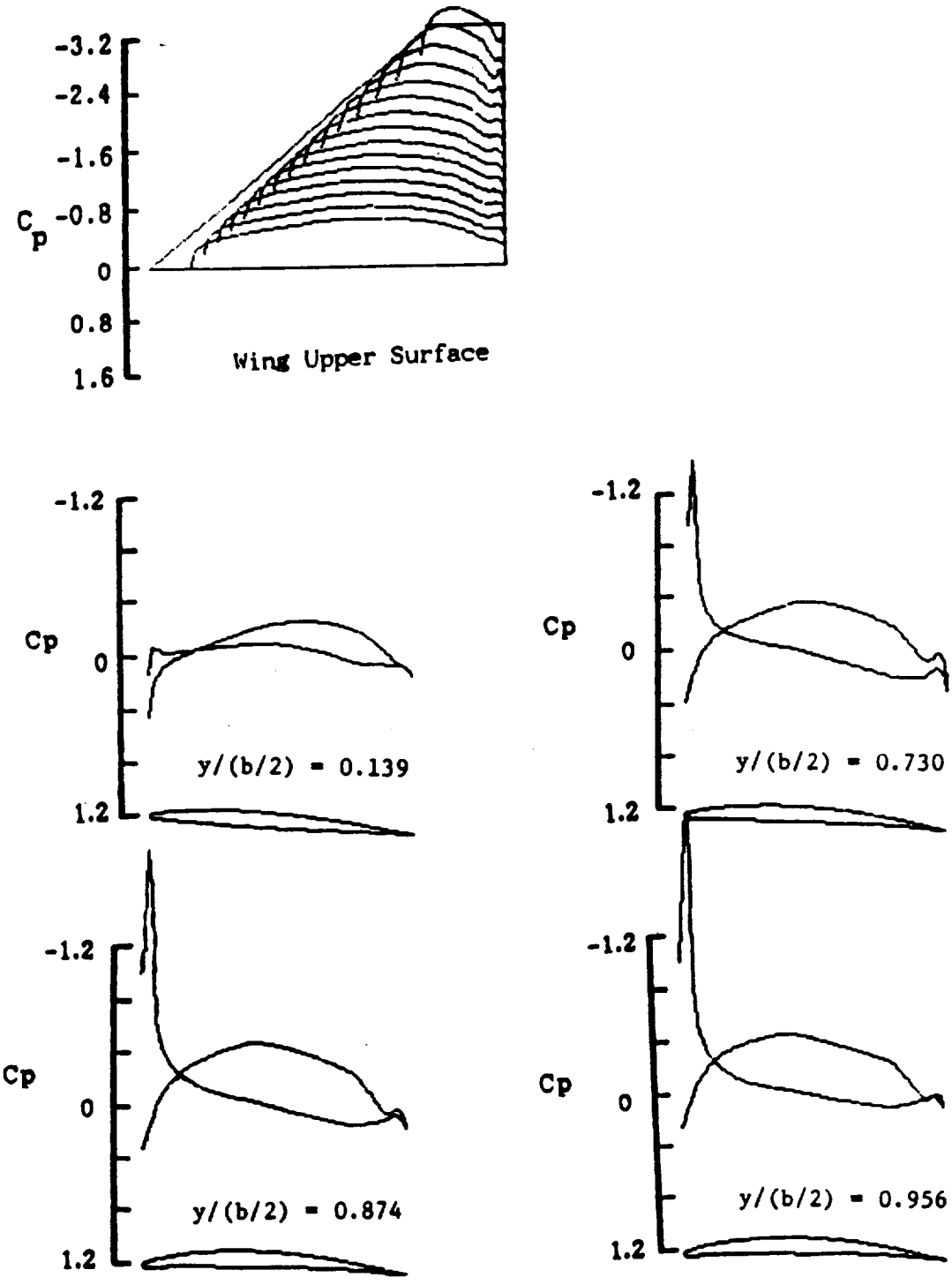

Fig. 39 Calculated wing-alone C_p distributions for wing of cropped delta G wing-winglet at M = 0.8, α = -4°.

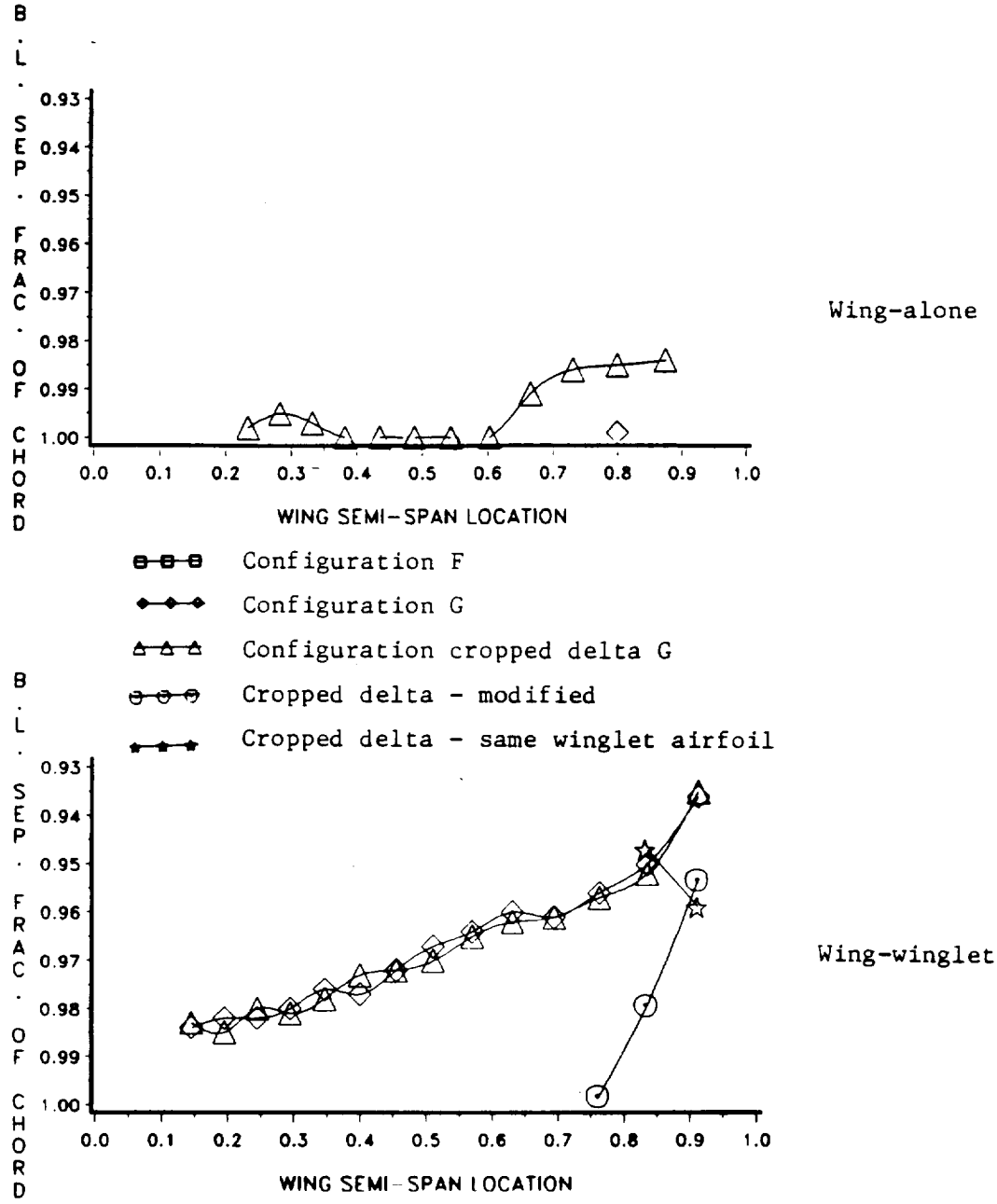

Fig. 40 Predicted upper surface boundary layer separation locations for all wing-alone and wing-winglet configurations at M = 0.8, α = 0° (modified cropped delta G results at α = -0.5°).

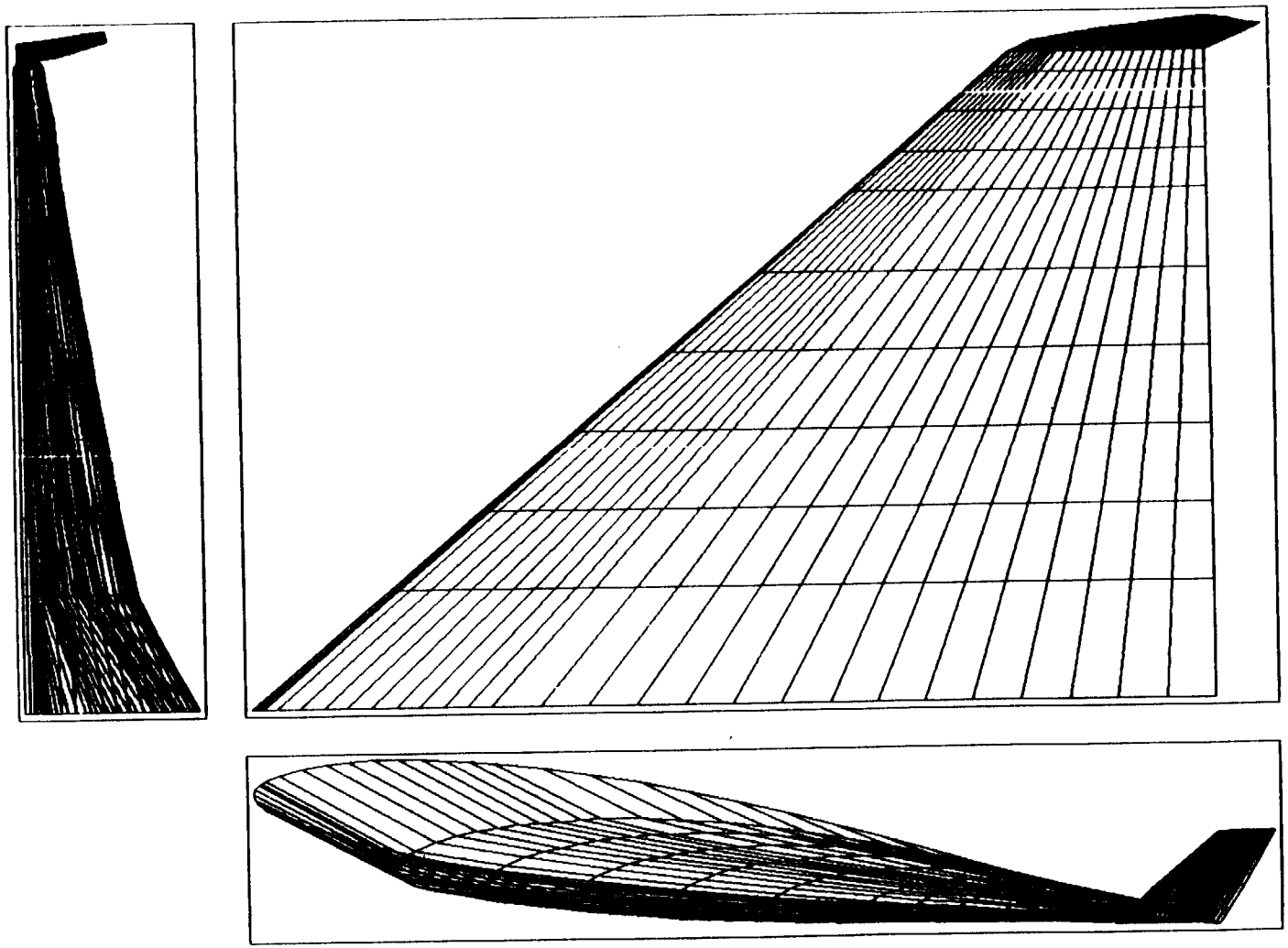

Fig. 41 Wing-winglet geometry for low-speed configuration cropped delta G (A = 2.22, Λ = 50°, λ = 0.203).

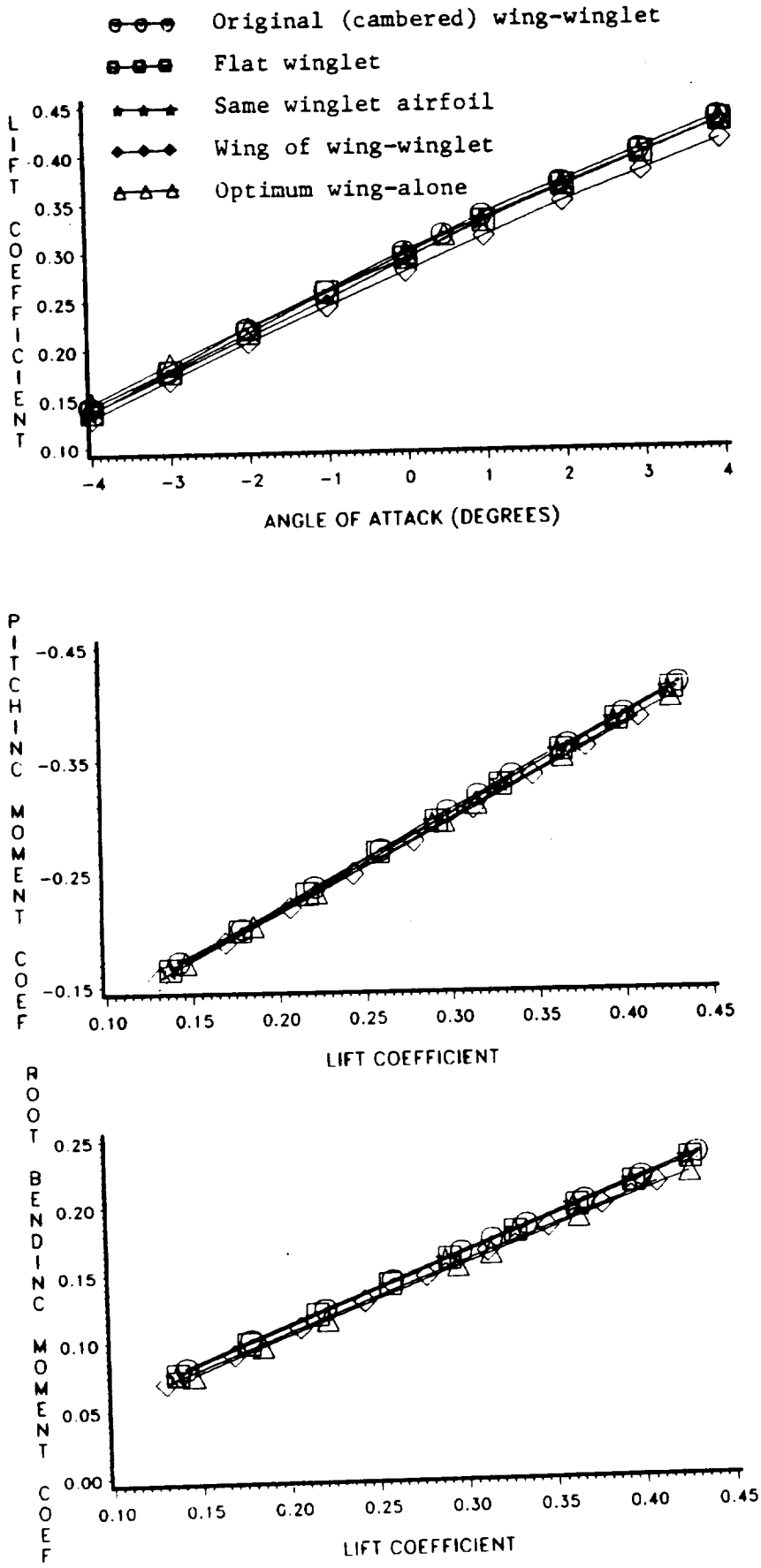

Fig. 42 Predicted performance of wing-alone and wing-winglet configurations low-speed cropped delta G at M = 0.1; C_L-α, C_m-C_L, C_B-C_L.

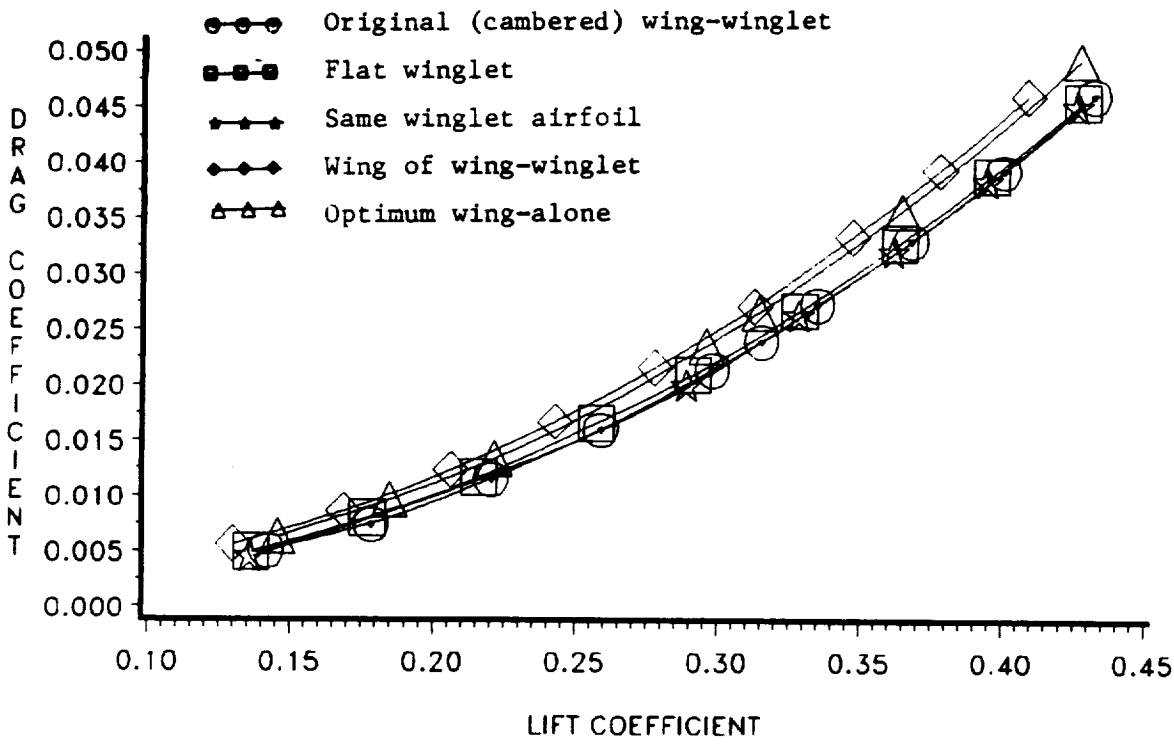

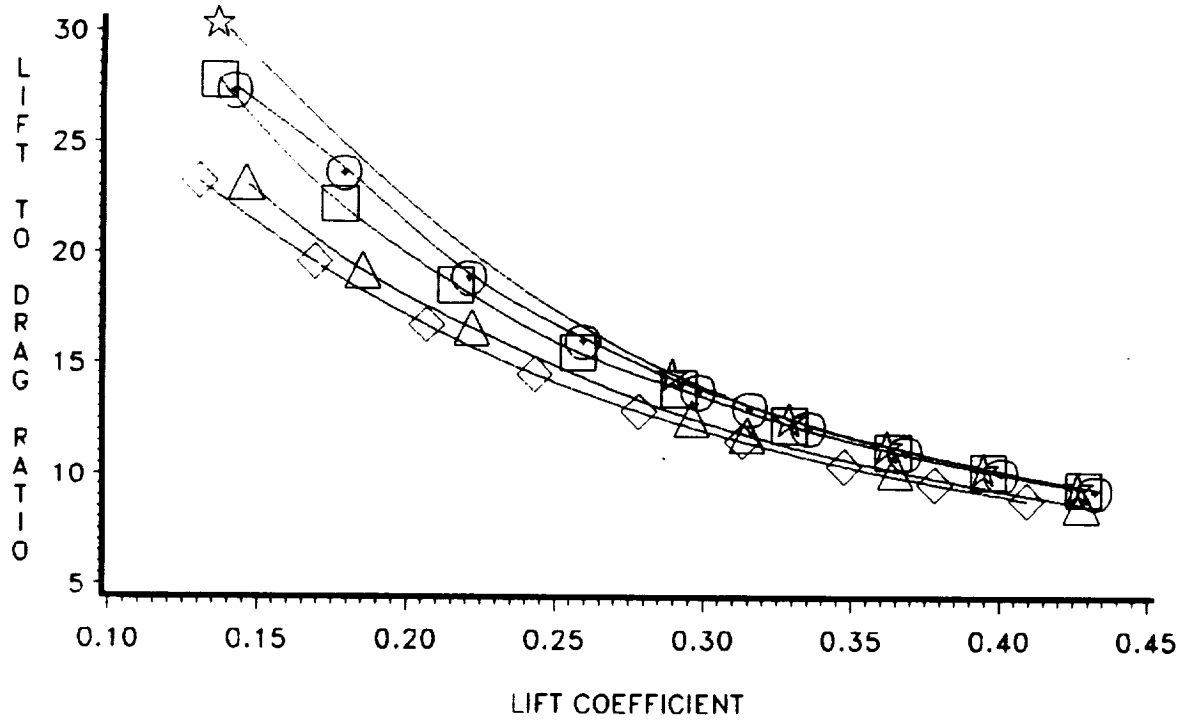

Fig. 42 (Concluded) - Predicted performance of wing-alone and wing-winglet configurations low-speed cropped delta G at M = 0.1; drag polar and L/D-C_L.

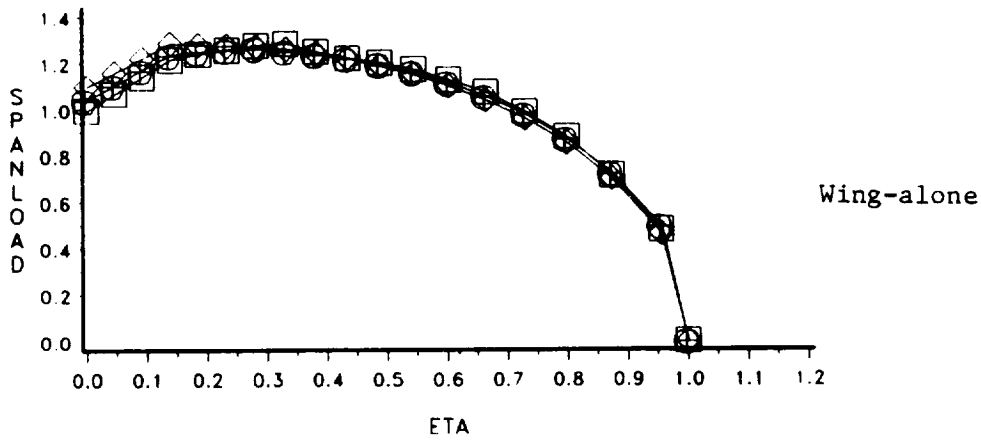

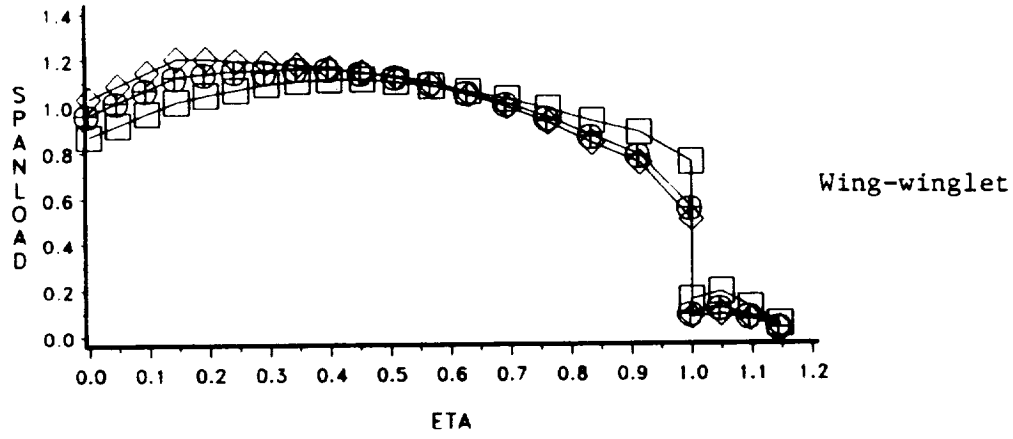

Fig. 43 Calculated normalized spanloads for wing-alone and wing-winglet configurations low-speed cropped delta G, optimum wing and original wing-winglet at M = 0.1.

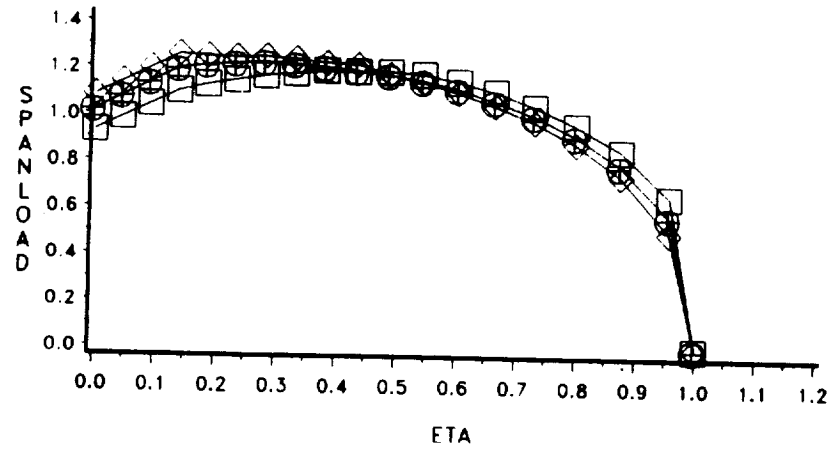

Wing-alone

DIAMOND: A=4 SQUARE: A=-4
CIRCLE: A=0

Angle of attack (deg)

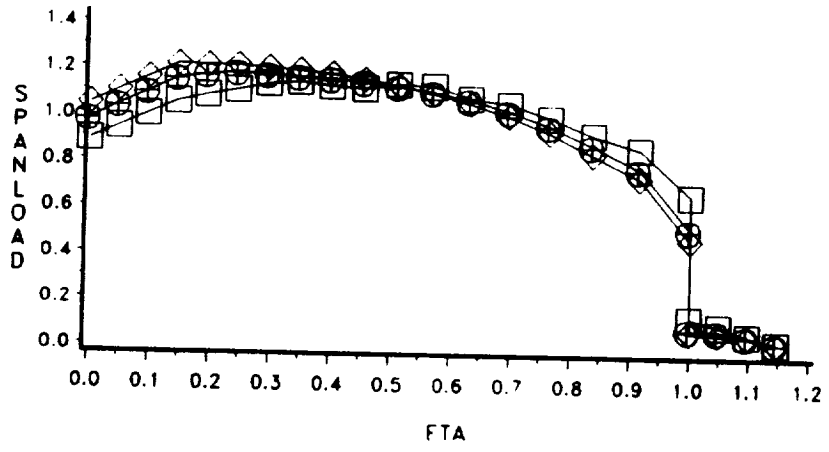

Wing-winglet

Fig. 43 Calculated normalized spanloads for wing and wing-winglet configurations low-speed cropped delta G, wing of wing-winglet and same winglet airfoil at M = 0.1.

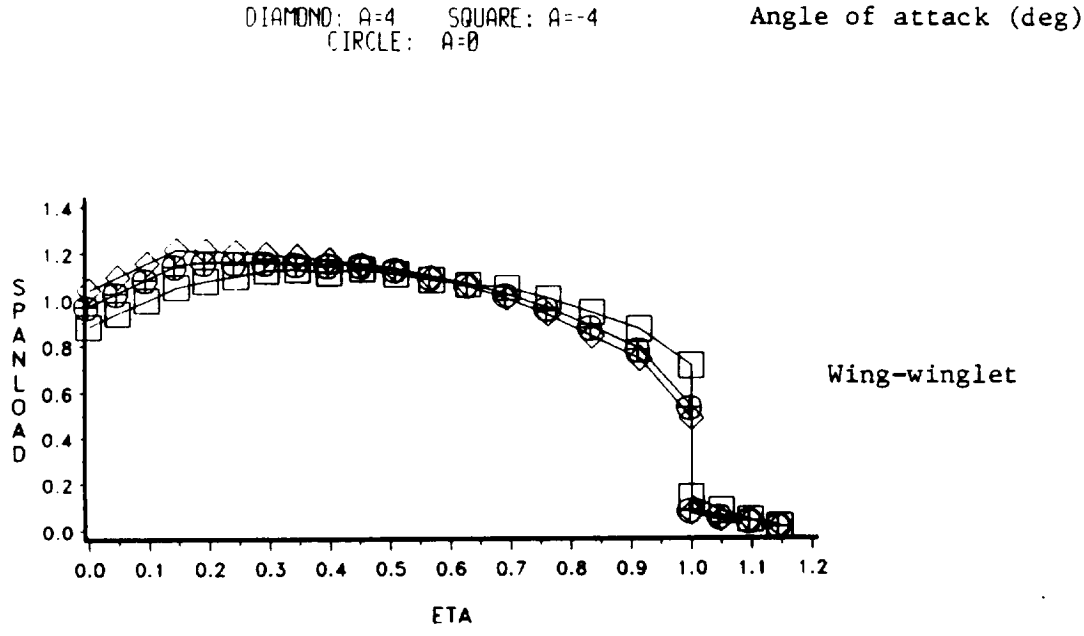

Fig. 43 (Concluded) Calculated normalized spanloads for low-speed uncambered winglet cropped delta G configuration at M = 0.1.

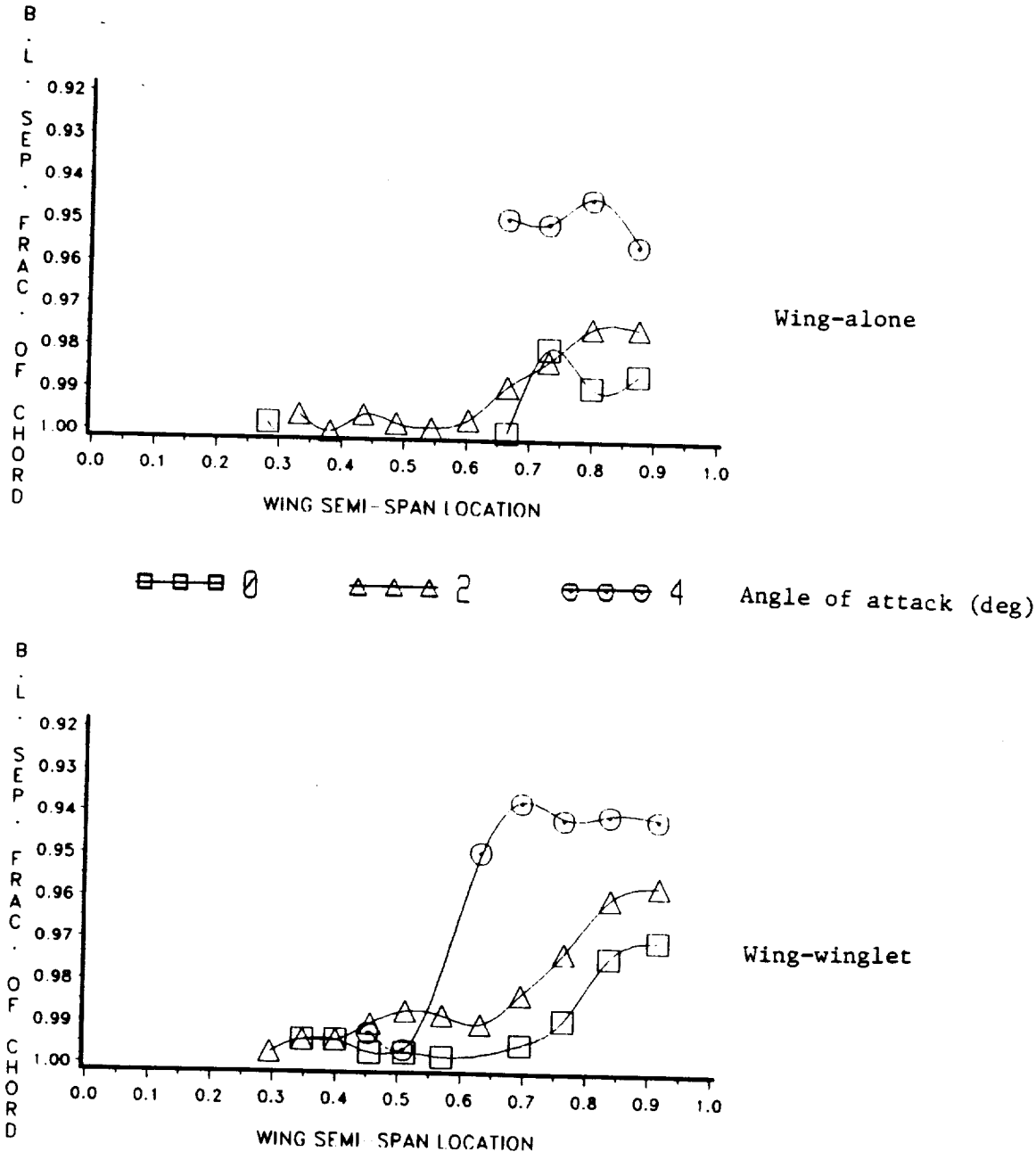

Fig. 44 Predicted upper surface boundary layer separation locations for optimum wing-alone and original wing-winglet low-speed cropped delta G configurations at M = 0.1.

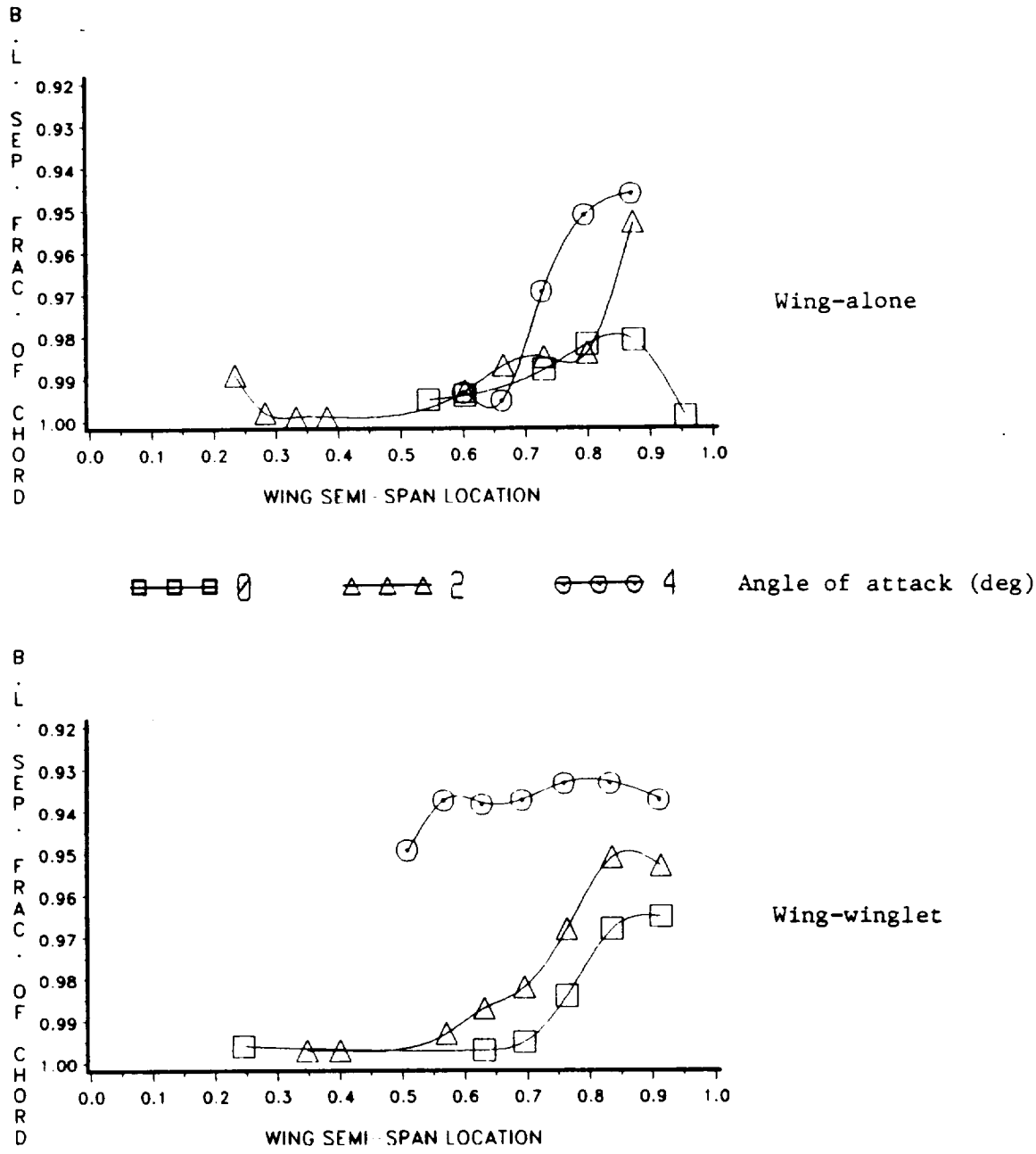

Fig. 44 Predicted upper surface boundary layer separation locations for wing of wing-winglet and same winglet airfoil low-speed cropped delta G configurations at M = 0.1.

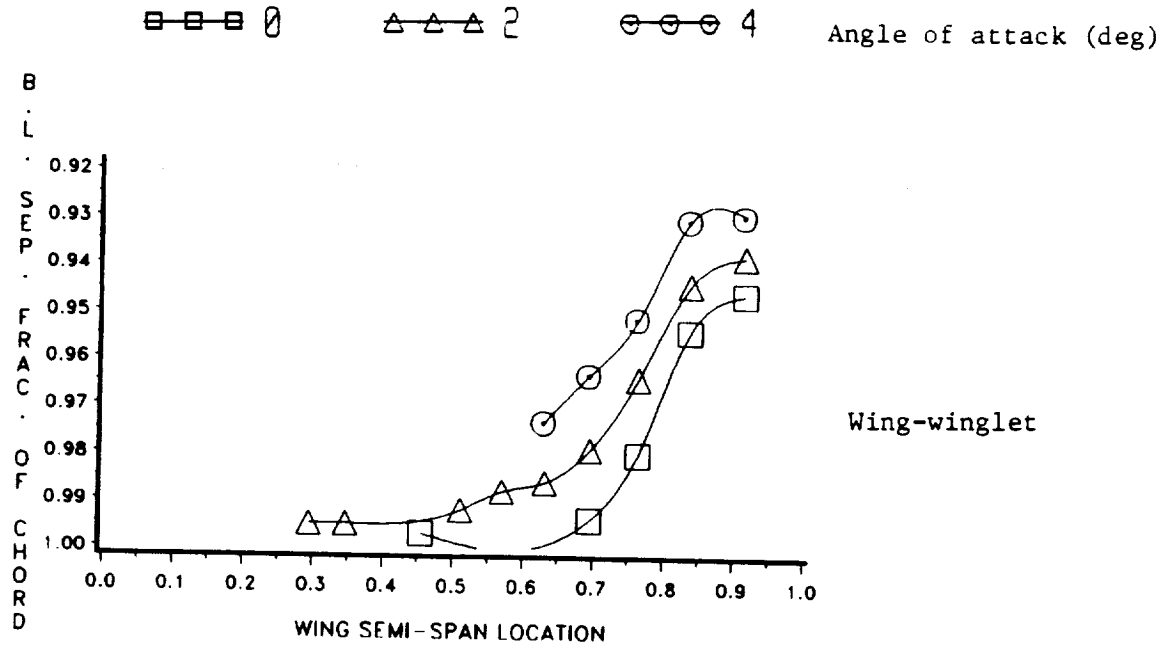

Fig. 44 (Concluded) Predicted upper surface boundary layer separation locations for uncambered winglet cropped delta G configuration at M = 0.1.

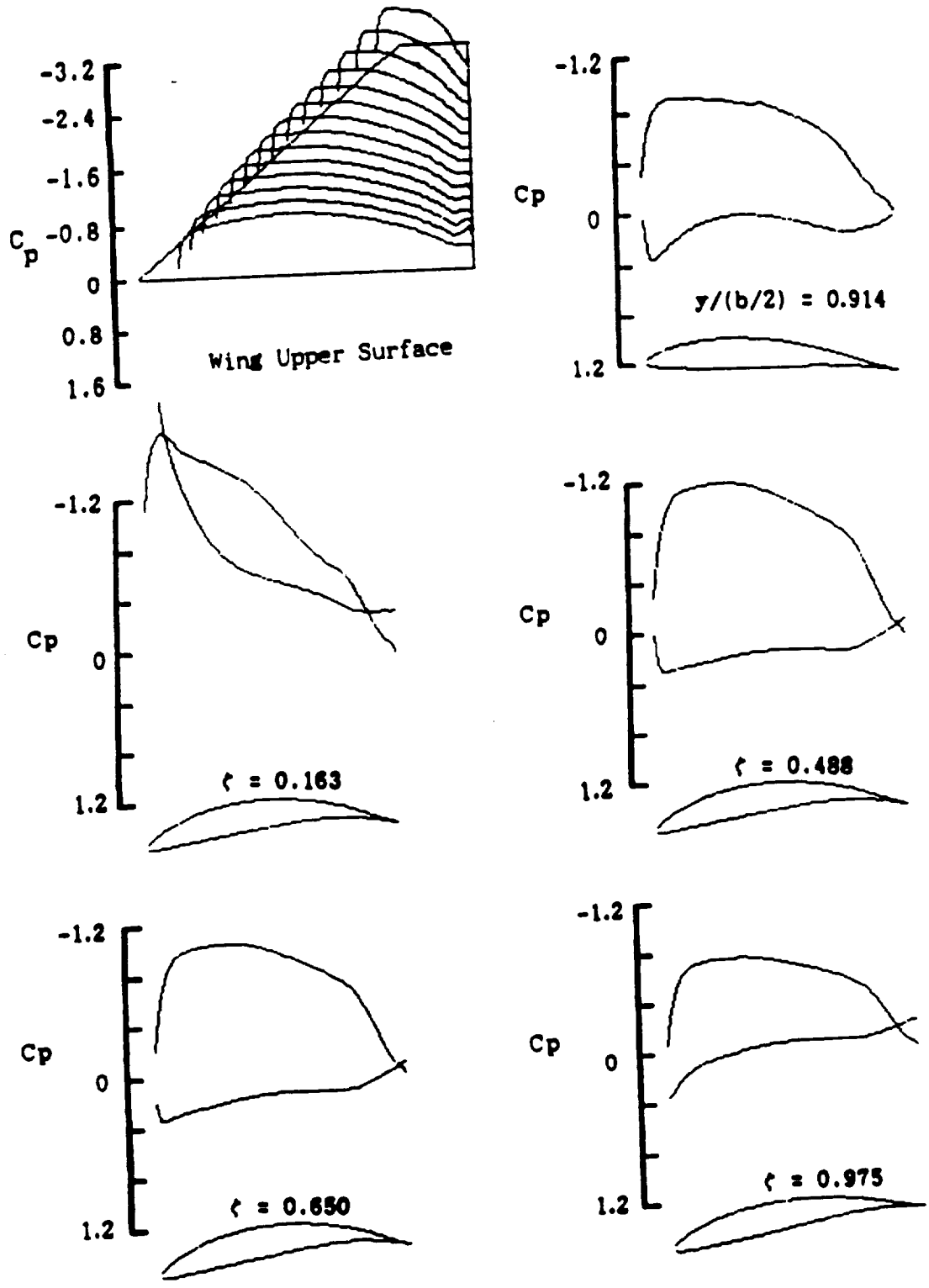

Fig. 45 Calculated C_p distributions for original low-speed cropped delta G wing-winglet configuration at M = 0.1, $\alpha = 4^\circ$.

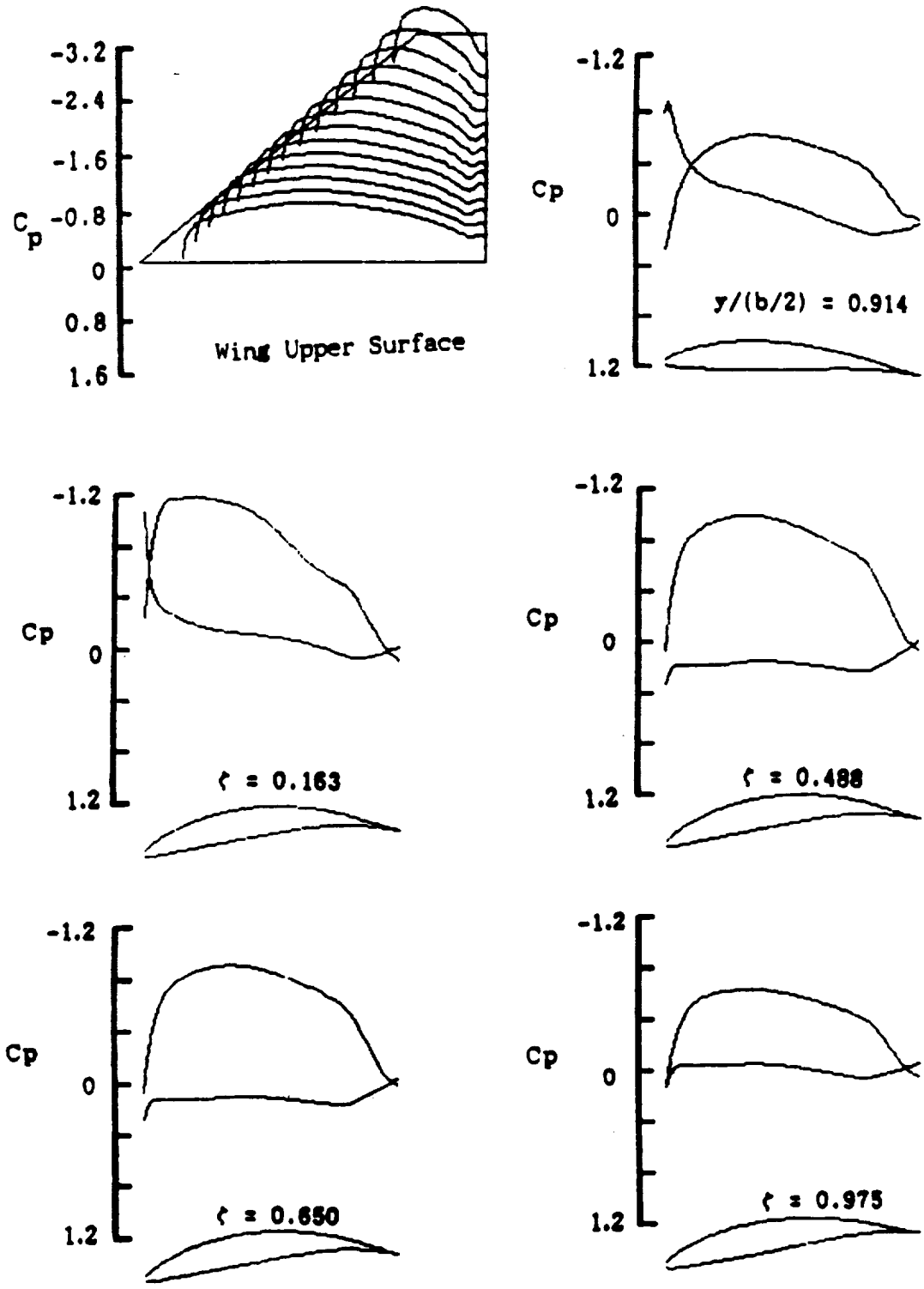

Fig. 46 Calculated C_p distributions for original low-speed cropped delta G wing-winglet configuration at M = 0.1, α = 0°.

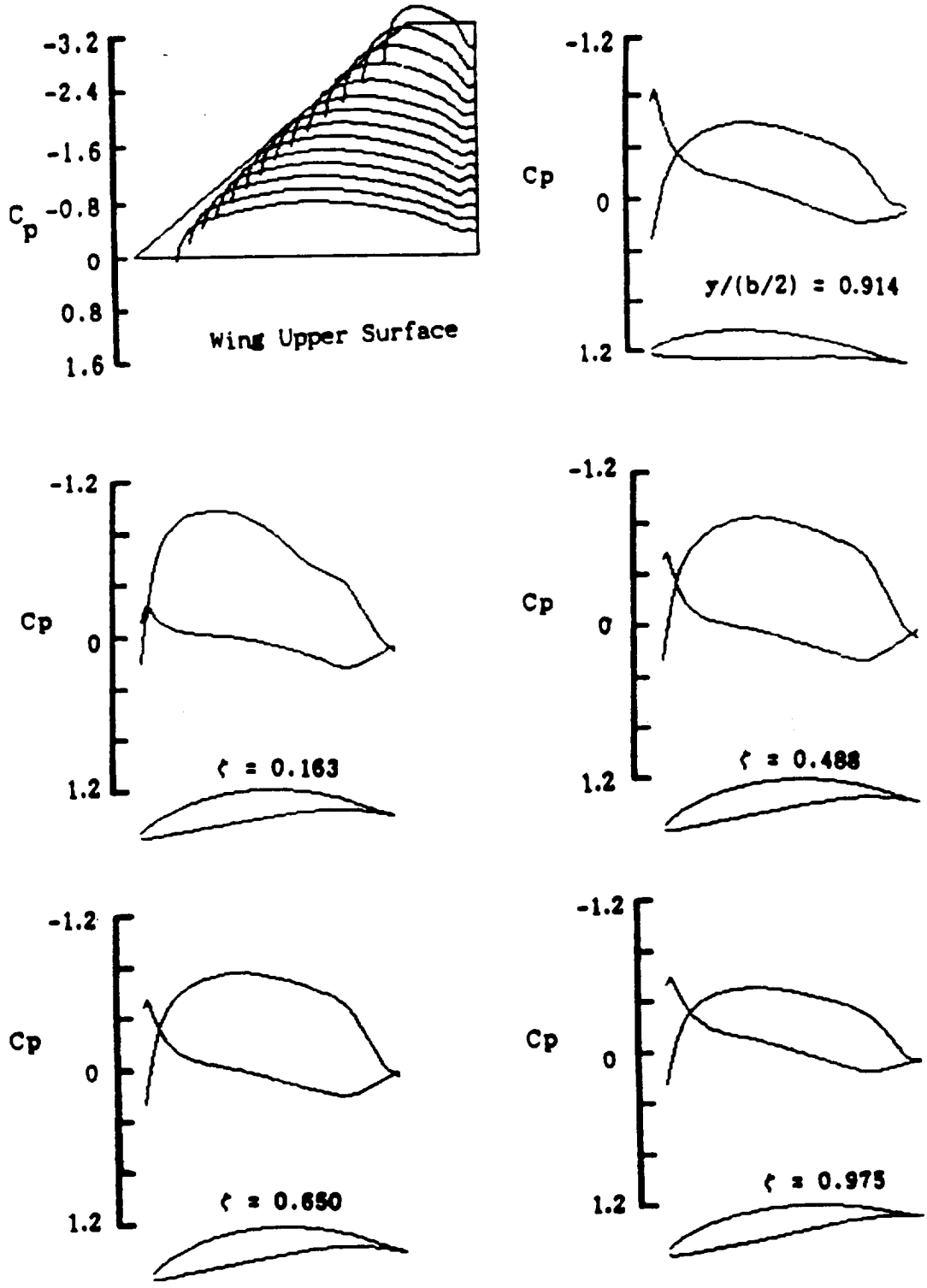

Fig. 47 Calculated C_p distributions for original low-speed cropped delta G wing-winglet configuration at M = 0.1, α = -4°.

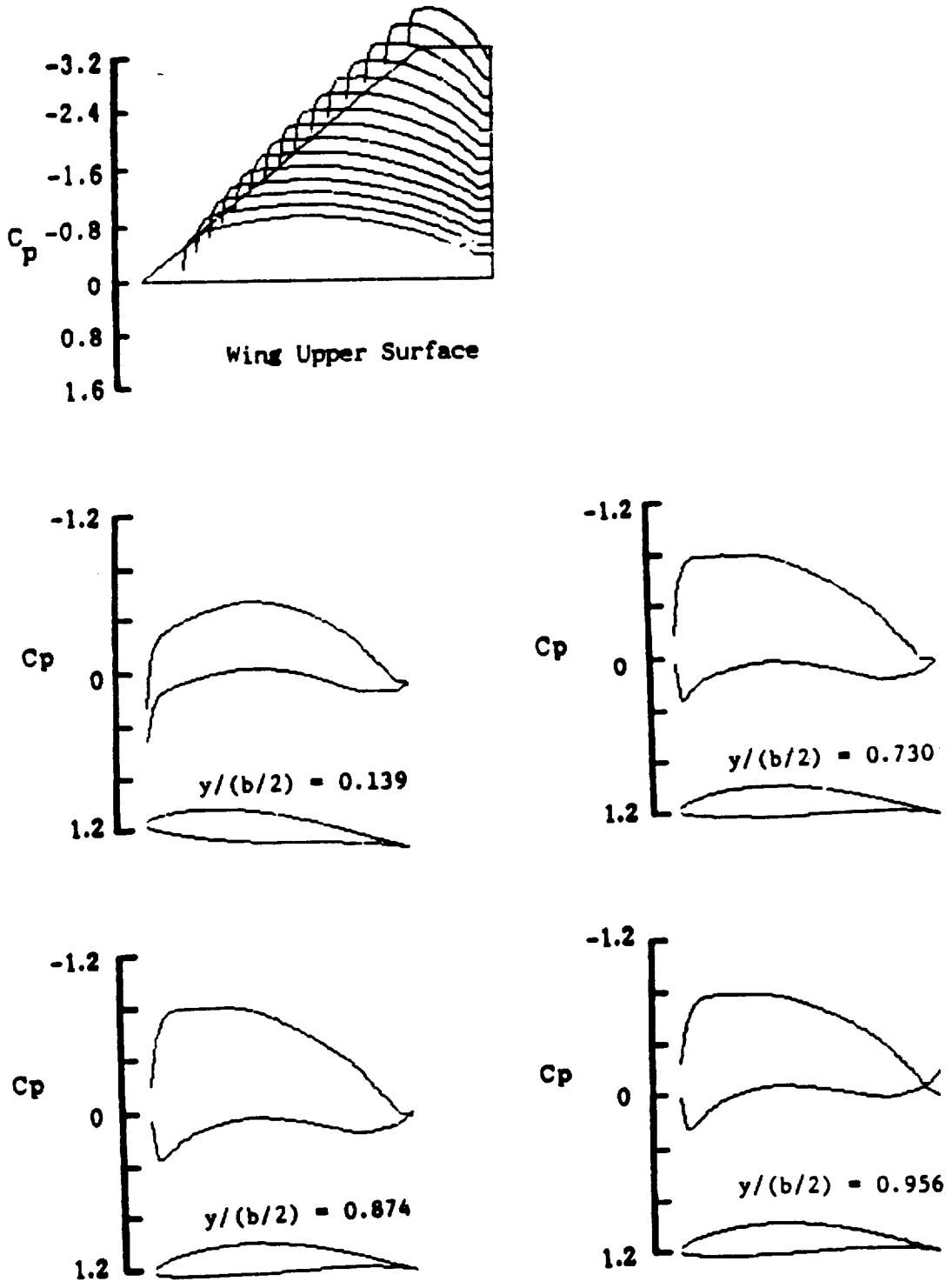

Fig. 48 Calculated C_p distributions for low-speed optimum wing-alone cropped delta G configuration at M = 0.1, α = 4°.

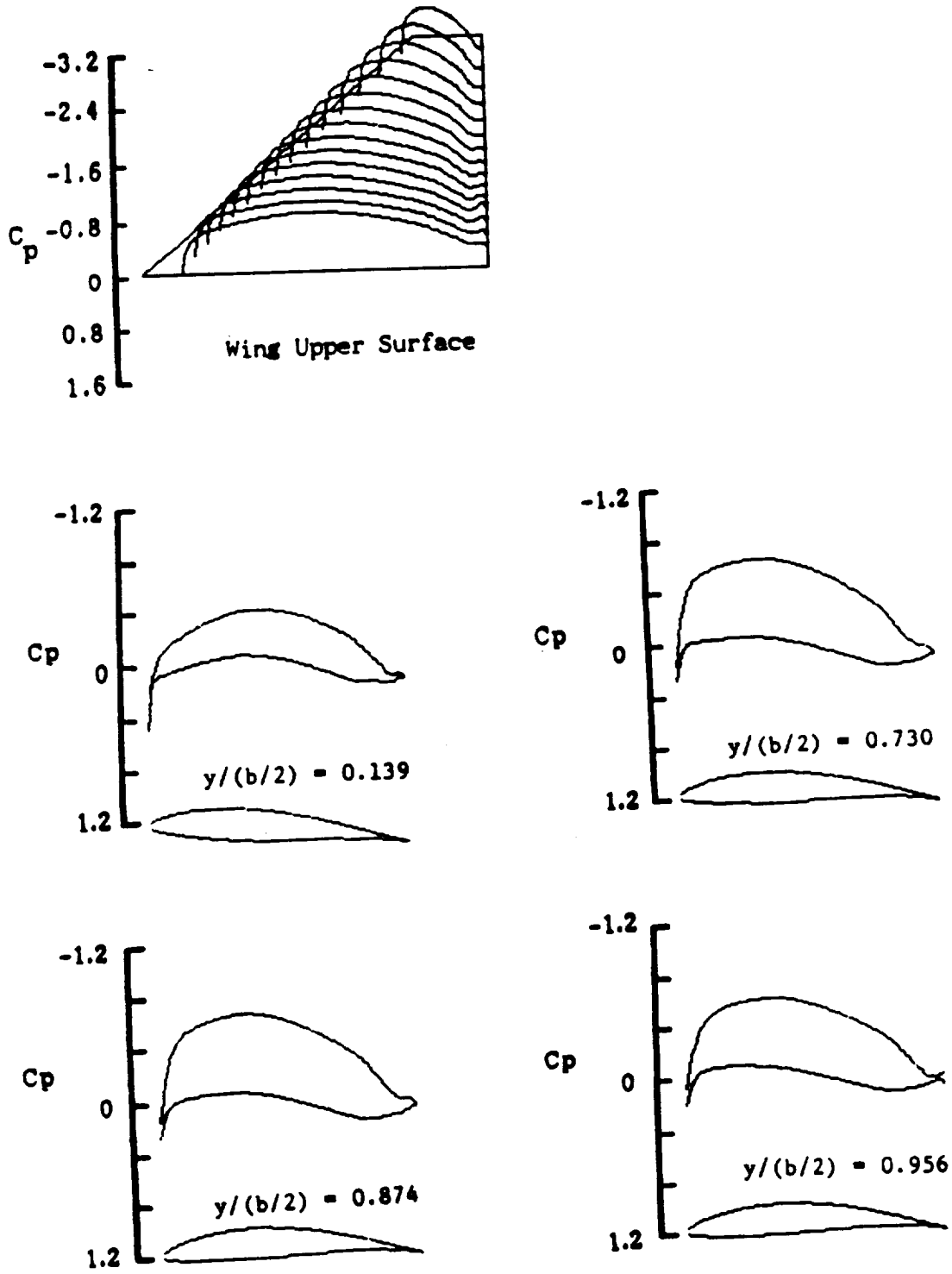

Fig. 49 Calculated C_p distributions for low-speed optimum wing-alone cropped delta G configuration at M = 0.1, α = 0°.

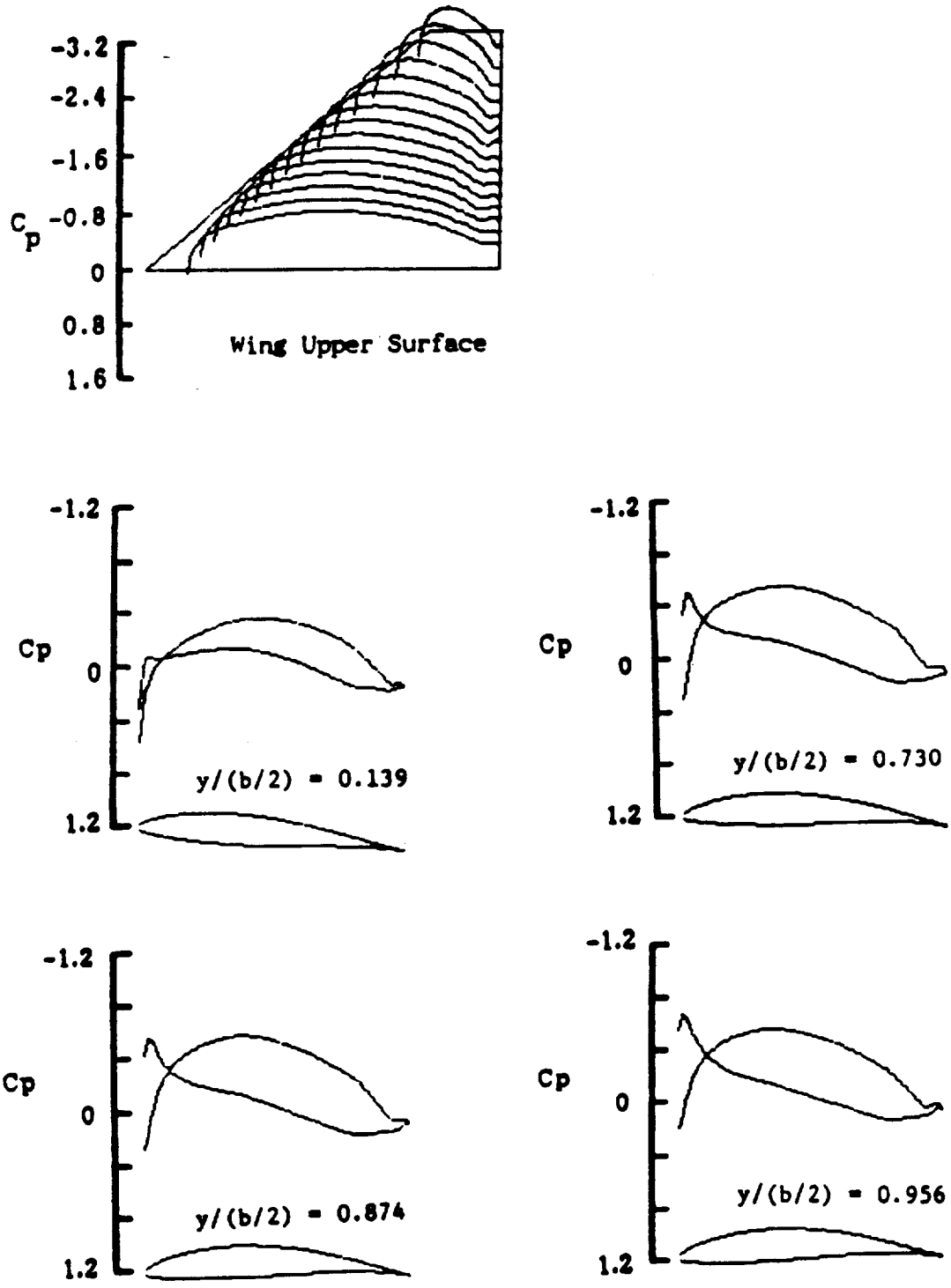

Fig. 50 Calculated C_p distributions for low-speed optimum wing-alone cropped delta G configuration at M = 0.1, α = -3°.

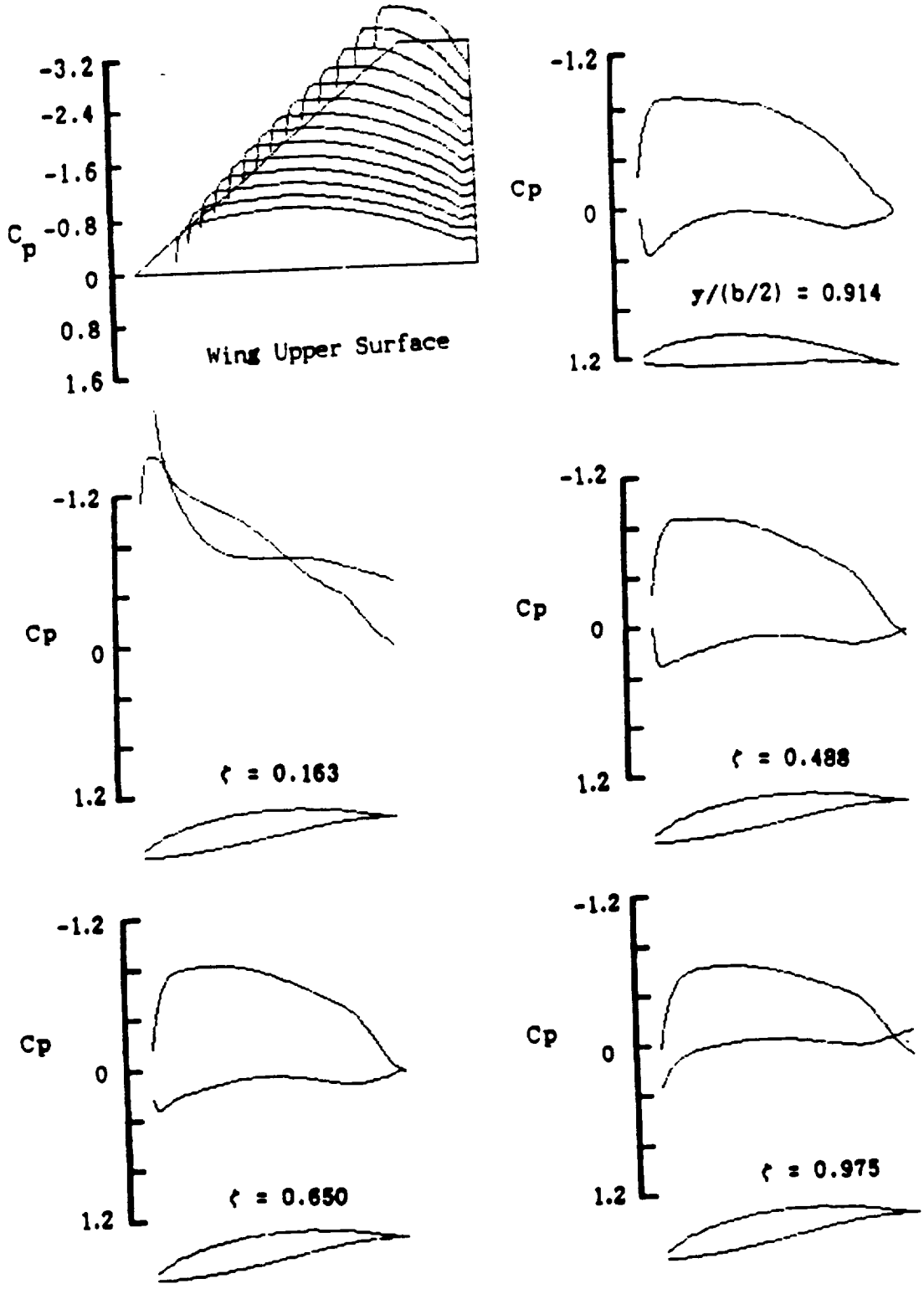

Fig. 51 Calculated C_p distributions for low-speed same winglet airfoil cropped delta G configuration at M = 0.1, α = 4°.

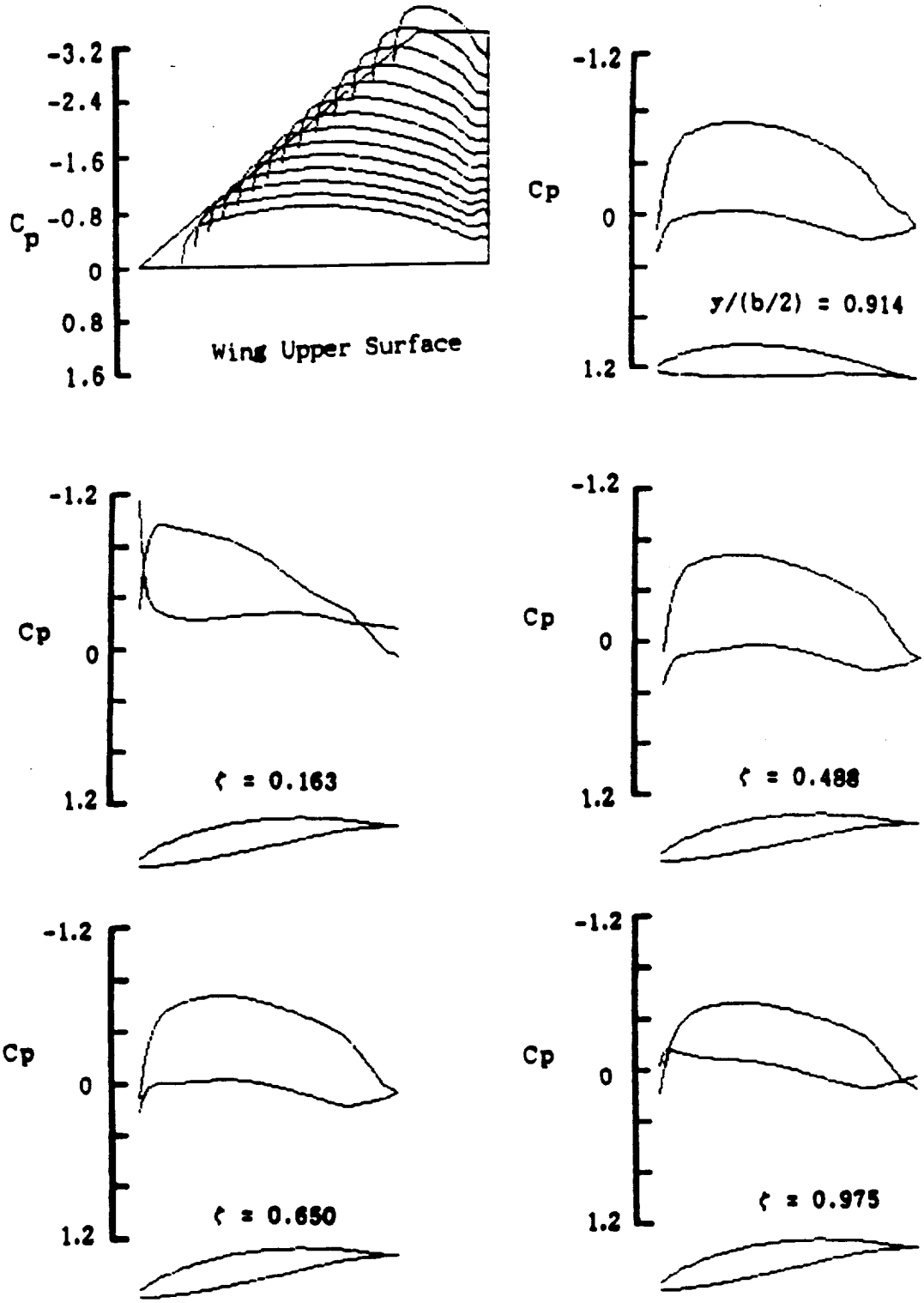

Fig. 52 Calculated C_p distributions for low-speed same winglet airfoil cropped delta G configuration at M = 0.1, α = 0°.

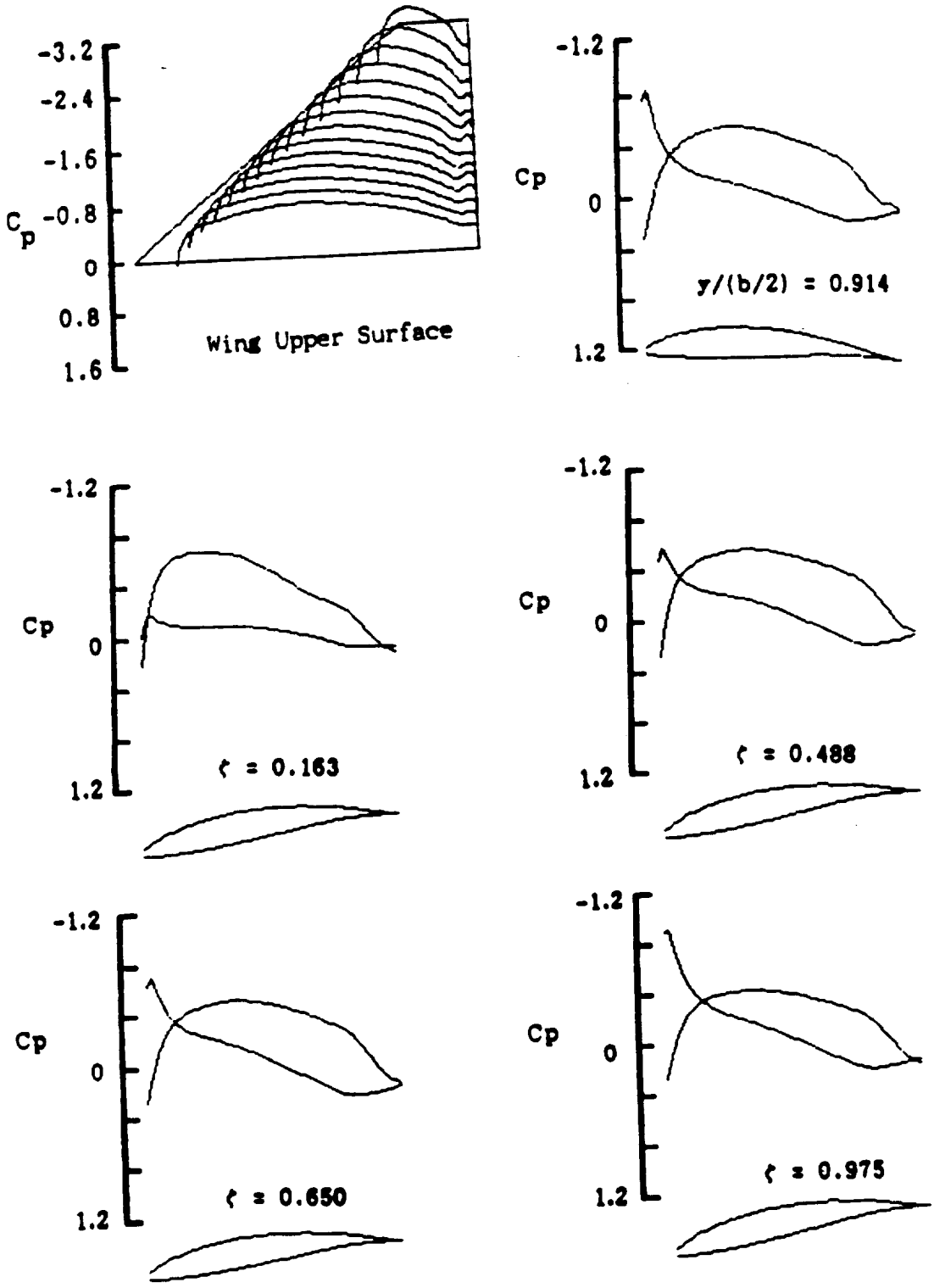

Fig. 53 Calculated C_p distributions for low-speed same winglet airfoil cropped delta G configuration at M = 0.1, α = -4°.

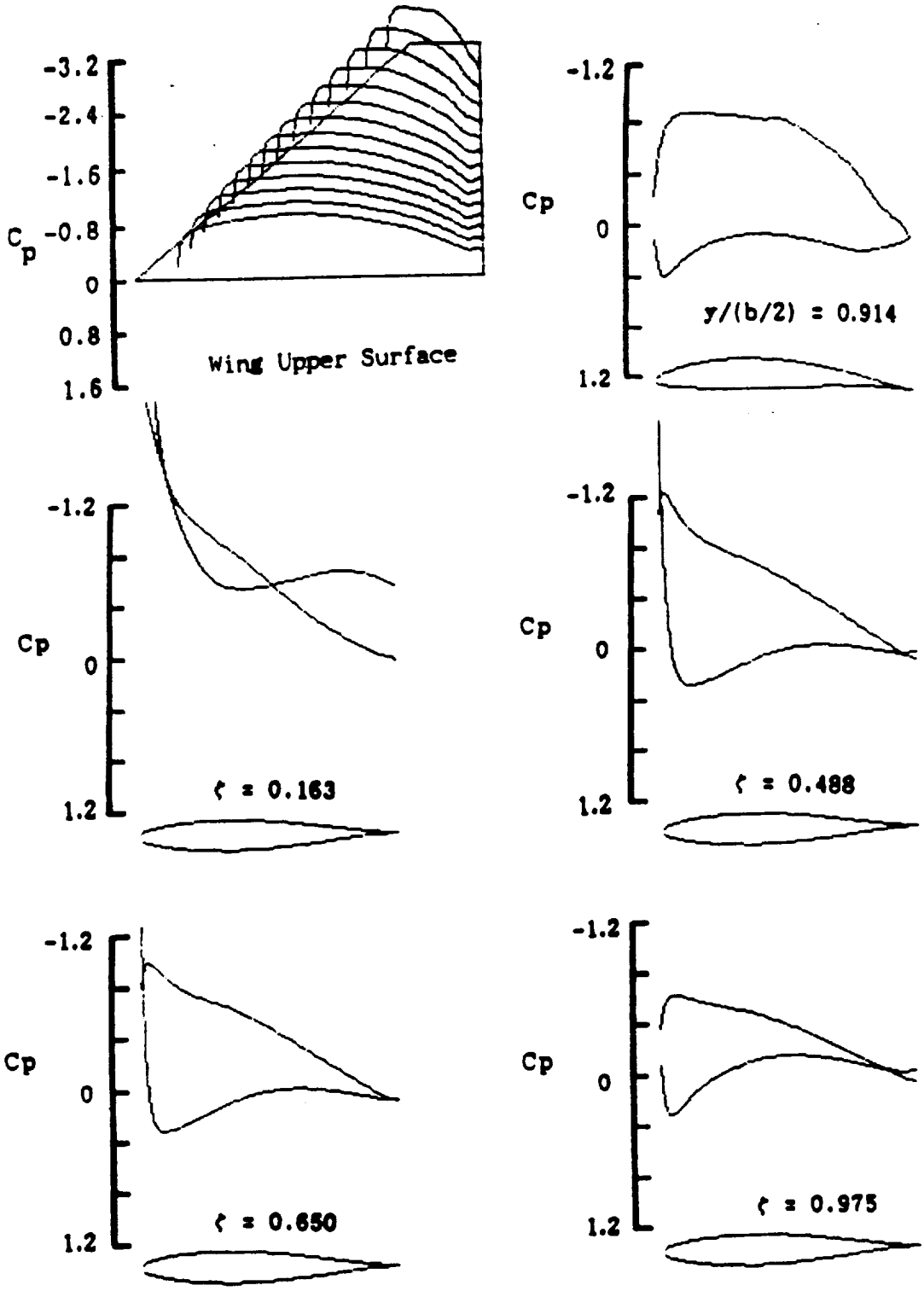

Fig. 54 Calculated C_p distributions for low-speed uncambered winglet airfoil cropped delta G configuration at M = 0.1, α = 4°.

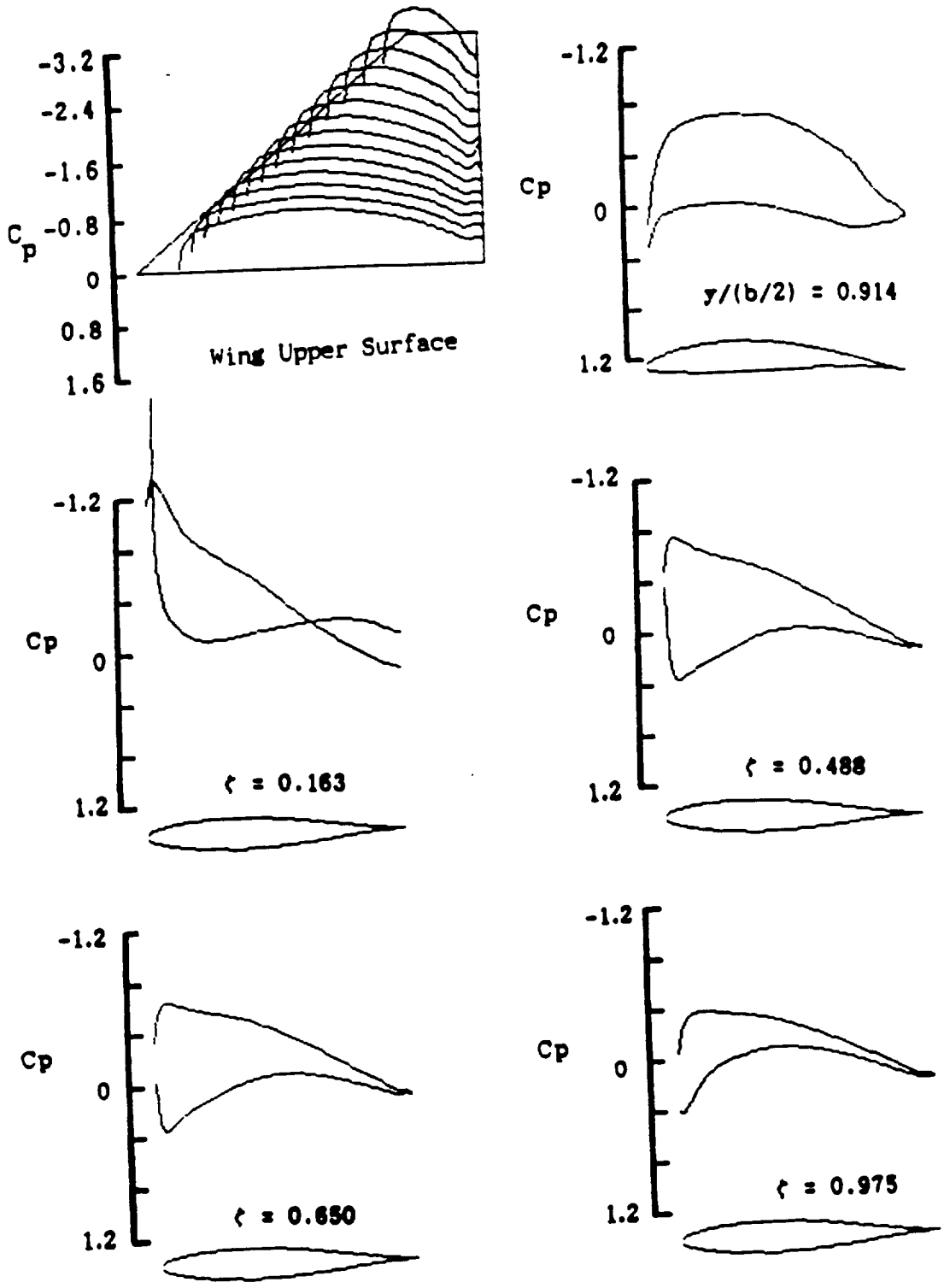

Fig. 55 Calculated C_p distributions for low-speed uncambered winglet airfoil cropped delta G configuration at M = 0.1, $\alpha = 0°$.

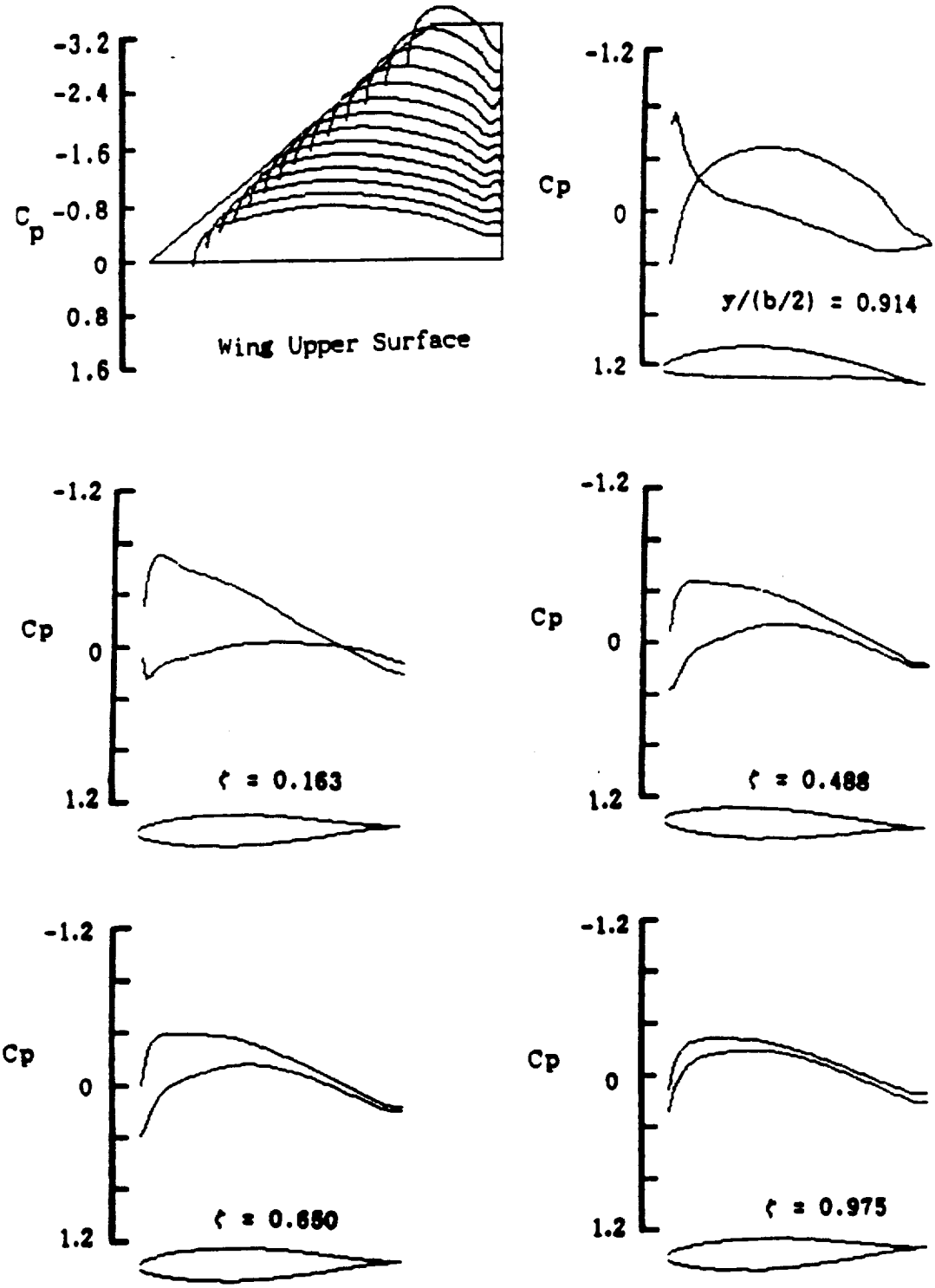

Fig. 56 Calculated C_p distributions for low-speed uncambered winglet airfoil cropped delta G configuration at M = 0.1, α = -4°.

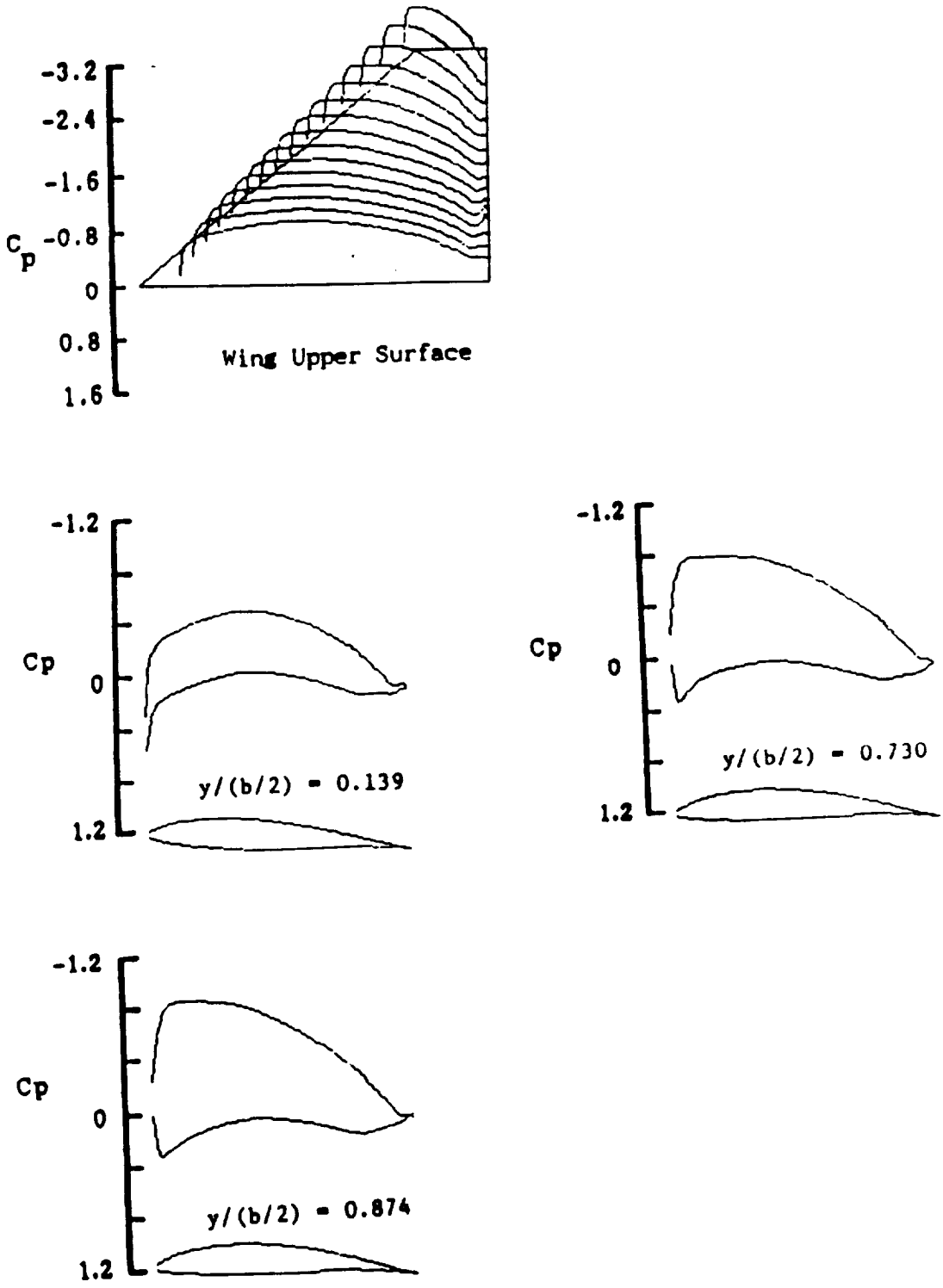

Fig. 57 Calculated C_p distributions for low-speed wing of wing-winglet cropped delta G configuration at M = 0.1, α = 4°.

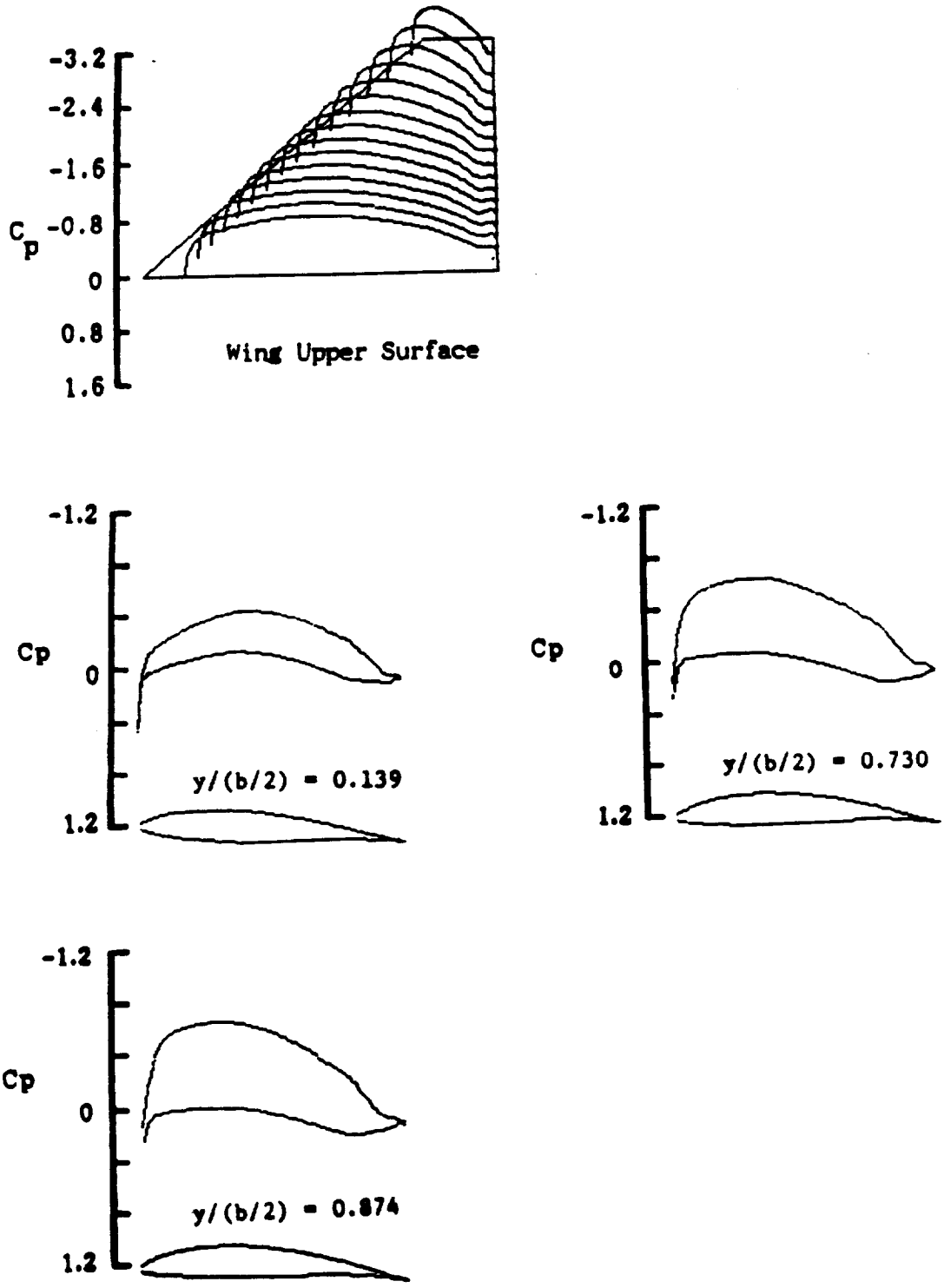

Fig. 58 Calculated C_p distributions for low-speed wing of wing-winglet cropped delta G configuration at M = 0.1, α = 0°.

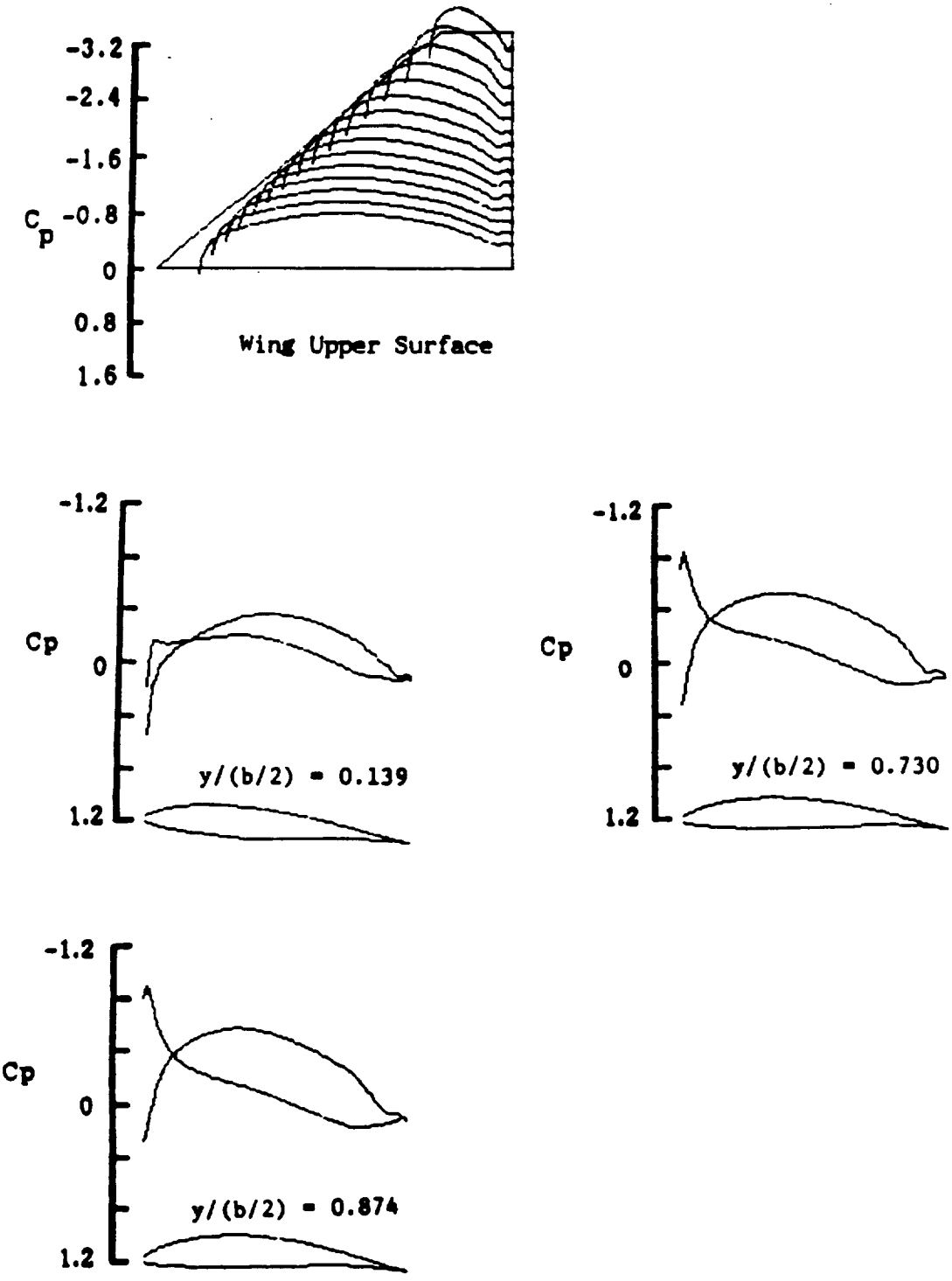

Fig. 59 Calculated C_p distributions for low-speed wing of wing-winglet cropped delta G configuration at M = 0.1, α = -4°.

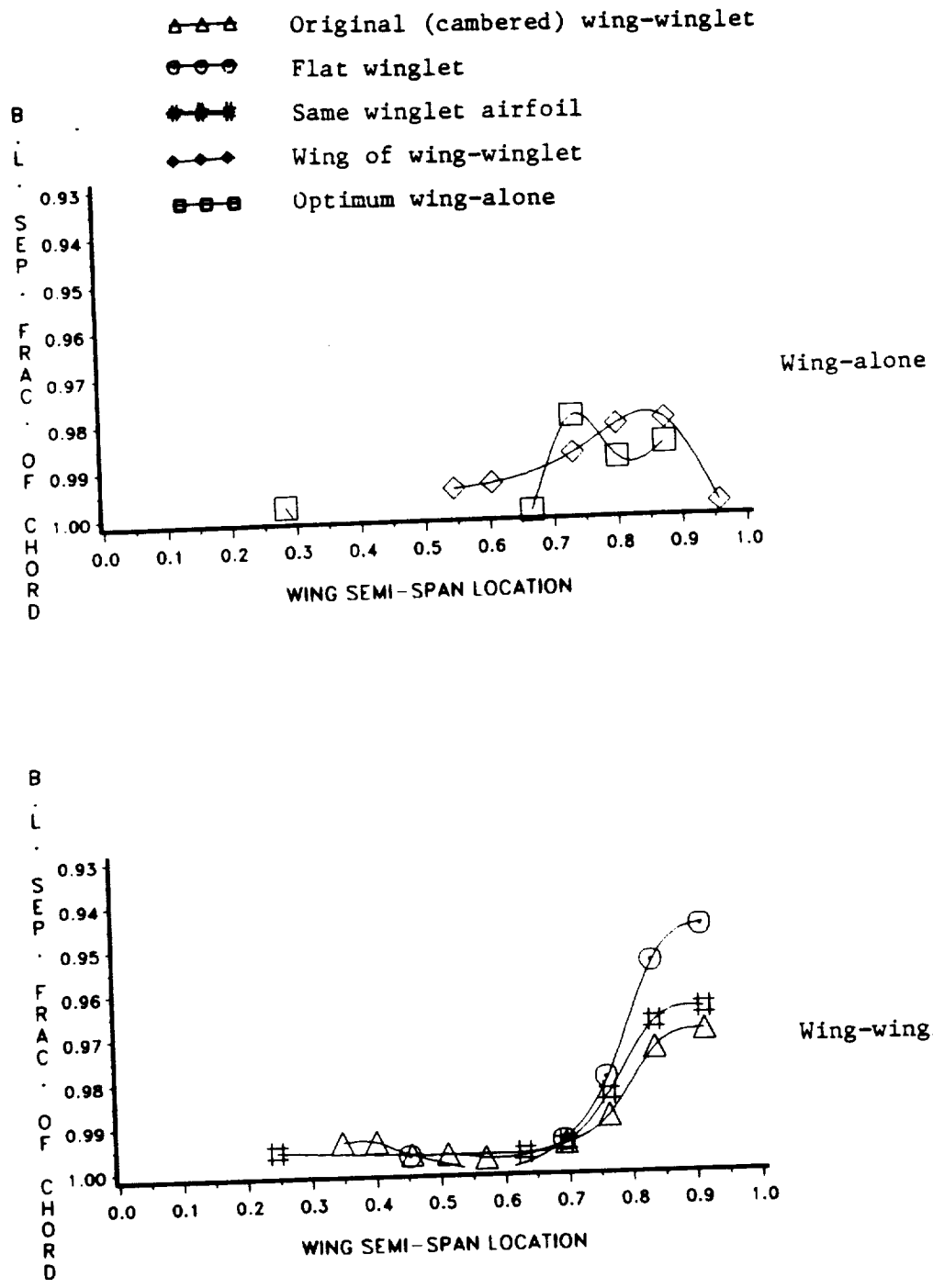

Fig. 60 Predicted wing upper surface boundary layer separation locations for all low-speed wing-alone and wing-winglet configurations at M = 0.1, $\alpha = 0°$.

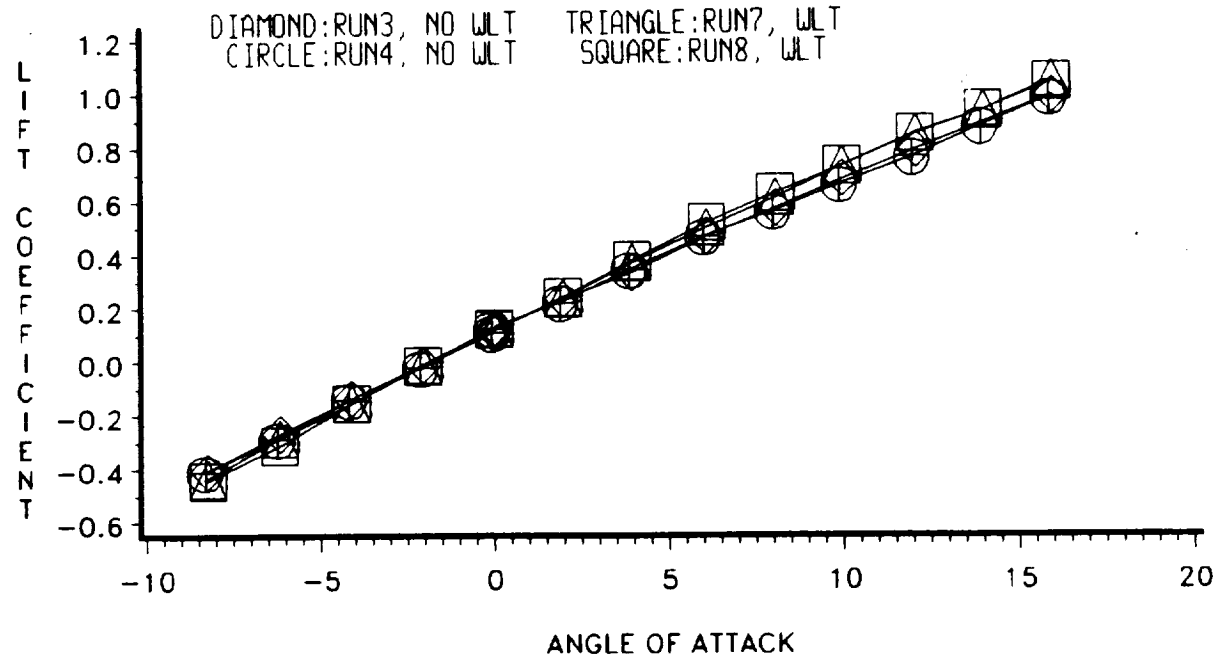

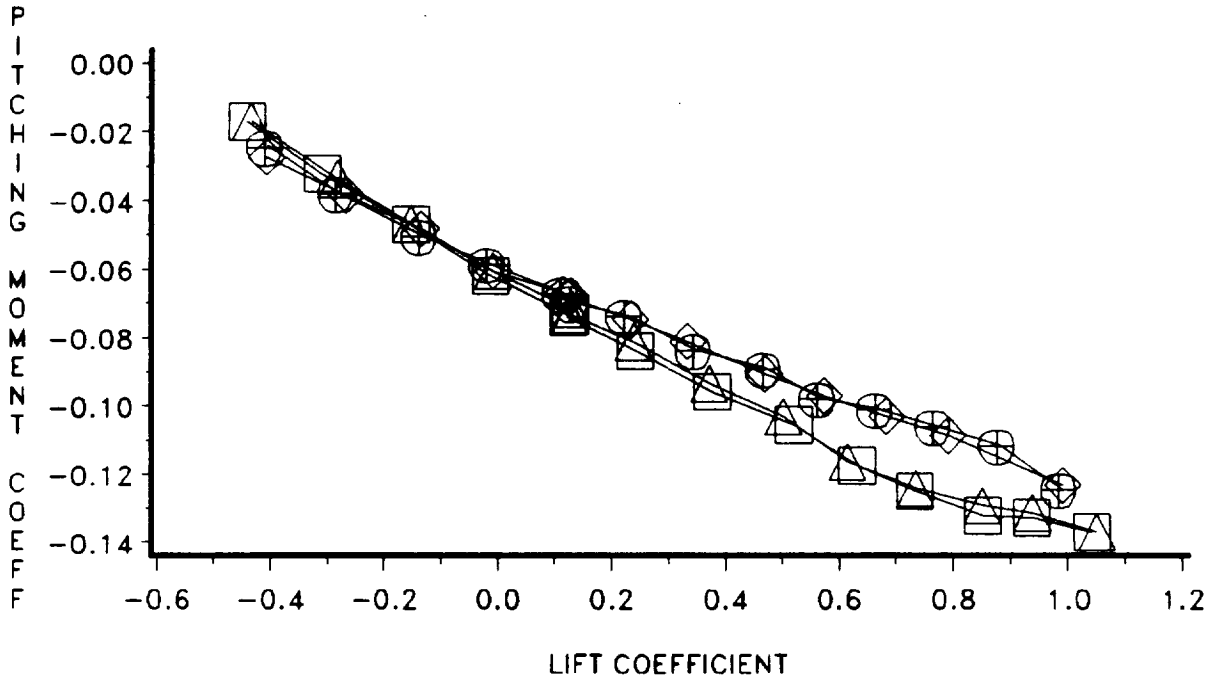

Fig. 61 Measured performance data for low-speed cropped delta G wind-tunnel model at U = 104 ft/sec.

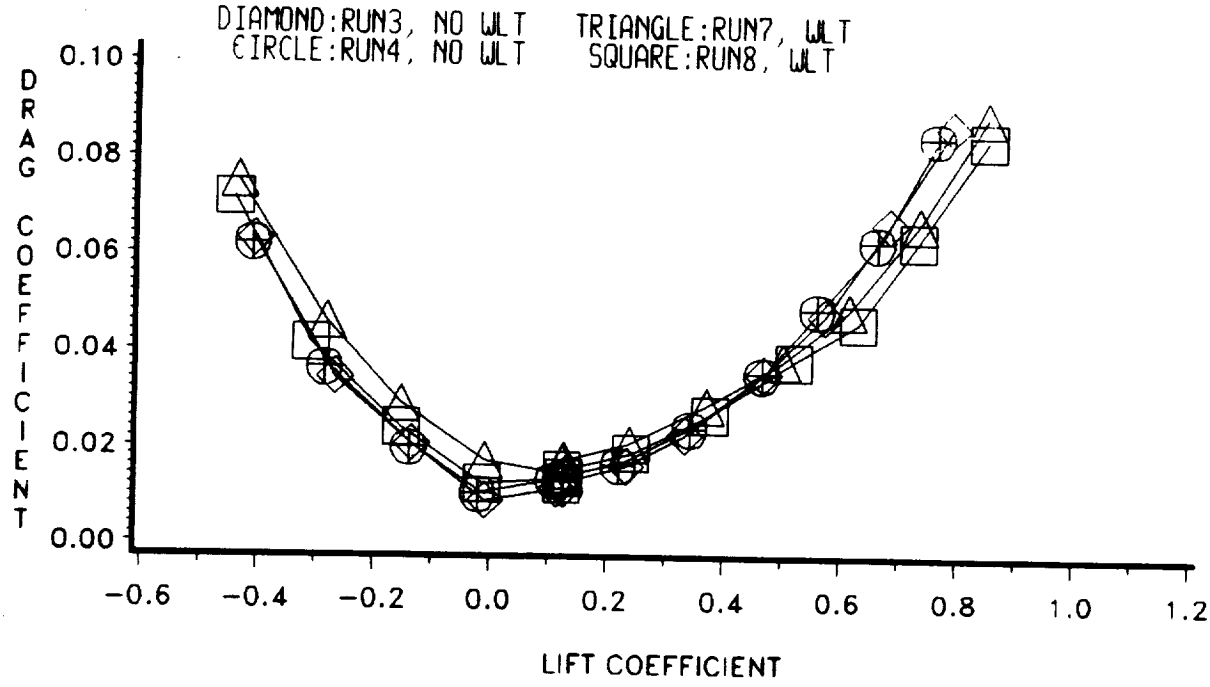

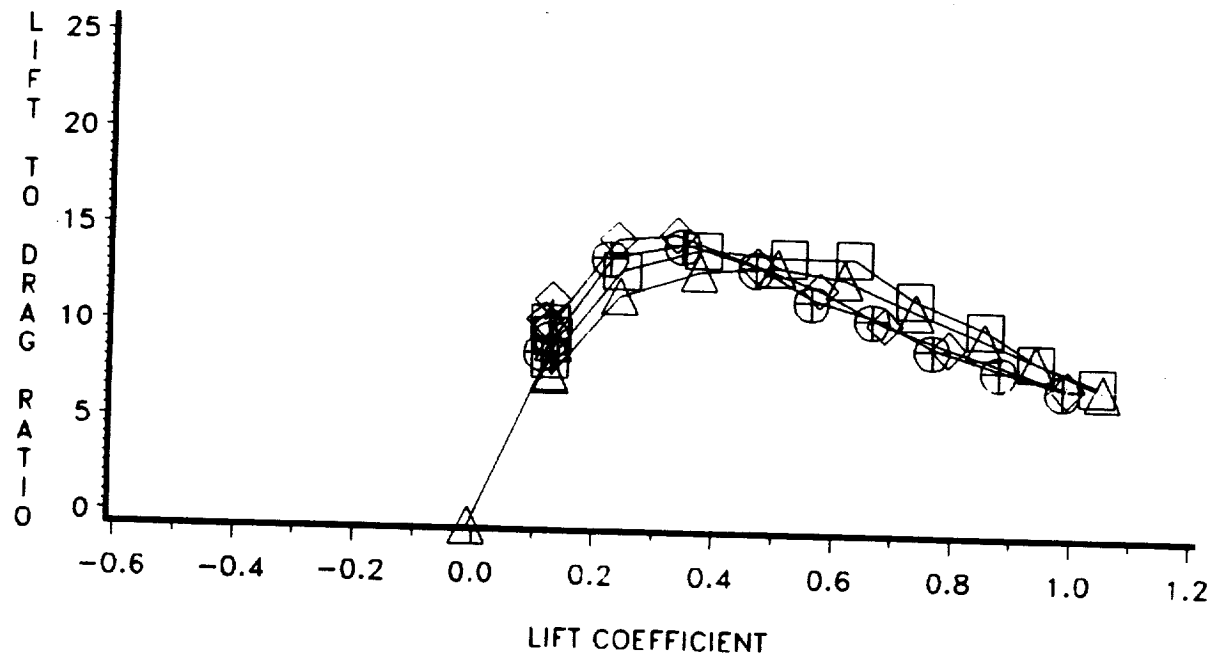

Fig. 61 (Concluded)

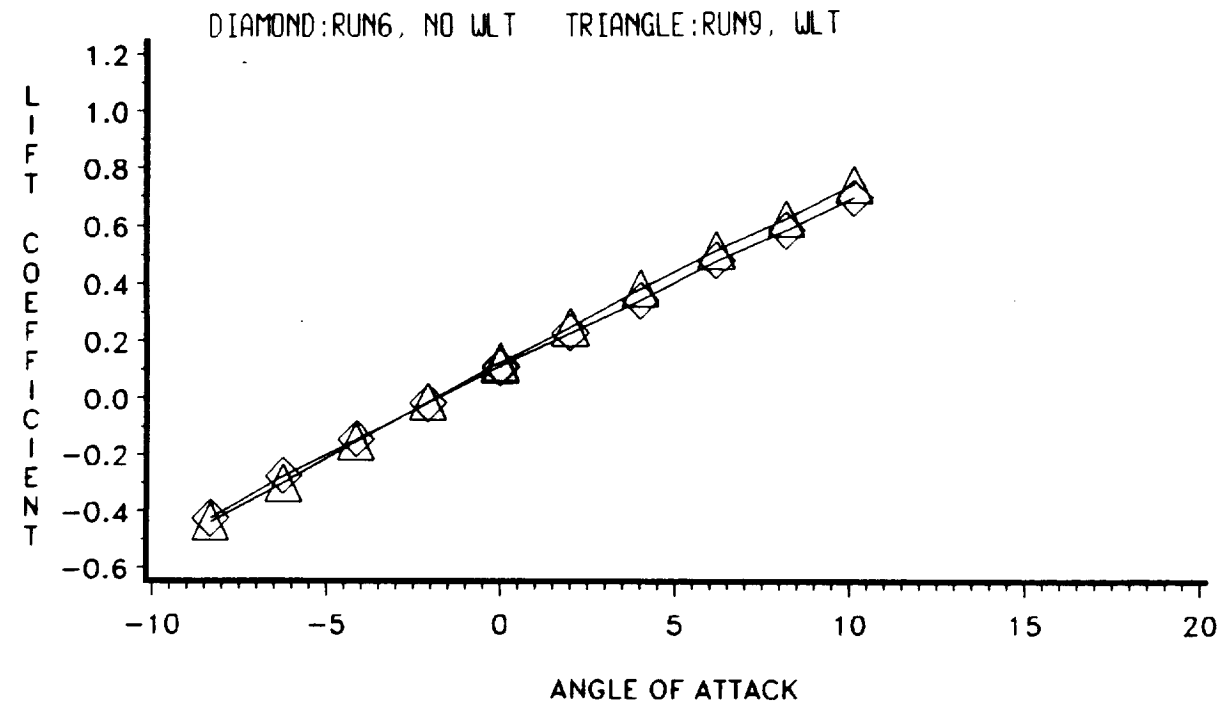

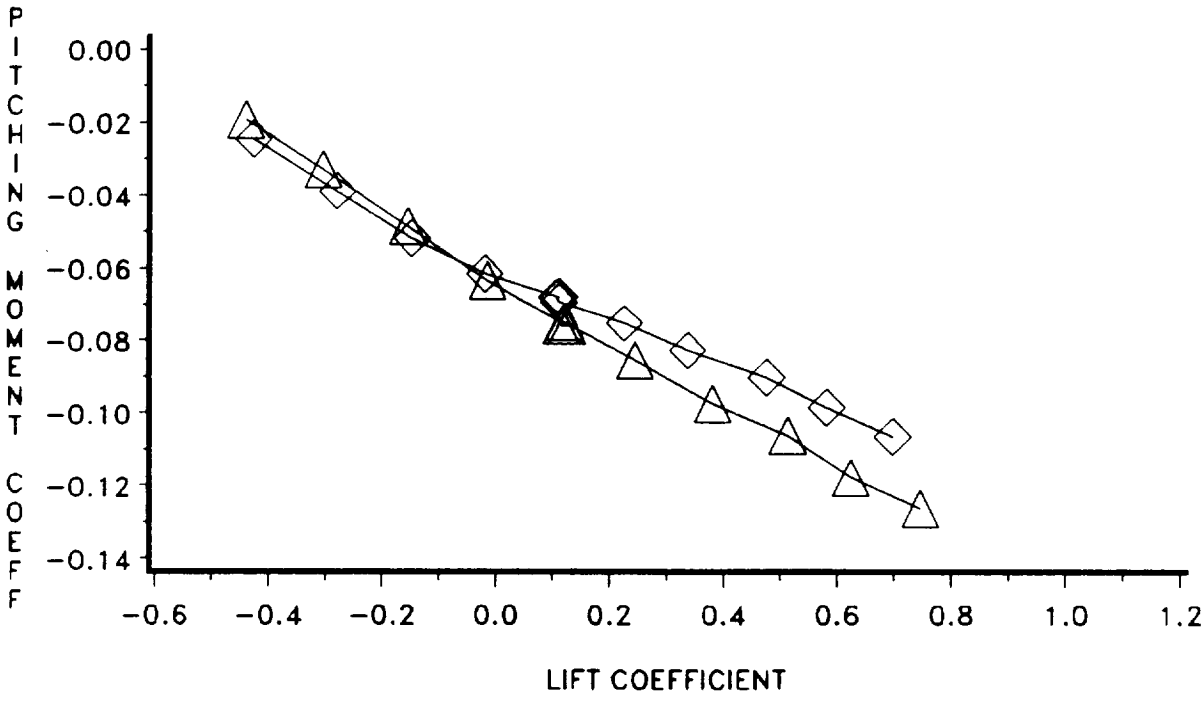

Fig. 62 Measured performance data for low-speed cropped delta G wind-tunnel model at U = 149 ft/sec.

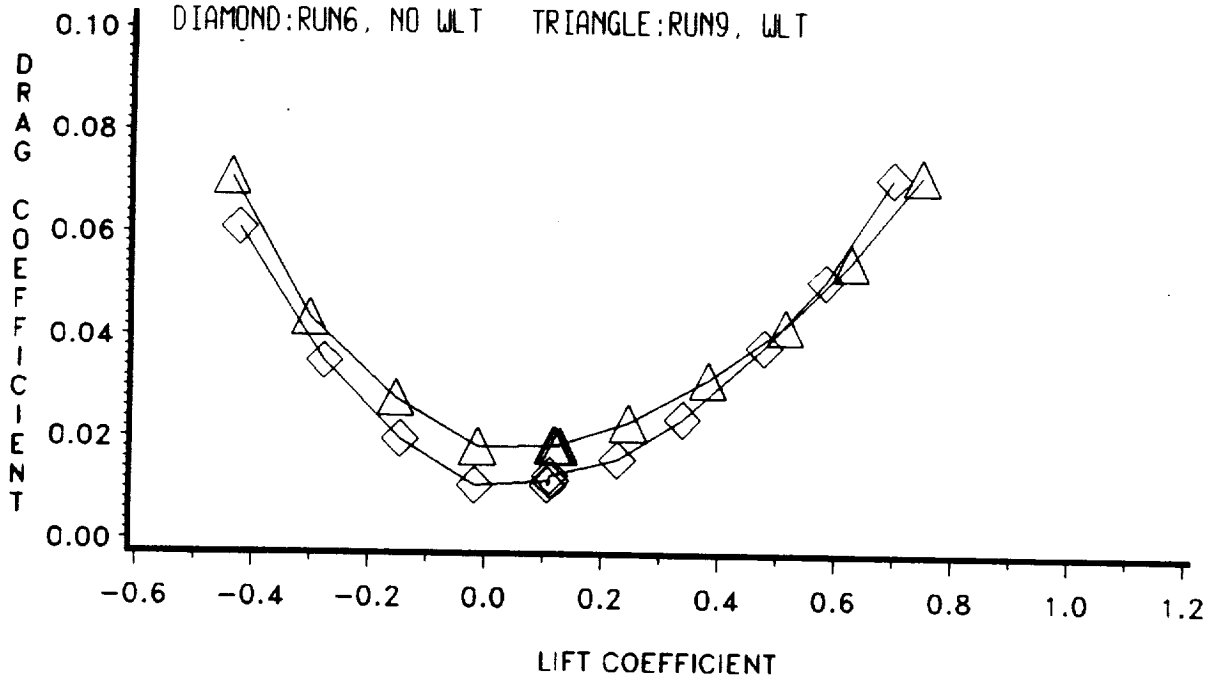

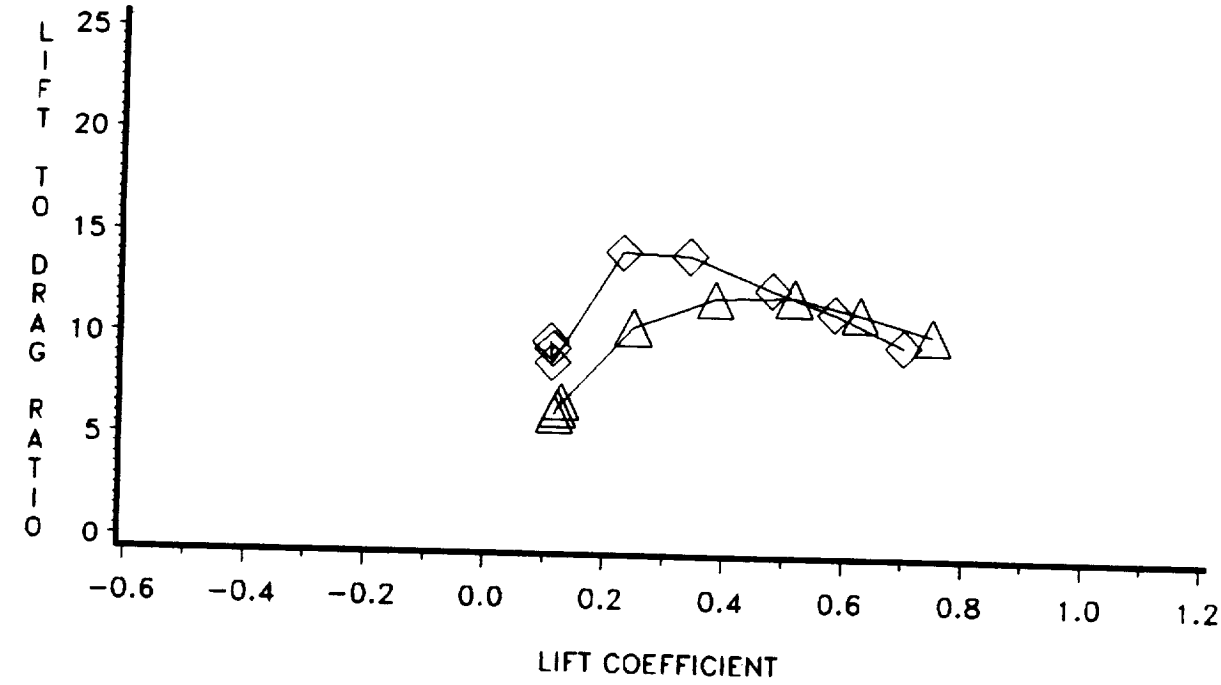

Fig. 62 (Concluded)

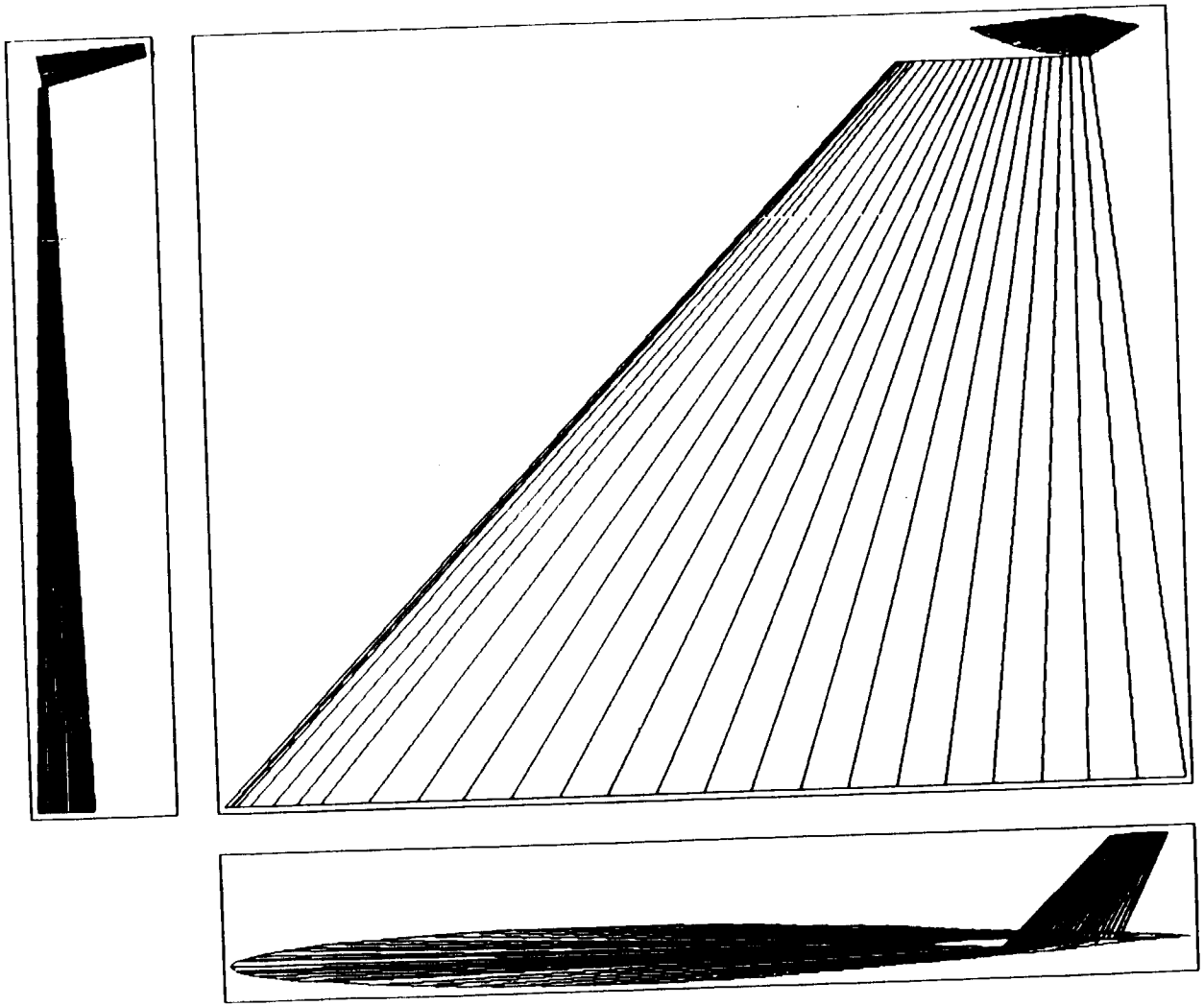

Fig. 63 Wing-winglet geometry for NASA general research fighter model fitted with winglets.

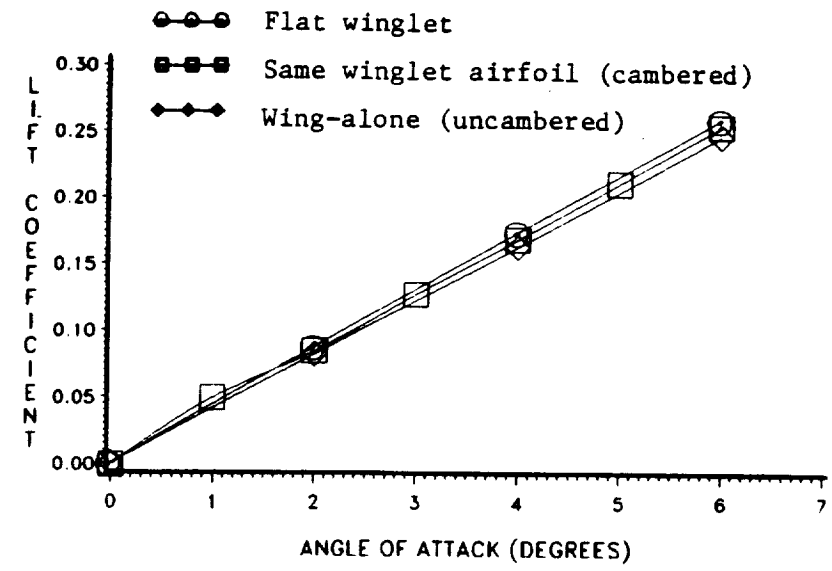

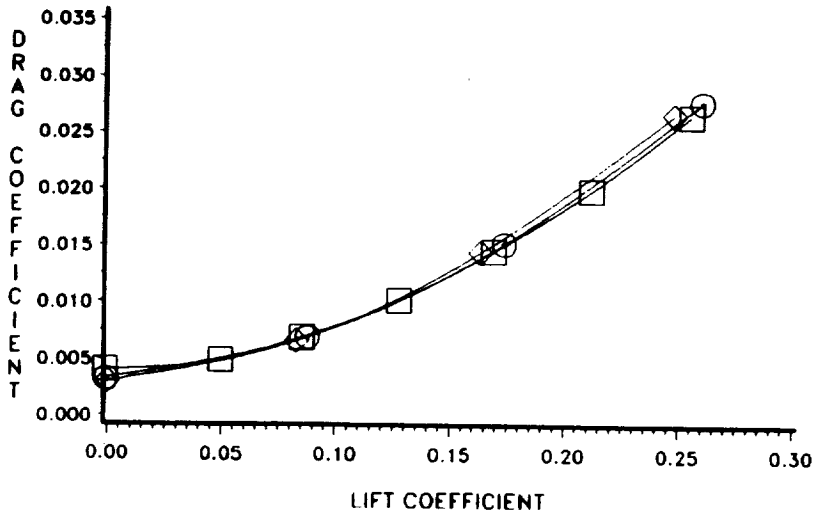

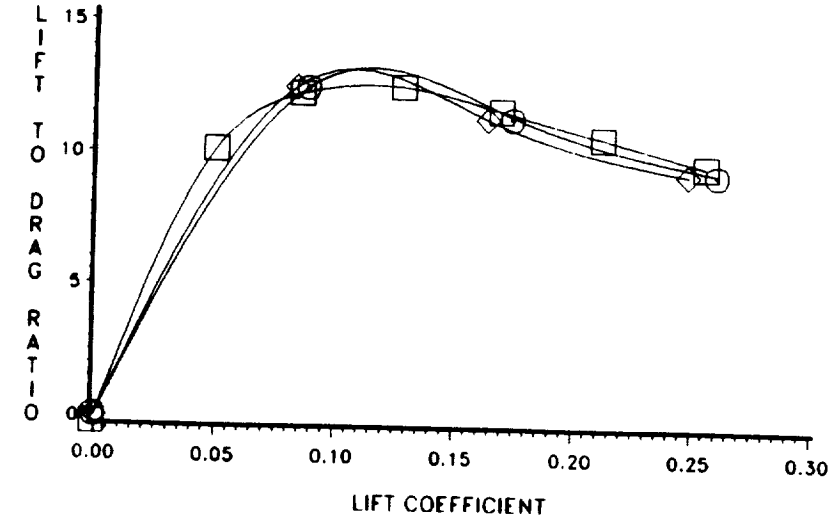

Fig. 64 Predicted performance of wing and wing-winglet configurations for NASA general research fighter model at M = 0.8; C_L - α, drag polar, and L/D - C_L.

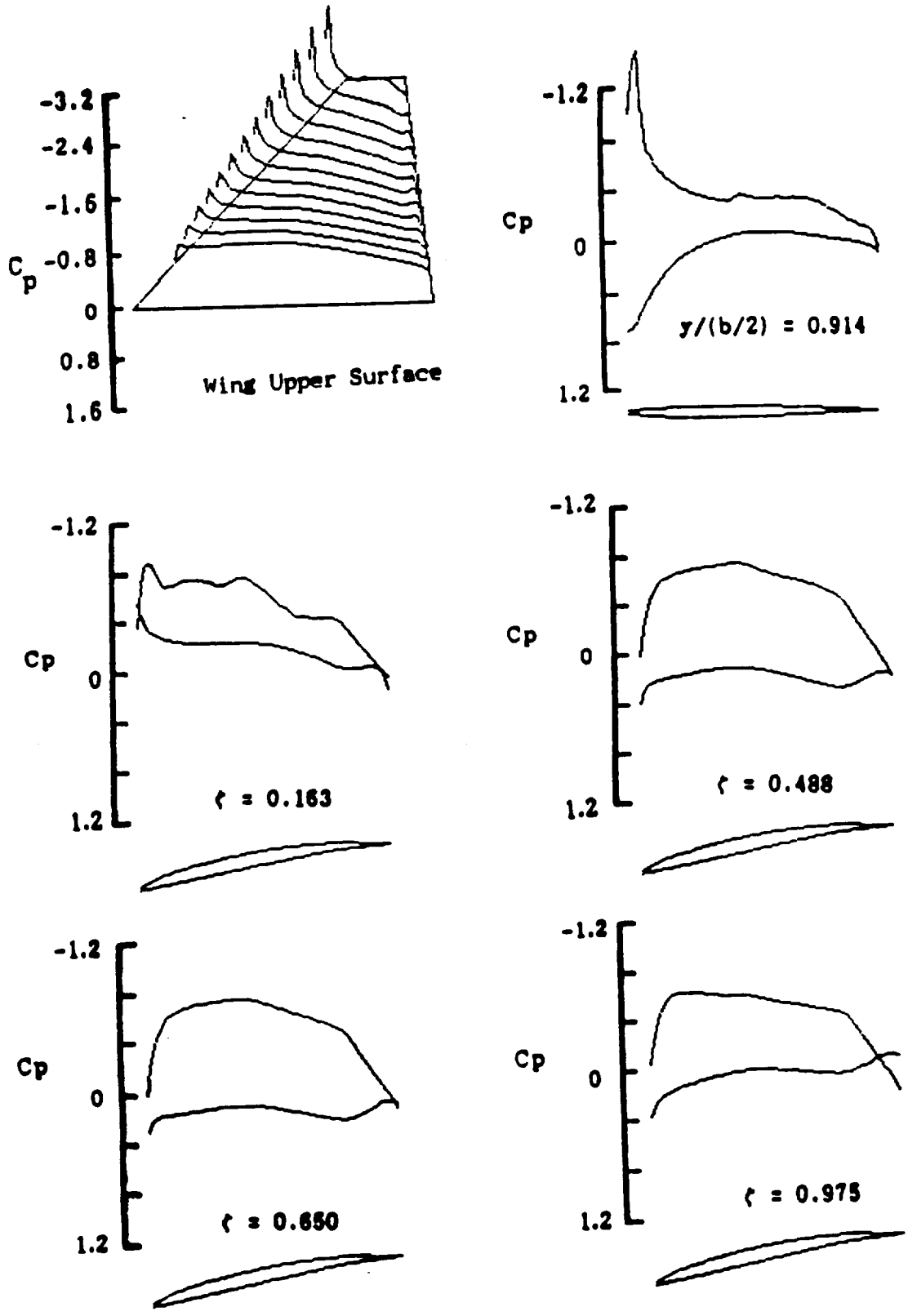

Fig. 65 Calculated C_p distributions for NASA general research fighter model fitted with cambered winglets at M = 0.8, α = 6°.

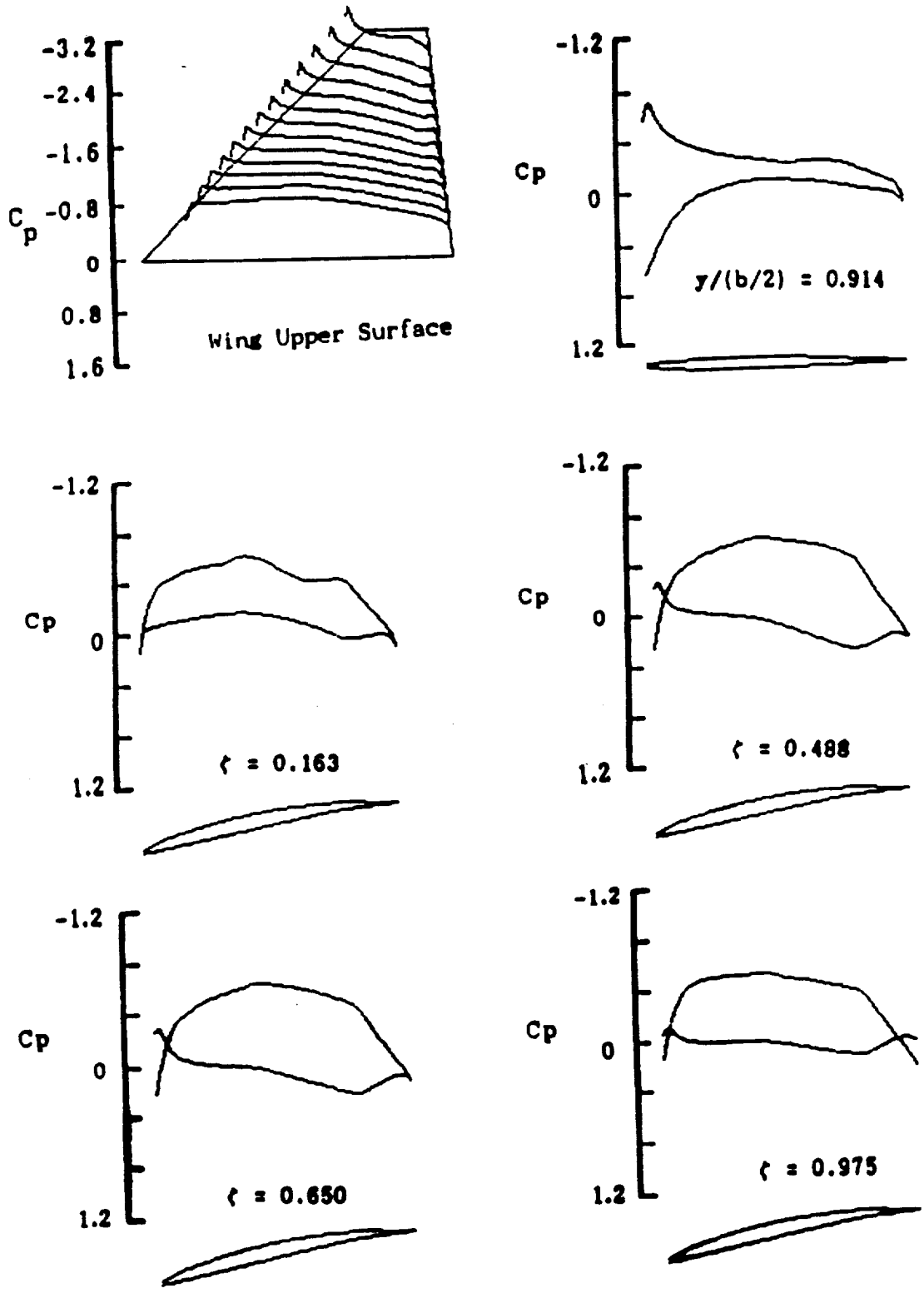

Fig. 66 Calculated C_p distributions for NASA general research fighter model fitted with cambered winglets at M = 0.8, α = 4°.

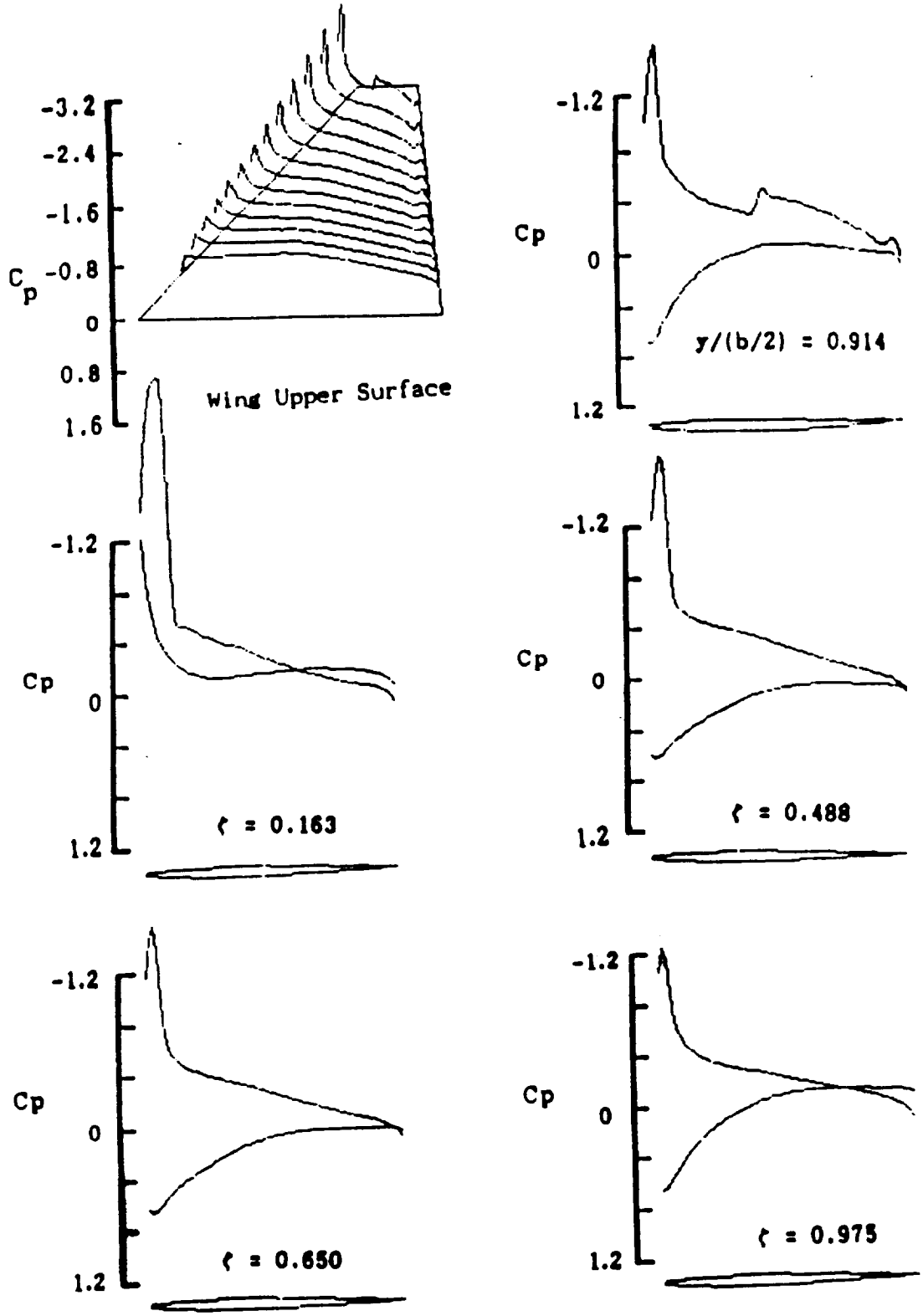

Fig. 67 Calculated C_p distributions for NASA general research fighter model fitted with uncambered winglets at M = 0.8, α = 6°.

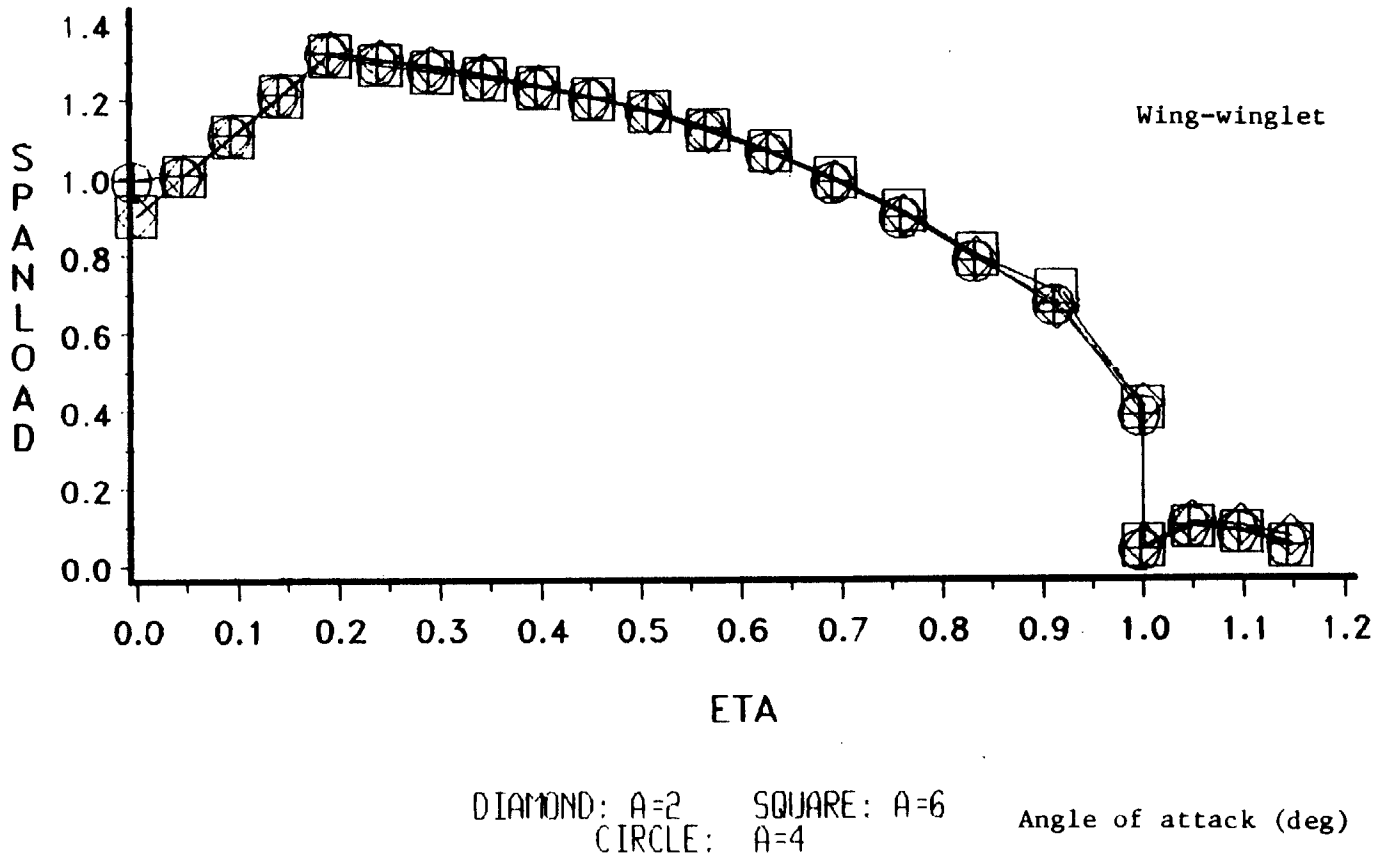

Fig. 68 Calculated normalized spanloads for NASA general research fighter model fitted with cambered winglets at M = 0.8.

NASA National Aeronautics and Space Administration

Report Documentation Page

1. Report No.	2. Government Accession No.	3. Recipient's Catalog No.
NASA CR-181939		

4. Title and Subtitle

Computational Design of Low Aspect Ratio Wing-Winglet Configurations for Transonic Wind-Tunnel Tests

5. Report Date

October 1989

6. Performing Organization Code

7. Author(s)

John M. Kuhlman and Christopher K. Brown

8. Performing Organization Report No.

10. Work Unit No.

505-61-21-03

9. Performing Organization Name and Address

West Virginia University
Department of Mechanical and Aerospace Engineering
Morgantown, WV 26506-6101

11. Contract or Grant No.

NAG1-625

13. Type of Report and Period Covered

Contractor Report
Jan. 1987 - May 1989

12. Sponsoring Agency Name and Address

National Aeronautics and Space Administration
Langley Research Center
Hampton, VA 23665-5225

14. Sponsoring Agency Code

15. Supplementary Notes

Langley Technical Monitor: Richard L. Campbell

Final Report - Jan. 1987 - May 1989

16. Abstract

Computational designs have been performed for three different low aspect ratio wing planforms fitted with nonplanar winglets; one of the three configurations has been selected to be constructed as a wind tunnel model for testing in the NASA LaRC 8-foot transonic pressure tunnel. A design point of M = 0.8, $C_L \cong 0.3$ was selected, for wings of aspect ratio equal to 2.2, and leading edge sweep angles of 45° and 50°. Winglet length is 15% of the wing semispan, with a cant angle of 15°, and a leading edge sweep of 50°. Winglet total area equals 2.25% of the wing reference area. This report summarizes the design process and the predicted transonic performance for each configuration.

In addition, a companion low-speed design study has been conducted, using one of the transonic design wing-winglet planforms but with different camber and thickness distributions. A low-speed wind tunnel model was constructed to match this low-speed design geometry, and force coefficient data have been obtained for the model at speeds of 100-150 ft/sec. Measured drag coefficient reductions were of the same order of magnitude as those predicted by numerical subsonic performance predictions.

17. Key Words (Suggested by Author(s))	18. Distribution Statement
Aerodynamics Transonic Flow Induced Drag Reduction Low Aspect Ratio Winglets	Unclassified - Unlimited Subject Category 02

19. Security Classif. (of this report)	20. Security Classif. (of this page)	21. No. of pages	22. Price
Unclassified	Unclassified	113	A06

For sale by the National Technical Information Service, Springfield, Virginia 22161-2171